nEUCLID: A NEW HOMODYNE INTERFEROMETER WITH SPACE APPLICATIONS

by

MIRANDA JANE BRADSHAW

A thesis submitted to the University of Birmingham
for the degree of
DOCTOR OF PHILOSOPHY

Astrophysics and Space Research Group
School of Physics and Astronomy
University of Birmingham
SEPTEMBER 2015

Abstract

The objective of this project was to design a low-mass, low-power interferometer to be used for space applications. It had to be capable of remaining tilt-immune whilst working at a distance of at least 1 m.

This thesis describes the design and subsequent building of a 1550 nm homodyne interferometer. Known as the new Easy to Use Compact Laser Interferometric Device (nEUCLID), it has a working distance of 660 mm and a working range of ±120 mm. These large distances are made possible by the novel cat's eye design within the interferometer, which also allows tilt immunity of ±0.35° of the target mirror (at the sweet plane). The thesis explains in detail the theory and design of the cat's eye, known as a pseudo cat's eye (PCE) in the text.

The interferometer, nEUCLID, has a sensitivity of 420 pm/$\sqrt{\text{Hz}}$, at 1 Hz in air, tested at the working distance of the current design. It has a mass of 2 kg and an overall power of 1.8 W. Both of these values are due to using standard, off-the-shelf components in the design, and could be reduced with further development.

Within this thesis ground-based and space-based applications for nEUCLID within the space industry are discussed and compared with existing technologies.

Acknowledgements

Firstly, I would like to thank Professor Clive Speake, for his continuing patience and support during my PhD. He was always available for discussions and advice whenever I had a problem or needed assistance, even when on holiday, and this project would not have progressed as far as it has without his support.

I am grateful to Dr Christian Trenkel for his continuous encouragement and spirit-raising from Airbus Defence and Space (DS) in Stevenage. He always gave a fresh perspective on whatever I was working on, and helped focus the task on the real-world applications. His support throughout my PhD was invaluable, especially during my placement at Airbus DS.

During daily laboratory work, I couldn't have managed without the on-going assistance of John Bryant and Dave Hoyland. John patiently helped me through software problems, and suggested sensible improvements to my mechanical fixtures. Dave built the electronics housing for the laser, and was on-hand to advise with any potential electronic noise problems. I would like to thank David Stops for his assistance with my computer, and the various times Matlab or Maple would not co-operate.

I also extend my thanks to Dr Michaela Nelson. She provided great insight into awkward Lissajous patterns and general missing intensities, and more importantly, she provided excellent and entertaining company in the lab.

Finally, I would like to thank Will Vousden, for getting me hooked on cycling (a great stress-reliever), for his never-ending patience, and for his indefatigable support throughout my PhD.

Contents

List of Figures

List of Tables

Chapter 1

INTRODUCTION

1.1 A Space Application

With the ever increasing competition between companies and countries in the space industry, new technologies are being welcomed with open arms. Low power, light-weight devices are being demanded, to improve mass and power budgets of modern spacecraft. Cost is also important; on average it costs approximately $22 000 to put 1 kg into geosynchronous orbit (GEO) [1]. Less massive technology will be more desirable, as less fuel is required to launch the device. This is why investment in interferometers as space-borne metrology tools is prudent; they can be made small and electronically and optically simple, and most of the optical parts required are already space-qualified from previous missions [2].

There are several areas within the space industry that lack sufficient technology to progress forward with future missions. Previous formation flying missions and large-scale observatories have been delayed or cancelled, due to lack of technology capable of the required precision. Large satellites are limited to the fairing size of the launch vehicle, with only the recent James Webb Space Telescope (JWST) being accepted as a feasible deployable structure worth proceeding with [3].

Meanwhile, with established satellites, telecommunications companies are demanding more precise ground coverage at the lowest possible price. Monitoring spacecraft and antenna distortion in/out of eclipse, and continuous monitoring of antenna centres are crucial to achieving this. Currently, these are either measured using an on-board computer system and ground loop (a time-consuming, and thus expensive process), or not at all.

Ground testing – a necessary procedure for all space missions – currently relies on accelerometers and cameras to measure and align components. Accelerometers add extra mass to vibration testing, whilst thermoelastic tests and antenna alignment procedures use simple cameras to take images of post-test components.

Chapter 6 explains in greater detail how the interferometer described in this thesis – the nEUCLID – would be useful for these applications, and compares the current technologies (if there are any).

I was tasked by Airbus Defence and Space (DS) UK to create an interferometer that could be used for a variety of space applications. Airbus DS is the largest space company in

Europe, and the third largest in the world [4]. They develop and fund future technologies that are advantageous to the space industry. The following specifications for the device were laid out:

- low mass (under 5 kg)
- low power (under 10 W)
- dimensions less than 300 mm × 200 mm × 100 mm
- tilt immunity (scales inversely with working distance; ±0.5° for 1 m)
- working distance of at least 1 m.

Two of the most desired characteristics were tilt immunity of the measurement target, and a long working distance. Whilst both the University of Birmingham interferometers (EUCLID and ILIAD) described in Section 2.5 are tilt-immune, neither are capable of a working distance of more than 60 mm. EUCLID is a compact displacement-measuring homodyne interferometer with a working distance of 6 mm, whilst ILIAD is a compact rotation-measuring homodyne interferometer with a working distance of 59 mm, capable of working at both room temperature and in cryogenic experiments.

Airbus DS also specified that the interferometer should be coaxial, to allow use on curved surfaces, such as antenna dishes. No interferometer at the University met all of these criteria, thus the need to develop nEUCLID.

1.2 Why an Interferometer?

Since the first interferometer was invented in 1887 [5] interferometers have been used for a wide range of applications, from measuring the anisotropy of the velocity of light [5] to the search for gravitational waves [6], from imaging body tissue [7] to aligning the surfaces of next-generation telescopes [8]. The common theme among these applications is the measurement of change; in displacement, in velocity or in the type of surface. The change investigated within this thesis is the change in phase of the interference pattern, caused by the change in displacement of a target mirror.

The potential for extremely high sensitivity makes interferometers a favourable experimental choice, whilst the basic design concept ensures the instrument can be used across many research fields. They are capable of wavelength-resolution measurements, yet can be simple to tailor for specific applications. Due to the simplicity of the basic design they can be constructed from components available off-the-shelf – a light source and several optical components (see Section 2.1) – meaning it is straightforward to implement this basic design. These components are available for many different wavelengths and are often space-qualified. Interferometers are also not limited by size; they can be as compact or as large as an application requires; e.g., aLIGO [6] compared to EUCLID [9].

Interferometers can be applied to a wide range of space activities, both on the ground and in orbit. Due to requiring few active components (i.e., a laser source and simple electronics) the mass and power budget is low, and their flexibility of size means they can be scaled up

or down to suit each mission. The nanometre sensitivity of interferometers is appealing to the space industry due to the increasing demand in finer precision of measurements, both from space and from testing on the ground. These reasons encouraged Airbus DS to look at interferometers for future space applications.

Extensive research has already been undertaken at the University of Birmingham regarding compact tilt-immune interferometers [9, 10], so these were the ideal candidates for further development. Tilt immunity is not common in interferometers; a patent was investigated for the design within this thesis and no competing technology was found, for either the new cat's eye (the PCE) or the interferometer design.

1.3 Outline of Thesis

This thesis describes the design and subsequent building of a new polarisation-based homodyne interferometer that is immune to tilt at a distance of 660 mm. The design contains a novel cat's eye lens system that was also created during this project; the thesis will discuss both the cat's eye and the interferometer. Chapter 3 to Chapter 5, and Chapter 7 are all my own work. Applications of the interferometer within the space industry will also be examined.

Chapter 2 outlines the concept of an interferometer and discusses two of the most common types of interferometers: heterodyne and homodyne. Previous polarisation-based homodyne interferometers are discussed, as are the interferometers that have been built at the University of Birmingham.

Chapter 3 describes the new cat's eye design; what it evolved from and how it works within the new interferometer. It also discusses how the new cat's eye is not a perfect cat's eye, and how this was innovatively dealt with using a mensicus lens.

Chapter 4 details nEUCLID; the optical configuration, the method of alignment, discussion on the laser selection, and the characteristics of the device.

Chapter 5 shows the results taken with nEUCLID: the sensitivity in air, the range of tilt immunity in and beyond the sweet plane, and the imperfections within the system.

Chapter 6 discusses potential space applications of nEUCLID – the driving force behind nEUCLID's creation.

Chapter 7 evaluates the work discussed in this thesis. Suggestions for future work are also expanded upon, such as improvements of the sensitivity and an absolute nEUCLID.

Chapter 2

INTERFEROMETRY

2.1 A Basic Interferometer

An interferometer is an optical device that causes two beams of light to interfere. Using the principle of superposition, when the two beams are combined their amplitudes are added together, creating an interference pattern. This pattern is made of consecutively dark and light strips ("fringes"), as shown in Section 2.2.1, and can be used to determine optical path length changes within the system, as discussed later in Section 2.2.4. Lasers are used to ensure the original beam is coherent (in phase), and monochromatic (the same frequency), so the interference pattern observed is solely from change within the system (e.g. a mirror moving towards/away from the system).

The simplest design of interferometer is a Michelson interferometer. It was invented in 1887 [5], and consists of a white light source, a half-silvered mirror (HSM), two standard mirrors, and a detector (D). The beam from the light source passes through the half-silvered mirror, causing half the beam to be transmitted to mirror 1 (M_1), and the other half of the beam to be reflected to mirror 2 (M_2). The passage from the half-silvered mirror to each standard mirror is known as an *arm* of the interferometer. Each beam travels to the mirror in its respective arm, where it is reflected back through the half-silvered mirror and recombined into one beam to form an interference pattern, such as shown in Fig. 2.6. Moving either M_1 or M_2 alters the length of that arm, changing the optical path length, and causing a change in phase between the two beams. This phase difference results in a varying fringe pattern at the detector, from which the mirror displacement can be measured (see Section 2.2.4).

The Michelson design has several issues that caused the design of later interferometers to develop beyond this. The design lacks the ability to determine the direction of the mirror motion; a major problem for most applications where direction of movement is critical. The Michelson is also susceptible to mirror tilt, causing additional (and erroneous) displacement measurement.

The design of interferometers has continued to advance, to cope with these problems, and these designs will be discussed in Section 2.3 and Section 2.4.

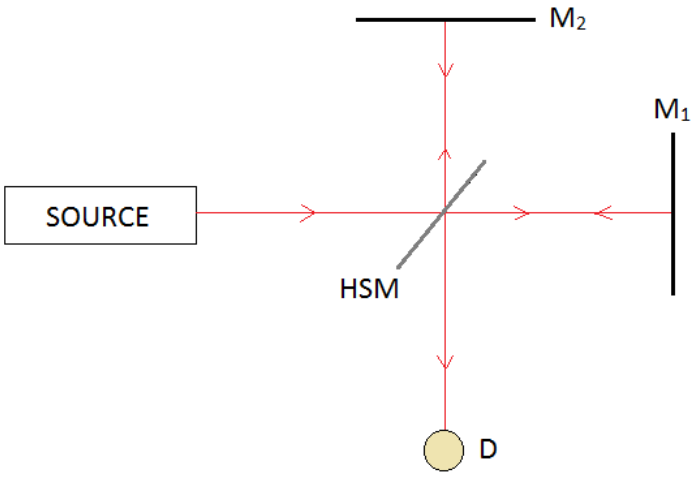

Figure 2.1: Schematic diagram of a Michelson interferometer, showing the two mirrors, M_1 and M_2 and the detector, D.

2.1.1 In-Quadrature Measurements

With one signal from the interferometer, the direction of the mirror movement within an arm is not possible to define. As the mirror is moved the interference pattern fringes change from dark to bright, and the signal at the detector moves between minimum and maximum. This occurs whether the mirror moves forwards or backwards. To enable the direction of the mirror motion to be calculated the sign of the phase difference between the beams must be known (see Section 2.2.1 for mathematical detail). Because the two beams are superposed, the phases are combined into one value. In order to determine the mirror direction a known phase difference is added between the beams, and observed in two interference patterns. When the visibility of one interference pattern is a maximum/minimum, the phase-shifted interference pattern will either lead or lag behind the first by $\pm\pi/2$ (the added phase difference). This known phase difference allows the mirror direction to be calculated (see Section 2.2.4 for details).

In both Easy to Use Compact Laser Interferometric Device (EUCLID) and nEUCLID this added value is a phase difference of $\pm\pi/2$, so the two interference patterns are 90° out of phase with each other – in "phase quadrature".

2.2 Understanding Interferometry

Sections 2.2.1 to 2.2.3 and 2.2.5 summarise the workings in Hecht [11, Sections 9.1 and 9.4.2].

2.2.1 Superposition and Interference

The principle of superposition is that two waves arriving at the same place will overlap, adding together (or subtracting from each other). The result is the sum of the individual

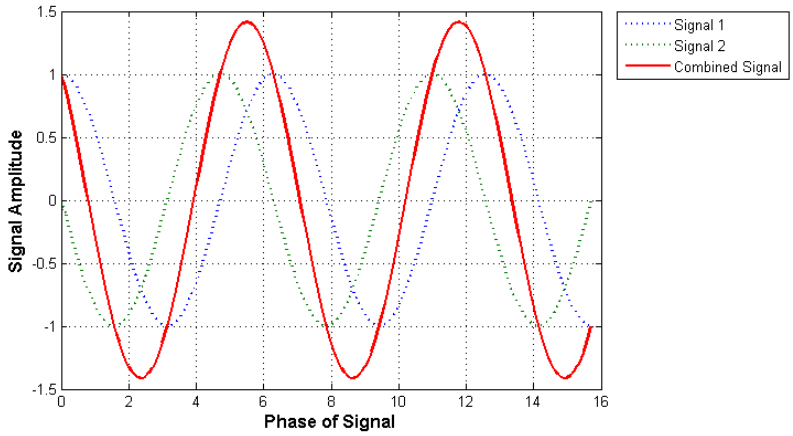

Figure 2.2: Modelled example of the superposition of two cosine waves, one with an offset of $+\pi/2$.

wave components at that point. The sum of the waves gives rise to interference. If the waves are in phase they will constructively interfere; if out of phase, the interference will be destructive. The waves must have the same polarisation to create an interference pattern.

Light is a vector in that it consists of both an electric and a magnetic field. To thoroughly model what happens during interference observe two linearly polarised plane waves from a monochromatic source

$$\mathbf{E}_1(\mathbf{r}, t) = \mathbf{E}_{01} \cos(\mathbf{k}_1 \cdot \mathbf{r} - \omega t + \epsilon_1), \tag{2.1}$$

and

$$\mathbf{E}_2(\mathbf{r}, t) = \mathbf{E}_{02} \cos(\mathbf{k}_2 \cdot \mathbf{r} - \omega t + \epsilon_2), \tag{2.2}$$

where $\mathbf{E}_{01}$ and $\mathbf{E}_{02}$ are the vector amplitudes of each wave, ϵ_1 and ϵ_2 are the initial phases of each wave, ω is the angular frequency, and $\mathbf{k}$ the wavenumber $(2\pi/\lambda)$.

The irradiance $(\mathrm{W\,m^{-2}})$ at the photodiodes is defined as

$$I \equiv \frac{cn\epsilon_0}{2} \langle \mathbf{E}^2 \rangle_T, \tag{2.3}$$

where c is the speed of light, n is the refractive index, ϵ_0 is the vacuum permittivity, and $\langle \cdot \rangle_T$ denotes the average over time. As this derivation is only concerned with relative irradiance in the same medium, the constants will be neglected.

For the two waves, $\mathbf{E}^2$ becomes

$$\mathbf{E}^2 = (\mathbf{E}_1 + \mathbf{E}_2) \cdot (\mathbf{E}_1 + \mathbf{E}_2). \tag{2.4}$$

Thus, at the photodiodes the superposition of the two waves as electric field vectors is

$$\mathbf{E}^2 = \mathbf{E}_1^2 + \mathbf{E}_2^2 + 2\mathbf{E}_1 \cdot \mathbf{E}_2. \tag{2.5}$$

Taking the time average of each term in Eq. (2.5) gives an irradiance of

$$I = I_1 + I_2 + 2I_{12}. \tag{2.6}$$

As shown in Eq. (2.6) there is a third term – the *interference term*, I_{12} – that contributes to the interference of the two waves.

For simplicity, if we assume $\mathbf{E}_{01}$ and $\mathbf{E}_{02}$ are parallel (i.e. the angle between these vectors is zero, thus they become scalars), the interference term in Eq. (2.6) reduces to

$$I_{12} = E_{01}E_{02}\cos\Delta, \tag{2.7}$$

where Δ is the phase difference of the two waves,

$$\begin{aligned}\Delta &= \mathbf{k}_1 \cdot \mathbf{r} - \mathbf{k}_2 \cdot \mathbf{r} + \epsilon_1 - \epsilon_2 \\ &= (\mathbf{k}_1 - \mathbf{k}_2)\,\mathbf{r} + (\epsilon_1 - \epsilon_2)\end{aligned} \tag{2.8}$$

Equation (2.6) can be written more conveniently as

$$I_1 = \langle \mathbf{E}_1^2 \rangle_T = \frac{E_{01}^2}{2}, \qquad \text{and} \qquad I_2 = \langle \mathbf{E}_2^2 \rangle_T = \frac{E_{02}^2}{2}, \tag{2.9}$$

The interference term can thus be written as

$$I_{12} = 2\sqrt{I_1 I_2}\cos\Delta, \tag{2.10}$$

and the total irradiance as

$$I = I_1 + I_2 + 2\sqrt{I_1 I_2}\cos\Delta. \tag{2.11}$$

When Δ is $0, \pm 2\pi, \pm 4\pi, \ldots$, the two waves are in phase, the amplitude is a maximum and constructive interference occurs (a bright "fringe"). When Δ is $\pi, \pm 3\pi, \pm 5\pi, \ldots$, the two waves are 180° out of phase, the amplitude is a minimum and the interference is destructive (a dark "fringe").

An interesting result occurs if the amplitudes of both waves are equal, i.e. $\mathbf{E}_{01} = \mathbf{E}_{02}$. As the irradiance from each source is equal, $I_1 = I_2 = I_0$, and Eq. (2.11) can be re-written as

$$I = 4I_0 \cos^2 \frac{\Delta}{2}, \tag{2.12}$$

where $I_{min} = 0$ and $I_{max} = 4I_0$; an interference pattern of much greater visibility is achieved (see Eq. (2.30)). In the case of spherical waves, Δ can be rewritten as

$$\Delta = k(r_1 - r_2) + (\epsilon_1 - \epsilon_2), \tag{2.13}$$

where k is the wavenumber, and r_1 and r_2 are the distances from source 1 and source 2, respectively.

2.2.2 Formation of Interference Patterns

Using Eq. (2.13), Eq. (2.12) can be expressed as

$$I = 4I_0 \cos^2 \frac{1}{2}[k(r_1 - r_2) + (\epsilon_1 - \epsilon_2)]. \tag{2.14}$$

Maxima occur when

$$\Delta = 2\pi m, \tag{2.15}$$

Minima occur when

$$\Delta = \pi(2m + 1), \tag{2.16}$$

where m is any integer.

If the waves are in phase, (e.g., $\epsilon_1 - \epsilon_2 = 0$), the maxima and minima are

$$r_1 - r_2 = \frac{\pi 2m}{k} = m\lambda, \tag{2.17}$$

$$r_1 - r_2 = \frac{\pi(2m + 1)}{k} = (m + \frac{1}{2})\lambda, \tag{2.18}$$

Using Eq. (2.14), the minimum and maximum irradiance of the waves are

$$I_{max} = 4I_0 \cos^2 m\pi = 4I_0, \tag{2.19}$$

and

$$I_{min} = 4I_0 \cos^2 (m + \frac{1}{2})\pi = 0, \tag{2.20}$$

2.2.3 Optical Path Length

It is important to note that a difference in phase can also come from a difference in displacement (or *path length*) travelled by the beams. Equation (2.13) can be re-written in terms of wavelength to give

$$\Delta = \frac{2\pi}{\lambda}(r_1 - r_2) + (\epsilon_1 - \epsilon_2). \tag{2.21}$$

If the phase of each beam does not change (i.e. $\epsilon_1 = \epsilon_2$), the phase difference relies on the difference in path length of the two beams

$$\Delta = \frac{2\pi}{\lambda}(r_1 - r_2). \tag{2.22}$$

The optical path length of the device described in this thesis – nEUCLID – is examined and calculated in Section 3.3.4.

2.2.4 Calculating Displacement from Interference Patterns

A Michelson interferometer has two arms. The input laser beam has an amplitude A_{in} which is split into the two arms. Each arm has a beam, labelled by $n = 1$ or 2, which has an amplitude of $\frac{A_{in}}{2}$, which travels a distance of $2l_n$ (from the beamsplitter to the mirror and back). Using complex notation, the two beams recombine at the photodetector with intensity

$$A_{out} = \frac{A_{in}}{2}\left(e^{-i\phi_1} + e^{-i\phi_2}\right), \tag{2.23}$$

where ϕ_n is the phase of each beam,

$$\phi_n = \frac{2\pi}{\lambda} 2l_n. \tag{2.24}$$

Equation (2.23) can be re-written, separating out the phase difference of each beam in terms of length

$$A_{out} = \frac{A_{in}}{2} e^{i\frac{2\pi}{\lambda}(l_1+l_2)}\left(e^{-i\frac{2\pi}{\lambda}(l_1-l_2)} + e^{-i\frac{2\pi}{\lambda}(l_2-l_1)}\right). \tag{2.25}$$

The intensity of a beam is given by the square of its amplitude, thus is

$$I_{out} = \left|\frac{A_{in}}{2}\right|^2 \left|e^{i\frac{2\pi}{\lambda}(l_1+l_2)}\right|^2 \left|\left(e^{-i\frac{2\pi}{\lambda}\Delta l} + e^{+i\frac{2\pi}{\lambda}\Delta l}\right)\right|^2, \tag{2.26}$$

Eq. (2.26) can be reduced using trigonometric identities

$$\left(e^{-i\frac{2\pi}{\lambda}\Delta l} + e^{+i\frac{2\pi}{\lambda}\Delta l}\right) = \cos(-\theta) + i\sin(-\theta) + \cos\theta + i\sin\theta = 2\cos\theta \tag{2.27}$$

where θ is

$$\theta = \frac{2\pi}{\lambda}\Delta l. \tag{2.28}$$

So, the intensity of the output beam is now

$$I_{out} = \frac{A_{in}^2}{4} 4\cos^2\theta = \frac{A_{in}^2}{2}\left(\cos\frac{2\pi}{\lambda} 2\Delta l + 1\right). \tag{2.29}$$

When $2\Delta l = \lambda$ the wave has travelled through an entire (bright) fringe, and Eq. (2.29) is reduced to A_{in}^2. Likewise, when the wave has travelled half this distance ($\Delta l = \lambda/2$), a dark fringe is observed. The pathlength of nEUCLID and EUCLID is $4\Delta l$.

Optimum interference is required for measuring mirror displacement. This is defined by the fringe visibility, V, being at a maximum, with

$$V \equiv \frac{(I_{max} - I_{min})}{(I_{max} + I_{min})}, \tag{2.30}$$

where I_{max} and I_{min} are the intensity values of the interfering output beam.

In Section 2.1.1, two photodiodes were used to determine the direction of the mirror displacement. Plotting these two signals against each other in X-Y mode on an oscilloscope

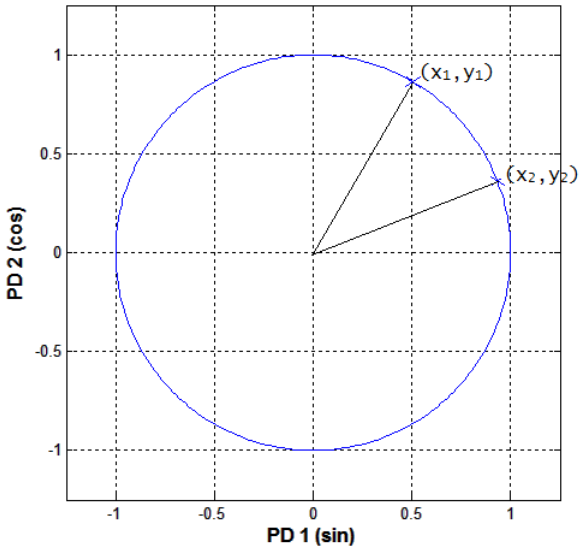

Figure 2.3: A Lissajous figure created by two photodiode signals, showing the initial and final positions of the signal, (x_1, y_1) and (x_2, y_2), having completed a full revolution of the figure.

yields a *Lissajous pattern*, shown in Fig. 2.3. As one of the mirrors is displaced the arm length changes, altering the phase proportionately. If a position on the circle is monitored any mirror motion causes this point to move around the Lissajous pattern from an initial to a final position: (x_1, y_1) to (x_2, y_2) in Fig. 2.3.

The angle between the two points on the circle is the phase difference between the two signals, ϕ

$$\phi = \arctan\left(\frac{y_2}{x_2}\right) - \arctan\left(\frac{y_1}{x_1}\right). \tag{2.31}$$

A complete revolution of the Lissajous pattern is equivalent to an arm length difference, Δl (or a mirror displacement) of $\lambda/2$ in Fig. 2.1, or $\lambda/4$ for both EUCLID and nEUCLID.

The arm length difference can be calculated by rearranging the phase term, ϕ, in Eq. (2.24) to give

$$\Delta l = \frac{\phi}{2\pi}\frac{\lambda}{2}, \tag{2.32}$$

and thus the displacement moved by the mirror (the other mirror in the interferometer is stationary).

This method is used to calculate displacement for both nEUCLID and EUCLID.

2.2.5 Straight or Circular Fringes?

Both straight and circular fringes are possible with an interferometer. Using a simple Michelson interferometer again as a starting point, as pictured in Fig. 2.1, the occurrence of a type of fringe pattern gives an indication of the mirror alignment in each arm.

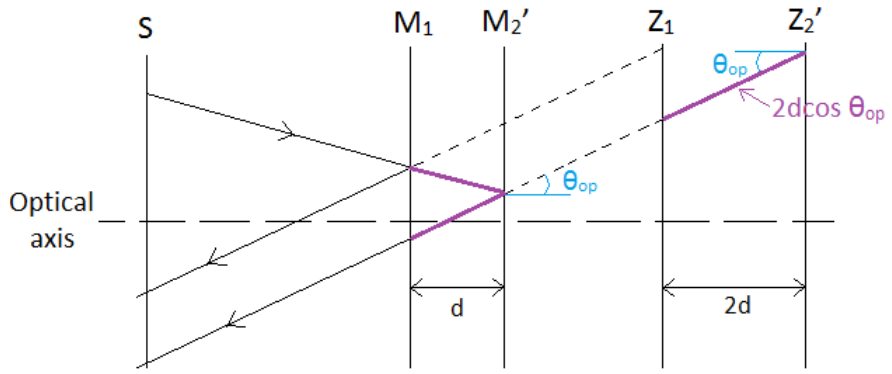

Figure 2.4: A Michelson interferometer on a shared axis. S is the source plane, M_1 and M_2' the two mirrors, and Z_1 and Z_2 are the imaginary source planes for each mirror. The purple line shows the path difference, $2d\cos\theta_{op}$.

Imagine each component of a Michelson interferometer on the same axis, starting with the source, then the two mirrors, M_1 and M_2, as shown in Fig. 2.1. M_2 has been moved into the same axis as the source and M_1 by using the virtual image of M_2, denoting it as M_2' to differentiate between them, as shown in Fig. 2.4.

Observing a ray leaving the source plane, S, and hitting M_1 and reflecting. This same ray also hits M_2', having been split by the beam splitter, but travels an extra distance before reflection as the arms are not of equal length; the mirrors are separated by a distance d. The two rays can be traced back to their virtual source planes, Z_1 and Z_2 respectively. The separation between these two planes is $2d$. Using simple trigonometry, the extra distance travelled by the second ray to M_2' can be calculated as approximately $2d\cos\theta_{op}$, where θ_{op} is the angle the incoming ray makes with the optical axis.

Using Eq. (2.17), for the maximum intensity, the optical path difference between the rays is

$$m\lambda = 2d\cos\theta_{op} \tag{2.33}$$

Equation (2.33) holds for any ray on the source plane entering between the source, S, and the optical axis; the phase difference depends only on the radius from the optical axis. This means the pattern is axially symmetric, thus creating **circular fringes**, as pictured in Fig. 2.6a. Both mirrors need to remain parallel for this pattern to occur (perpendicular when unfolded). As M_2' is moved towards M_1, d decreases until $d = 0$, where one large central fringe is left. This is what is achieved in nEUCLID, as it gives maximum fringe visibility.

To achieve **straight fringes** as pictured in Fig. 2.6b, M_2' is tilted by an angle α with respect to M_1, as shown in Fig. 2.5. As before the two mirrors are on the same axis, M_2' remaining as the virtual image of M_2.

Due to this tilt the ray travelling to M_2' has an extra path length, as well as that caused by the difference in arm lengths, d. This extra path length increases as the beam strikes the mirror further from the tilt axis of M_2', causing the phase to increase. The phase cycles from 0 to 2π, thus constructive and destructive fringes are alternately observed up the mirror. Along the mirror, however, the phase remains constant as d remains constant,

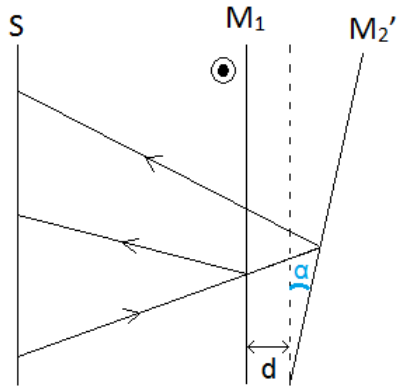

Figure 2.5: The two mirrors of a Michelson interferometer in one plane. S is the source plane, and M_1 and M_2' are the two mirrors, where M_2' is tilted by an angle α with respect to M_1.

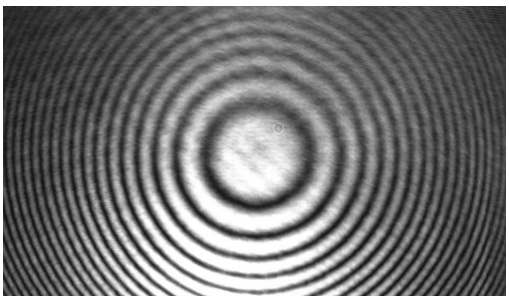

(a) Photograph of circular fringes from an infra-red Michelson interferometer

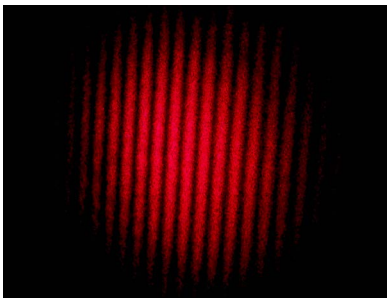

(b) Photograph of straight fringes using a HeNe laser [12]

Figure 2.6: In comparison to radially symmetric circular fringes (Fig. 2.6a), straight line fringes are symmetric along the axis of mirror tilt (Fig. 2.6b).

thus the fringe is straight in the direction perpendicular to the page in Fig. 2.5.

2.2.6 The Benefit of Three Signals

A third photodiode can be used with the initial two to remove an offset in the signals. The three photodiode signals can be represented as

$$I_1 = a\cos\phi + b, \tag{2.34}$$

$$I_2 = a\sin\phi + b, \tag{2.35}$$

$$I_3 = -a\cos\phi + b, \tag{2.36}$$

where a is the amplitude of each signal, and b is the offset for each signal.

The offset is removed by subtracting one signal from the other to give

$$S_1 = I_1 - I_2, \tag{2.37}$$

$$S_2 = I_2 - I_3, \tag{2.38}$$

By subtracting the signals from each other the Lissajous pattern is centred on the origin.

The phase is calculated using the arctangent function given in Eq. (2.31), but using the two signals above, Eq. (2.37) and Eq. (2.38):

$$\phi = \arctan\left(\frac{S_1}{S_2}\right), \tag{2.39}$$

All of the calculations using three photodiodes (from Eq. (2.34) to Eq. (2.38)) are computed in the electronics box via the Field Programmable Gate Array (FPGA), as described in Section D.2.

2.3 Homodyne vs. Heterodyne Detection

There are two principal types of interferometers: heterodyne and homodyne. A heterodyne interferometer uses a dual-frequency beam, whereas a homodyne interferometer uses a beam of single frequency.

An explanation of the fundamental features of homodyne and heterodyne interferometers will be discussed in this section.

2.3.1 Homodyne Interferometry

The Michelson interferometer described in Section 2.1 is an example of a homodyne interferometer. However, the use of a half-silvered mirror can allow light to travel back to the light source (usually a laser), thus causing instabilities in the beam. As mentioned in Section 2.1, there is also no way to monitor the direction of the mirror motion. Figure 2.7 shows a basic homodyne interferometer design, including the extra apparatus required for phase quadrature measurements.

The laser beam of single frequency travels through a polarising beamsplitter (PBS), and is separated into the two polarisation components. One component is transmitted to mirror 1 (M1), the other reflected to mirror 2 (M2); both pass through a quarter wave plate (QWP) within their respective arms. The QWP changes the linearly polarised laser light to circularly polarised, and then back to linearly polarised light on return from the mirror at the end of each arm. This rotation of the plane of polarisation causes the initially transmitted beam to be reflected, and vice versa for the initially reflected beam. The two beams recombine to pass through the non-polarising beamsplitter (NPBS), where they are split again (50% intensity in each new beam). The transmitted beam travels to photodiode (PD)1, whilst the reflected beam passes through a second quarter wave plate to PD2, causing this beam to be $\pi/2$ out of phase with PD1.

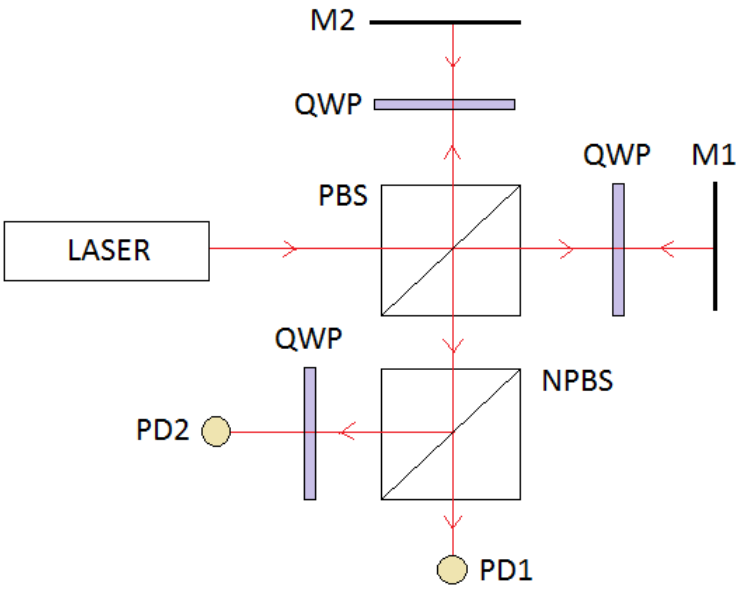

Figure 2.7: Schematic diagram of a basic homodyne interferometer, with in-quadrature apparatus for measurement of mirror motion direction.

2.3.2 Heterodyne Interferometry

A heterodyne interferometer has a source that emits a laser beam of two superposed frequencies, f_1 and f_2, that have orthogonal polarisations and are described by

$$E_1 = A_1 \cos\left(2\pi f_1 t + \phi_1\right), \tag{2.40}$$

$$E_2 = A_2 \cos\left(2\pi f_2 t + \phi_2\right), \tag{2.41}$$

where A is the amplitude and ϕ is the initial phase of each beam.

The interferometer has two arms, like the homodyne interferometer, but a third is created before the beam enters the PBS. This part of the beam is separated straight after the laser to create a reference signal (see Fig. 2.8). A polariser (P) at 45° is placed in this arm to create interference at the reference photodiode, PD1, by causing one frequency to be out of phase with the other. The transmitted beam travels on into the PBS, where the two frequencies are separated into each arm, as the polarisation components were in the homodyne interferometer. The beams reflect off their respective mirrors and recombine to travel to the measurement photodiode, PD2. A second polariser at 45° to the polarisation axes of the beams is placed in front of PD2, to again create interference between the two frequencies.

If the mirror in one of the arms moves, the signal gains an extra phase, $\phi(t)$. The signal at the reference photodiode (PD1) is

$$E_1 = A_1 \cos[2\pi\left(f_1 - f_2\right)t + (\phi_1 - \phi_2)], \tag{2.42}$$

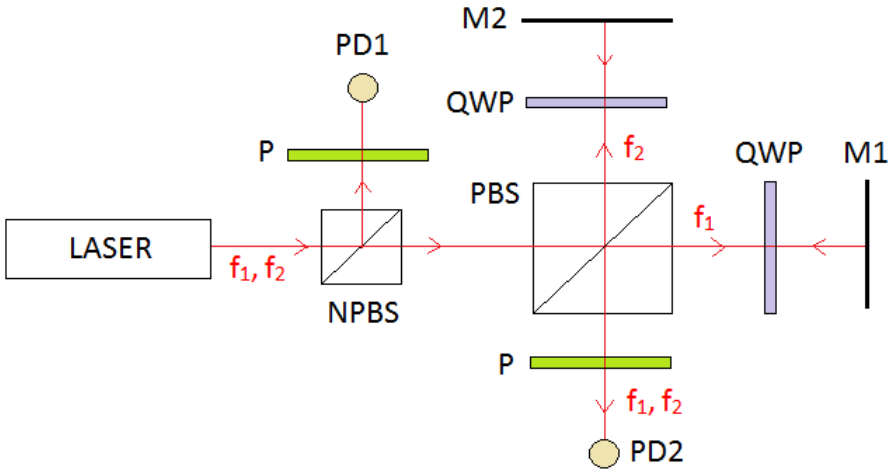

Figure 2.8: Schematic diagram of a basic heterodyne interferometer, with in quadrature apparatus for measurement of mirror motion direction.

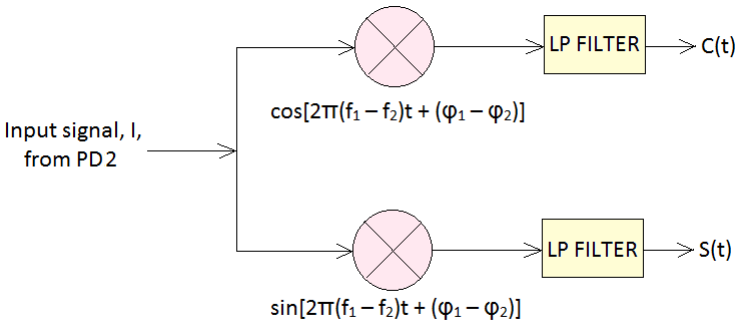

Figure 2.9: Diagram showing the synchronous demodulation and low-pass filtering (LP FILTER) of the heterodyne signal from the measurement photodiode, PD2 [13].

and the signal at the measurement photodiode (PD2) is

$$E_2 = A_2 \cos[2\pi\,(f_1 - f_2)\,t + (\phi_1 - \phi_2) + \phi\,(t)]. \tag{2.43}$$

Using the principle of superposition and Eq. (2.11), the intensity, I, at PD2 is

$$I = I_1 + I_2 + 2\sqrt{I_1 I_2}\cos[2\pi\,(f_1 - f_2)\,t + (\phi_1 - \phi_2) + \phi\,(t)], \tag{2.44}$$

where I_1 and I_2 are the intensity of each beam.

The signal at PD2 (Eq. (2.44)) is "synchronously demodulated", i.e. the signal is split into two and multiplied by $\cos[2\pi\,(f_1 - f_2)\,t + (\phi_1 - \phi_2)]$ and $\sin[2\pi\,(f_1 - f_2)\,t + (\phi_1 - \phi_2)]$, as shown in Fig. 2.9. The cosine and sine signals come from PD1, where the reference

polariser has shifted one part of the signal by $\pi/2$ to give the sine signal. Thus,

$$\begin{aligned} I\cos[2\pi\left(f_1-f_2\right)t+\left(\phi_1-\phi_2\right)] &= \left(I_1+I_2\right)\cos[2\pi\left(f_1-f_2\right)t+\left(\phi_1-\phi_2\right)] \\ &+ 2\sqrt{I_1 I_2}\cos[2\pi\left(2\left(f_1-f_2\right)t+2\left(\phi_1-\phi_2\right)+\phi\left(t\right)\right)] \\ &+ 2\sqrt{I_1 I_2}\cos[2\pi\phi\left(t\right)], \end{aligned} \tag{2.45}$$

and

$$\begin{aligned} I\sin[2\pi\left(f_1-f_2\right)t+\left(\phi_1-\phi_2\right)] &= \left(I_1+I_2\right)\sin[2\pi\left(f_1-f_2\right)t+\left(\phi_1-\phi_2\right)] \\ &+ 2\sqrt{I_1 I_2}\sin[2\pi\left(2\left(f_1-f_2\right)t+2\left(\phi_1-\phi_2\right)+\phi\left(t\right)\right)] \\ &+ 2\sqrt{I_1 I_2}\sin[2\pi\phi\left(t\right)]. \end{aligned} \tag{2.46}$$

Both Eq. (2.45) and Eq. (2.46) contain high frequency terms – $\left(f_1-f_2\right)t$ and $2\left(f_1-f_2\right)t$. By low-pass filtering the two signals the high frequency terms are removed, leaving only the signals containing the phase shift from the mirror motion, $\phi\left(t\right)$:

$$\begin{aligned} C(t) &= 2\sqrt{I_1 I_2}\cos 2\pi\phi\left(t\right), \\ S(t) &= 2\sqrt{I_1 I_2}\sin 2\pi\phi\left(t\right). \end{aligned} \tag{2.47}$$

The phase is extracted from these signals in a similar way to the homodyne method described in Section 2.2.4: using the arctangent of the two signals

$$\phi\left(t\right) = \frac{1}{2\pi}\arctan\left[\frac{S(t)}{C(t)}\right] \tag{2.48}$$

As discussed in Section 2.2.4, the phase is proportional to the displacement of the mirror, Δl. Thus rearranging Eq. (2.32) gives the displacement from the phase:

$$\phi\left(t\right) = \frac{2\pi}{\lambda}2\Delta l \tag{2.49}$$

where λ is the wavelength of the laser.

For more detail on homodyne and heterodyne interferometers, please refer to Hecht [11, Chapters 7 and 9], Gåsvik [13, Section 3.6], and Bass [14, Chapter 21].

2.4 Previous Polarising Interferometers

One of the first polarisation-based homodyne interferometers to use electronic subtraction for in-quadrature measurements was created by Downs and Raine in 1978 [15]. The design is simple and contains few components, using two polarisation states to determine displacement and is shown in Fig. 2.10. The interferometer achieves a precision of movement

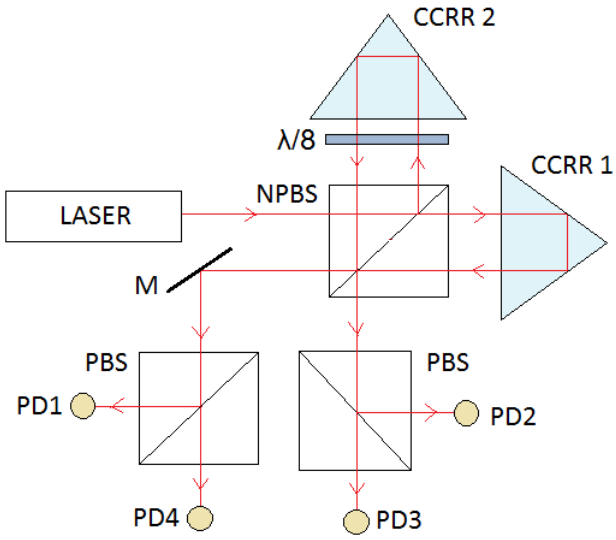

Figure 2.10: Schematic diagram of the Downs and Raine homodyne interferometer [15]. Note the use of CCRR in the arms, rather than mirrors.

of 0.1 µm (the measurement noise in the system is not quantified), and correctly tracks fringes even with 99% intensity loss in one arm [15].

The design is a Michelson interferometer and is similar to the layout described in Section 2.1, but uses a cube-corner retro-reflector (CCRR) in each arm rather than a mirror. This is to offset the beam to stop it returning back into the frequency-stabilised HeNe laser and destabilising it. It also means the interferometer is insensitive to any potential tilt of the reflecting components, which is not the case for conventional mirrors in this type of set-up. However, using CCRRs means the device is sensitive to transverse motion, as shown in Fig. 2.11.

A $\lambda/8$ plate in one arm provides a $\pi/2$ phase difference between the two signals PD2 and PD3 (as the beam passes through this plate twice). Thus, when PD3 has maximum intensity, PD2 is halfway between minimum and maximum.

A characteristic of the glass NPBS is that when a beam is reflected by the beamsplitter it gains a phase shift of $\pi/2$. The beam from CCRR2 that travels to PD4 and PD1 is reflected twice; the beam travelling to PD2 and PD3 is reflected once and transmitted once. At PD4 and PD1 there is an accumulated π phase shift between the transmitted and reflected beam, whilst the phase shift between the beams at PD2 and PD3 has been cancelled out. This means PD4 has minimum intensity when PD3 is at a maximum.

The signals are submitted to the subtraction process (PD3 - PD4 and PD3 - PD2), leaving two signals to create a Lissajous pattern from which to extract the phase, as explained in Section 2.2.4. PD1 verifies the result of the subtraction process by replacing PD2, if necessary.

The stability and simplicity of this interferometer inspired the design of the University of Birmingham interferometers.

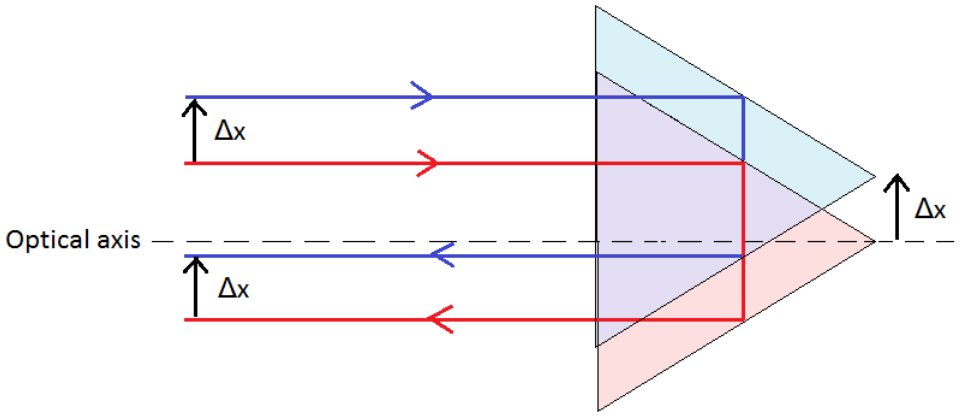

Figure 2.11: A diagram of a CCRR showing how transverse motion of the CCRR affects the position of the returning reflected beam. The scale has been exaggerated for ease of understanding.

Another design that inspired the University of Birmingham interferometers is that of Greco et al [16] (shown in Fig. 2.12), who used an algorithm to compute in-quadrature measurements.

A 632.8 nm HeNe laser is used as the source, and the design is similar to the simple homodyne interferometer described in Section 2.3.1: two arms, each containing a mirror and a QWP; the beams recombine and are separated by a NPBS to three photodiodes, one with a second QWP in front to provide the $\pi/2$ phase difference signal.

However, instead of orientating the source specifically to align the polarisation for the first PBS, a half wave plate (HWP) is placed after the laser. This rotates the polarisation by 45°, thus splitting the beam into two equal beams through the PBS; one vertically polarised, the other horizontally polarised.

The other difference is the use of the fourth photodiode. Upon exiting the NPBS, the beam is split into two. The transmitted beam travels through a QWP and onto another PBS to two photodiodes. The reflected beam travels to another PBS and is separated to two more photodiodes. This means PD1 and PD3 are in quadrature, as are PD2 and PD4. As with Downs et al, the two extra photodiodes produce a second means of verifying the mirror motion, as well as monitoring any laser power instabilities. However, the two sets of signals are combined via an algorithm to remove any signal drifts from the laser. These signal drifts come from intensity noise in the laser, which at low laser power is limited by the shot noise. The shot noise is discussed further in Section 2.6.1.

The use of a second pair of photodiodes in quadrature and a corresponding algorithm to monitor laser instabilities is present in all three Birmingham interferometer designs.

It is worth mentioning that all the homodyne interferometers described above measure incremental displacement; all motion is measured with respect to the interferometer. This means that were something to cause the interferometer to stop measuring for a period of time when it began again the measurement would be from zero, no matter

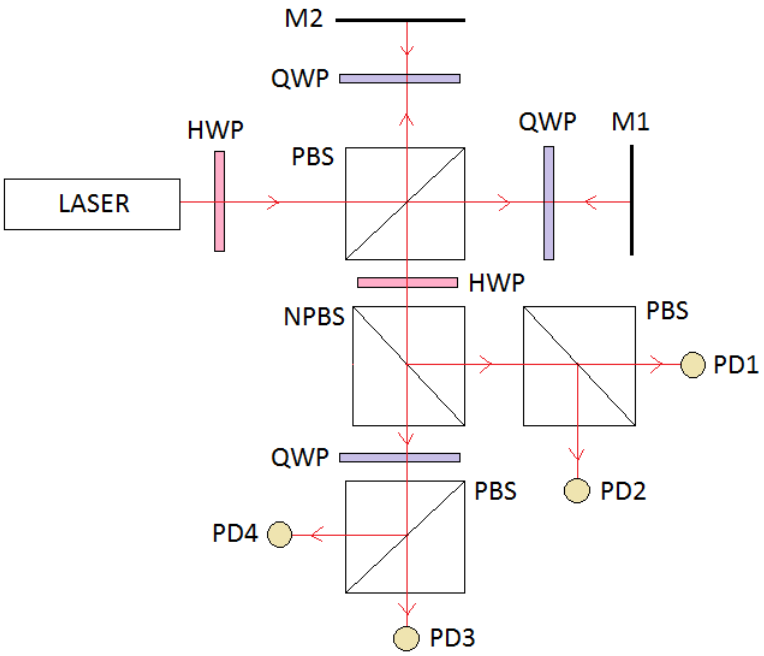

Figure 2.12: Schematic diagram of the Greco et al homodyne interferometer [16].

the position of the target, and would invalidate any previous measurement. To avoid this problem in real-world applications absolute displacement is sometimes necessary. The University of Birmingham interferometers, EUCLID and ILIAD, are currently both incremental-displacement interferometers, as this was what was required at the time. Section 7.2 discusses how nEUCLID could be made absolute in future.

2.5 Interferometers at the University of Birmingham

Three different polarising homodyne interferometers have been designed and built at the University of Birmingham: EUCLID, ILIAD and nEUCLID. All three are immune to tilt of the target mirror, as each has a cat's eye lens system built into their design.

2.5.1 EUCLID

The first interferometer to be built at the University of Birmingham was the Easy to Use Compact Laser Interferometric Device (EUCLID) (Fig. 2.13). This was designed and produced by Speake, Peña Arellano and Aston in 2011 [9, 10, 17]. It is a compact, tilt-immune interferometer which uses a vertical-cavity surface-emitting laser (VCSEL) to produce visible wavelength, 667 nm. EUCLID has a working distance of 6 mm and a working range of ±3 mm (see Fig. 4.8 for definitions). It is 60 mm × 22.5 mm × 56 mm, and has a mass of only 131 g [18]. EUCLID was built as a relative displacement sensor for the Advanced Laser Interferometer Gravitational-wave Observatory (aLIGO) to monitor movement of the test masses. This drove the design of EUCLID towards a compact size, as well as a high sensitivity of $50\,\mathrm{pm}/\sqrt{\mathrm{Hz}}$ at 1 Hz (in a vacuum) [18].

(a) EUCLID, external

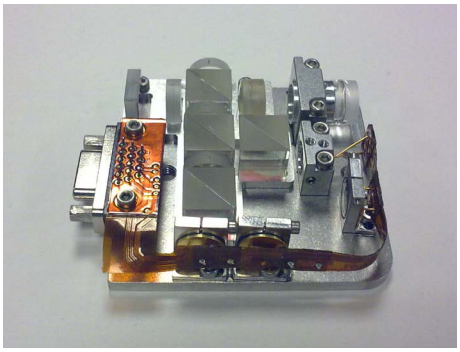

(b) EUCLID, internal (aluminium cover removed)

Figure 2.13: EUCLID: External and internal photographs [19]

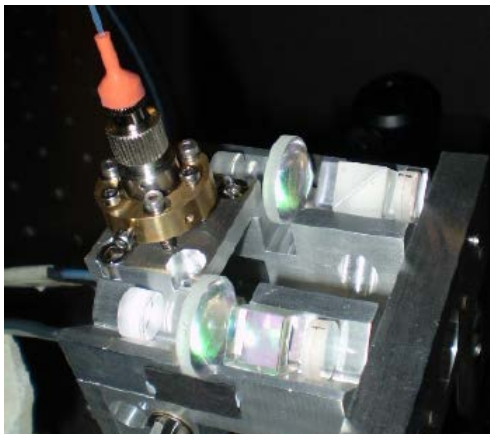

Figure 2.14: The room-temperature ILIAD in the laboratory [22, pp. 66].

A more detailed discussion of EUCLID and its relevance to nEUCLID will be discussed in appendix D.

2.5.2 ILIAD

The design and subsequent building of EUCLID led to a second interferometer being constructed – the Innovative Laser Interferometric Angular Device (ILIAD), shown in Fig. 2.14. Two have been constructed: a room-temperature version, and a cryogenic version. The cryogenic ILIAD was created to measure the angular rotation of the test masses used in the Inverse Square Law experiment [20], whilst the room temperature ILIAD measures angular displacement of the torsion balance in the G experiment [21] [22]. Both experiments are currently being undertaken in the School of Physics and Astronomy at the University of Birmingham. ILIAD uses a 1550 nm distributed feedback (DFB) laser, and is 58 mm × 54 mm × 48 mm in dimension [22, pp. 63], again relatively compact. It has a tilt range of ±1°, and a sensitivity of 50 prad/$\sqrt{\text{Hz}}$ at 1 Hz (in a vacuum) [23].

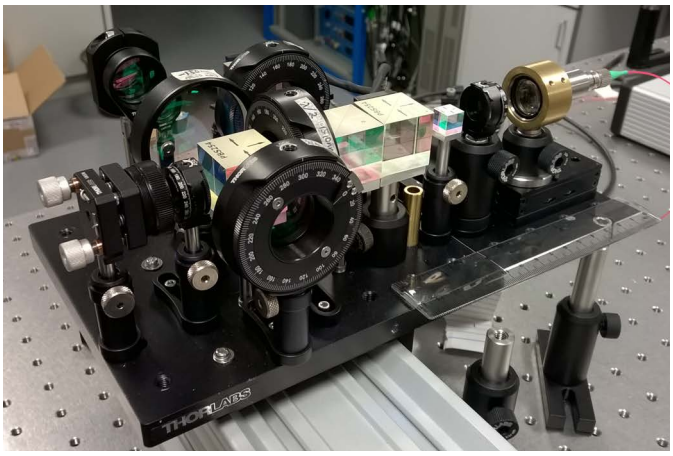

Figure 2.15: nEUCLID in the laboratory.

2.5.3 nEUCLID

The new Easy to Use Compact Laser Interferometric Device (nEUCLID) (Fig. 2.15) is very similar in design to that of EUCLID. Like EUCLID, it measures relative displacement, albeit over a larger range. However, like ILIAD, nEUCLID uses a 1550 nm DFB laser as its source, as will be discussed in Section 4.4. nEUCLID is insensitive to $\pm 0.35°$ of tilt of the target mirror, and has a working distance of 660 mm and a working range of ± 120 mm. It has a sensitivity of $420\,\mathrm{pm}/\sqrt{\mathrm{Hz}}$ at 1 Hz (in air).

Further details of nEUCLID will be described in Chapter 4.

2.6 Noise Sources in Interferometers

Like all metrology instruments, interferometers are subject to sources of noise that affect measurements made with them. Below are the most relevant noise sources for nEUCLID, the values of which are given in Section 5.7.

2.6.1 Shot Noise

The shot noise is caused by statistical fluctuations in the discrete arrival times of the photons from the laser. The number of photons arriving at the photodiodes will vary slightly over time; these fluctations are shot noise. Equation (2.50) [9] can be used to calculate the shot noise in the system, σ_ν,

$$\sigma_\nu = \sqrt{2ei_{pd}}R_f G, \tag{2.50}$$

where e is the charge of an electron, i_{pd} is the photocurrent of the photodiodes, R_f is the transimpedance amplifier gain, and G is the voltage gain.

This can be converted into a displacement sensitivity, N_ν, via

$$N_\nu = \frac{\sigma_\nu}{V}\frac{1}{2\pi}\frac{\lambda}{4}, \tag{2.51}$$

where V is the approximate radius of the Lissajous pattern produced by the interferometer.

2.6.2 Frequency Noise

Fluctuations in phase can result in displacement noise in interferometers of unequal armlengths, such as nEUCLID. Phase fluctuations can appear as oscillations in the frequency of the laser. These fluctuations are determined by the laser linewidth. The laser linewidth relates to the power spectral density (PSD) of the laser frequency ν as

$$L^2 \approx \int_{f_1}^{f_2} S_\nu(f) df \tag{2.52}$$

where L is the laser linewidth, and $S_\nu(f)$ is the one-sided PSD of the laser frequency. In practice, the choice of frequency band $[f_1, f_2]$ in estimating the linewidth from a measured PSD depends on the band over which frequency noise dominates.

2.6.3 Thermal Noise

Johnson noise – also known as thermal noise – arises from thermal agitation of the electrons inside a resistor when a voltage is applied. This causes the output voltage to vary randomly, creating extra noise in the electronics for nEUCLID. As it is temperature dependent, the temperature of the surroundings, T, also affect the variations.

$$N_J = \sqrt{\frac{4k_B T}{Rf}} R_f G \frac{\lambda}{8\pi} \tag{2.53}$$

where k_B is the Boltzmann constant, and T is the average temperature of the laboratory.

2.6.4 ADC Noise

analogue to digital converter (ADC) noise is present in all ADC circuits due to resistor noise and thermal noise. The ADC noise for nEUCLID (ADC_V) is the same as for EUCLID: $3.24 \times 10^{-7}\,\mathrm{V}/\sqrt{\mathrm{Hz}}$ (16-bit resolution) [24]. Using this value the displacement noise can be calculated:

$$N_{ADC} = \frac{ADC_V}{ADC_U}\frac{\lambda}{8\pi V_{in}} \tag{2.54}$$

where ADC_U is the ADC utilisation and V_{in} is the ADC voltage input range [9].

2.7 Competing Technologies

There are several methods for using lasers to measure distance:

- *Time-of-flight method*: Also known as the "pulse method", this is used for measuring extremely large distances, usually tens of metres to several kilometres. The time of flight of a pulse of laser light is measured from the measurement device to a target and back. Typical accuracies are a few centimetres [25, 26], however, recent developments have lead to an increase in measurement accuracy of 0.01 mm [27].
- *Triangulation method*: Capable of measuring distances of up to 1 m, this method uses a collimated laser beam to illuminate the measurement object, and triangulation to calculate the object distance. Whilst this technique is low cost and capable of fast measurement, the sensor-head scales with the distance, thus large distances are infeasible [25].
- *Phase shift method*: This method uses an intensity-modulated beam, and is better for more diffuse objects. The range is still large; several to tens of metres for millimetre accuracy [26].
- *Interferometers*: Distance measurements are limited by the interferometer design. However, the accuracy of the result is much higher than the above techniques; it is of the order of the wavelength used in the device [28], thus the motivation to use them for space applications.

Different displacement-measuring interferometers will now be briefly investigated, to give a wider comparison of applications for displacement-measuring interferometers. Each example describes how the method is not suitable for the applications described in this thesis.

Measuring surface roughness: A stabilised, linearly polarised 633.0 nm homodyne interferometer measures the surface roughness of polymer materials, with a sample size 10.0 mm in height and diameter. The resolution achieved by the device is 0.6 nm, with a total measured displacement of 10.0 µm [29]. However, the reference and measurement arms are both 25 mm, and the device is not tilt-insensitive as the sample is mounted and vibrationally isolated.

Measuring ultrasonic waves: A stabilised, linearly polarised 632.8 nm homodyne interferometer measures the displacement of an aluminium plate caused by high-amplitude ultrasonic waves. From this measurement the ultrasonic wave can be characterised. The device makes use of the quadrature method described in Section 2.1.1 to determine the direction of displacement, and achieves nanometre resolution [30], yet is not tilt-immune.

Measuring translational & angular displacement: The Istituto Nazionale di Ricerca Metrologica (INRiM) has produced a heterodyne device for the European Space Agency (ESA) that measures the relative attitude of satellite components. The Compact Optical Attitude Transfer System (COATS) uses three independent metrology systems inside an

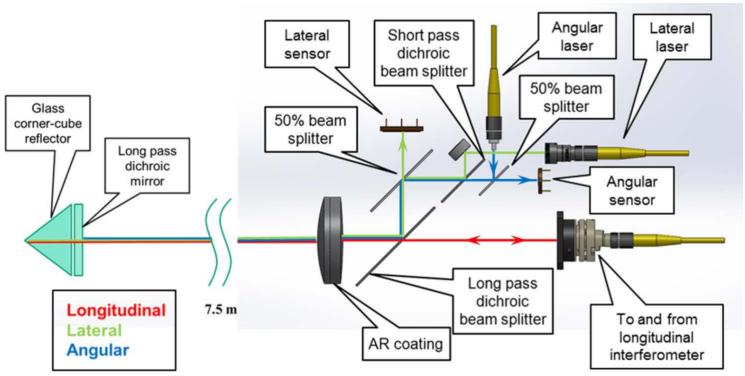

Figure 2.16: The optical schematic of COATS, with the optical head on the right, and the passive target on the left. The laser paths are shown in red, green, and blue respectively for the 1542 nm, 850 nm, and 780 nm wavelengths [31].

optical head to monitor a passive target. Each system contains a laser source of a different wavelength (1542 nm, 850 nm, and 780 nm). These measure three translational and two angular degrees of freedom. The maximum working distance between the optical head and target is 7.5 m (as defined by the Wavemill mission described in Section 6.1.2). The resolution of the translational coordinates is 5×10^{-6} m, and 1° for the two angular coordinates [31].

It is worth mentioning here the argument between tilt immunity and long working distance. Clearly, for very long armlengths the tilt of the target is irrelevant, as the optics would have to scale up in size making the design infeasible. Thus, a working distance of 100 m, as described by COATS, does not give tilt immunity of the target. The removal of tilt immunity for very long target lengths is discussed for nEUCLID in Section 6.1.2

COATS is a competing technology with the device described in this thesis, nEUCLID. The properties of COATS will be compared in detail with those of EUCLID and nEUCLID in Chapter 7.

2.8 Summary

An interferometer causes two beams of light to interfere from two arms that each contain a mirror. Moving one of these mirrors produces a change in phase in the interference pattern, measured by photodetectors, from which the mirror displacement can be calculated.

There are two main types of interferometer: heterodyne and homodyne. A heterodyne interferometer uses two frequencies to measure mirror displacement, whilst a homodyne interferometer uses only one.

At the University of Birmingham, two tilt-immune homodyne interferometers have been built; EUCLID and ILIAD. Working from these, the third device, nEUCLID – the subject of this thesis – has been developed, which is tailored towards space applications. Space applications are sensible for this interferometer as it is small, light-weight, has a very low power consumption and is capable of working over distances of several metres.

Chapter 3

THE NEW CAT'S EYE

The calculations derived in this chapter also appear in Appendix F. Some have been separated into smaller steps for further explanation or refer to other sections within this thesis. The other equations are trivial, e.g. Eq. (3.2)*, unless specifically referenced.*

3.1 What is a Cat's Eye?

A cat's eye is a retroreflector – a device that reflects rays of light back to their source with minimum scattering. The simplest design consists of a lens and a mirror, arranged so that the focal surface of the lens coincides with the mirror surface [32].

The basic function of a cat's eye is to reflect an incoming beam such that it is returned parallel to its incoming path, irrespective of the angle between the incoming beam and the optic axis of the cat's eye. Snyder showed that the cat's eye has a plane (which we will refer to as the *sweet plane*) in front of the convex lens where the radial position of the outgoing beam remains fixed, irrespective of the angle that the beam makes with the optic axis [32]. It is upon this premise that the tilt-immune interferometers at Birmingham were built.

3.2 The Conventional Cat's Eye

The cat's eye design used in EUCLID [10] is a standard design [32] of two lenses and a mirror, and as such is referred to as a conventional cat's eye (CCE) [33].

The role of the CCE within EUCLID is to ensure that the reference and target beams exiting the optical components remain parallel when the target mirror is tilted. This is achieved by designing the cat's eye such that the input plane and output plane are self-conjugate; if an object is placed at the input plane of the CCE an inverted image is produced at the object location. An input plane satisfying this condition is known as a *sweet plane*.

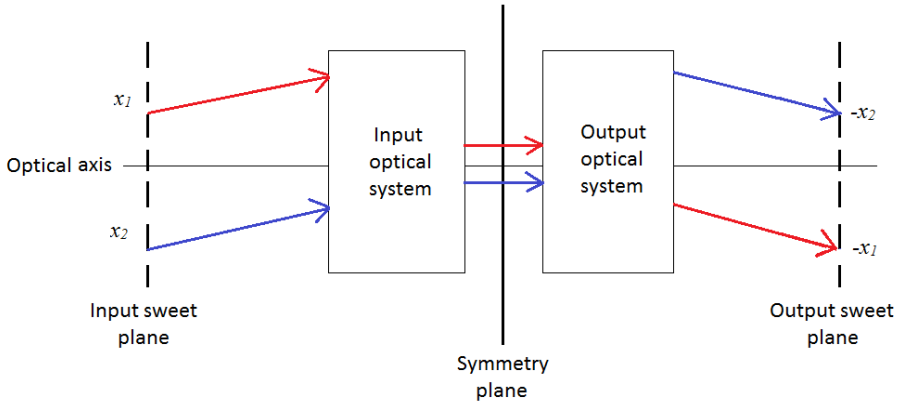

Figure 3.1: Schematic showing how rays are processed by a cat's eye, travelling from the sweet plane and reflecting back to it.

Thus, if a light ray incident on the input plane at angle θ and position x, should pass through the CCE it would arrive back at the input plane at position $-x$ with the angle of incidence $-\theta$, as shown in Fig. 3.1.

This result can be shown using simple ABCD matrices (also known as *ray tracing matrices*). These matrices represent individual optical components, and when multiplied by a vector representing a light ray trace the ray through the optical component. E.g., for a simple lens of focal length, f, the system is described with a matrix representing the lens, M_f

$$M_f = \begin{pmatrix} 1 & 0 \\ -\frac{1}{f} & 1 \end{pmatrix} = \begin{pmatrix} A & B \\ C & D \end{pmatrix} \tag{3.1}$$

A CCE has a matrix Eq. (3.2):

$$M_{CCE} = \begin{pmatrix} -1 & 0 \\ 0 & -1 \end{pmatrix} \tag{3.2}$$

Tracing an input vector of radial height, r_{in}, and angle, θ_{in}, through the CCE gives an output vector of equal but negative radial height and incidence angle (Eq. (3.3)).

$$\begin{pmatrix} r_{out} \\ \theta_{out} \end{pmatrix} = \begin{pmatrix} -1 & 0 \\ 0 & -1 \end{pmatrix} \cdot \begin{pmatrix} r_{in} \\ \theta_{in} \end{pmatrix} = \begin{pmatrix} -r_{in} \\ -\theta_{in} \end{pmatrix} \tag{3.3}$$

The cat's eye system also ensures that the phase accumulated by all the rays passing through the system is identical irrespective of input angle, ensuring no extra path difference is gained to give an erroneous displacement measurement.

In the CCE the primary lens, L_1, is a convex lens of focal length, f_1. The secondary lens, L_2, is either a positive or negative lens, with focal length, f_2. The distance, d, between the primary and secondary lenses is equal to f_1. In both nEUCLID and EUCLID a plane mirror is placed behind the secondary lens, to reflect the beam back out of the cat's eye. It is worth reiterating here that a CCE can also be constructed from a lens and

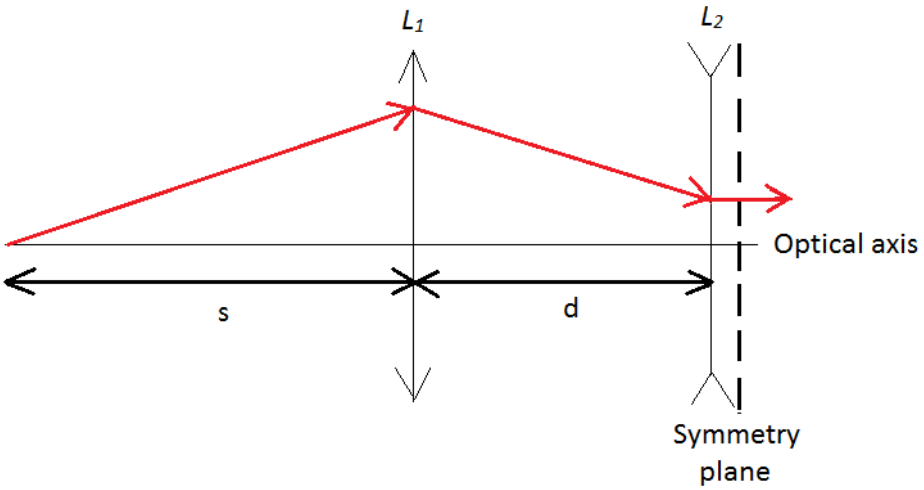

Figure 3.2: Schematic diagram of the CCE system used in EUCLID. The primary lens, L_1, is a convex lens of focal length, f_1. The secondary lens, L_2, is either a positive or negative lens, with focal length, f_2. The distance, d, is equal to f_1 [33]

a concave/convex mirror; there is no need for the secondary lens and a plane mirror [32].

The figure of merit, R, is used to compare the performance of the two cat's eyes described in this thesis. R is the ratio of s/d; the working distance, s, divided by the separation of the primary and secondary lenses, d.

3.3 The Pseudo Cat's Eye

3.3.1 The Optics

The CCE has limitations; it cannot be used in interferometers with highly unequal arm lengths due to a limit on s [33]. nEUCLID requires a long working distance, with tilt immunity. This required a new design of cat's eye to be developed - the pseudo cat's eye (PCE).

The PCE uses two lenses and a mirror, like the CCE (see Fig. 3.3). However, it does not behave as a perfect retroreflector; there is an extra off-diagonal term, δ. A PCE can be described by the matrix, M_{PCE}, [33]:

$$M_{PCE} = \begin{pmatrix} -1 & \epsilon \\ \delta & -1 \end{pmatrix} \tag{3.4}$$

where ϵ represents an error in the output plane position with respect to the sweet plane.

If the target mirror in the interferometer is moved away from the sweet plane by a distance, $+z$, the resulting ABCD matrix, M_z becomes:

$$M_z = \begin{pmatrix} -1 + z\delta & \epsilon + z^2\delta - 2z \\ \delta & -1 + z\delta \end{pmatrix} \tag{3.5}$$

ϵ can be removed by moving the target mirror by a distance of $z = \epsilon/2$, setting ϵ to zero, thus it will not be considered any further in these calculations.

To find the output position where all the rays passing through the PCE are focused (thus finding the self-conjugate plane), the top right term in Eq. (3.5) ($z^2\delta - 2z$) is set to zero, as in a CCE. This yields two solutions, thus locations: one at $z = 0$ and one at $z = 2/\delta$. Having self-conjugate planes proves that the PCE works as a cat's eye. As described in [33], δ has units of mm^{-1} and is negative, thus the second conjugate plane position cannot be realised; one cannot place a mirror at this position and retain a useful interferometer design.

Using the solutions from setting the top right term in Eq. (3.5) to zero, the focal length of the PCE can be defined as:

$$f_{PCE} = \frac{2}{\delta} \tag{3.6}$$

This is shown in Fig. 3.4b.

If the object and image positions are not the same (i.e. have different z values), it can be shown that an object at infinity focuses at $z = 1/\delta$. If the PCE is modelled as a CCE with a diverging lens (focal length $-f$) on either side (to represent the unfolded system), the resulting system can be represented as a lens with effective focal length, F_{eff}, as shown in Eq. (3.7).

$$\begin{pmatrix} 1 & 0 \\ \frac{1}{f} & 1 \end{pmatrix} \cdot \begin{pmatrix} -1 & 0 \\ 0 & -1 \end{pmatrix} \cdot \begin{pmatrix} 1 & 0 \\ \frac{1}{f} & 1 \end{pmatrix} = \begin{pmatrix} -1 & 0 \\ \frac{1}{F_{eff}} & -1. \end{pmatrix} \tag{3.7}$$

The effective focal length of the system is equivalent to the original full matrix of the PCE, as shown in Eq. (3.8).

$$\begin{pmatrix} -1 & 0 \\ \frac{1}{F_{eff}} & -1 \end{pmatrix} \equiv \begin{pmatrix} -1 & 0 \\ \delta & -1. \end{pmatrix} \tag{3.8}$$

This means that

$$F_{eff} = \frac{1}{\delta} = \frac{f}{2}, \tag{3.9}$$

and so an object at infinity focuses at $1/\delta$. This effect is shown in Fig. 3.5b.

Whilst this focusing effect is negatable within nEUCLID, the methods for its removal are discussed in Section 5.5.

3.3.2 The Design

The PCE is very similar to the CCE in design, except the two lenses have been reversed in order: the primary lens, L_1 is now a concave lens, and the secondary lens, L_2 is now a convex lens, as shown in Fig. 3.3.

To design a functional PCE, the working distance of the system, s, and the focal lengths of the lenses, f_1 and f_2, must be chosen. Figure 3.4 shows how each of these values determines the others; this is described in greater detail in Appendix F.

The distance between the two lenses, d, and δ can be calculated from these three parameters

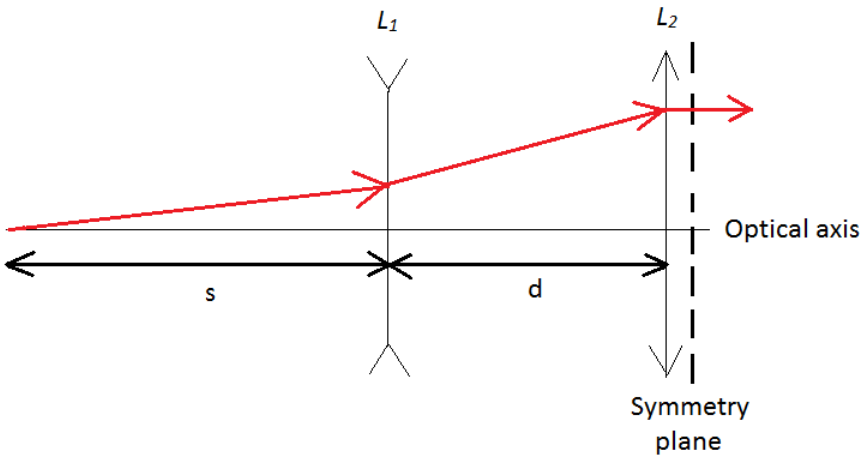

Figure 3.3: Schematic diagram of the PCE system, as used in nEUCLID. The primary lens, L_1, is a concave lens of focal length, f_1. The secondary lens, L_2, is a convex lens with focal length, f_2 [33].

by modelling the full PCE as individual ABCD matrix components: a space s, the diverging lens of focal length f_1, the space between the lenses d, and the converging lens of focal length f_2:

$$\begin{aligned} M_{out} &= \begin{pmatrix} 1 & 0 \\ \frac{1}{f_2} & 1. \end{pmatrix} \cdot \begin{pmatrix} 1 & d \\ 0 & 1 \end{pmatrix} \cdot \begin{pmatrix} 1 & 0 \\ \frac{1}{f_1} & 1 \end{pmatrix} \cdot \begin{pmatrix} 1 & s \\ 0 & 1 \end{pmatrix} \\ &= \begin{pmatrix} \frac{f_1+d}{f_1} & \frac{sd+sf_1+df_1}{f_1} \\ -\frac{f_1+d-f_2}{f_2 f_1} & -\frac{sd+sf_1-sf_2+df_1-f_1f_2}{f_2 f_1} \end{pmatrix} \end{aligned} \tag{3.10}$$

The beam travels through these components, reflects off the PCE mirror and returns back through the system, to give the final matrix, M_{back}:

$$\begin{aligned} M_{back} &= \begin{pmatrix} 1 & s \\ 0 & 1 \end{pmatrix} \cdot \begin{pmatrix} 1 & 0 \\ \frac{1}{f_1} & 1 \end{pmatrix} \cdot \begin{pmatrix} 1 & d \\ 0 & 1 \end{pmatrix} \cdot \begin{pmatrix} 1 & 0 \\ \frac{1}{f_2} & 1. \end{pmatrix} \cdot M_{out} \\ &= \begin{pmatrix} -\frac{sd+sf_1-sf_2+df_1-f_1f_2}{f_2 f_1} & \frac{sd+sf_1+df_1}{f_1} \\ -\frac{f_1+d-f_2}{f_2 f_1} & \frac{f_1+d}{f_1} \end{pmatrix} \end{aligned} \tag{3.11}$$

M_{out} does not look like the CCE matrix described by Eq. (3.2); both the top right $M_{out(1,2)}$ and bottom left matrix $M_{out(2,1)}$ components of M_{out} are non-zero. Starting with the top right component, if it is solved for d this yields two solutions:

$$M_{out(1,2)} = -\frac{sf_1}{s+f_1}, -\frac{sf_1 - sf_2 - f_1f_2}{s+f_1}. \tag{3.12}$$

The second solution is used, as it contains all three unknown parameters. Conversely, if $M_{out(2,1)}$ is solved for d the solutions are $-f_1$ and $-f_1 + f_2$, thus are not of use.

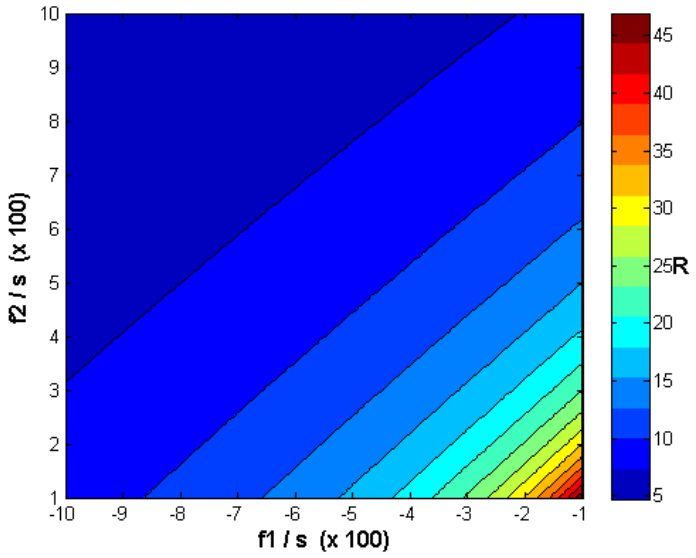

(a) Surface plot of the PCE as a function of the focal lengths f_1 and f_2, normalized by the distance between the diverging lens and the sweet plane, s. $R = s/d$, where d is the distance between the two PCE lenses. [33]

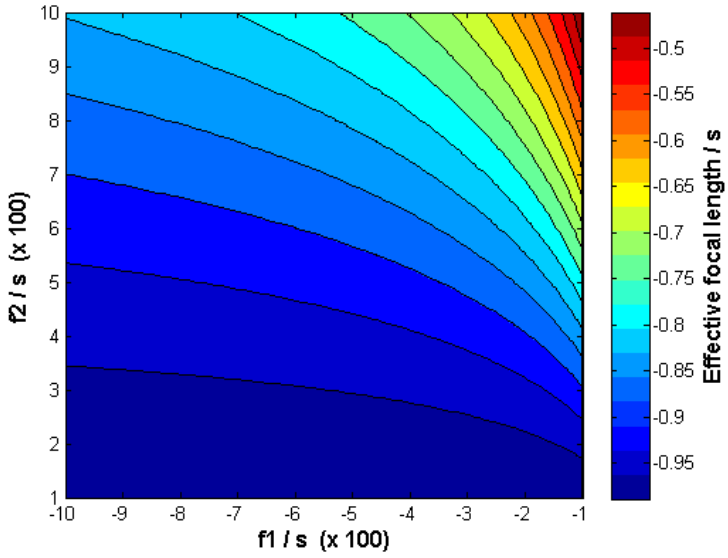

(b) Contour plot of the effective focal length, F_{eff}, of the PCE as a function of the focal lengths f_1 and f_2, normalized by the distance between the diverging lens and the sweet plane, s. [33]

Figure 3.4: Plot showing how choosing the working distance of the system, s, and the focal lengths of the lenses, f_1 and f_2, determines the focusing parameter, f_{PCE}.

The distance d can now be defined as

$$d = \frac{f_1 f_2 - s(f_1 - f_2)}{s + f_1}. \tag{3.13}$$

Using eq:d, M_{out} reduces to:

$$\begin{pmatrix} -1 & 0 \\ -\frac{2(sf_2+f_1^2+f_1f_2)}{f_2(s+f_1)^2} & -1. \end{pmatrix} \tag{3.14}$$

where $M_{out(2,1)}$ is the δ parameter of the PCE, described in Eq. (3.4). δ can thus be defined by:

$$\delta = -\frac{2(sf_2 + f_1^2 + f_1 f_2)}{f_2(s + f_1)^2}. \tag{3.15}$$

For further details of these calculations, see Section 3 in Appendix F. One very useful property of the PCE, from Eq. (3.13), is that the larger the working distance s, the smaller the distance between the lenses, d, becomes. This is extremely desirable for space applications, as it means the size of the device containing the PCE can be reduced for working distances larger than the current nEUCLID design.

Ray tracing diagrams were produced using MATLAB to investigate the properties of the PCE in both the focal (Fig. 3.5a) and afocal (Fig. 3.5b) configurations, i.e., an object at the sweet plane and an object at infinity. The parameters used were: $f_1 = -30\,\text{mm}$, $f_2 = 50\,\text{mm}$ and $s = 200\,\text{mm}$, giving $d = 23.9\,\text{mm}$ and $1/\delta = -107\,\text{mm}$.

In the focal configuration – Fig. 3.5a – the PCE acts as a CCE; inverted images of the object are formed at the sweet plane. However, the returning rays do not have angles that are equal and opposite of the input rays, as discussed in Section 3.3.3.

In Fig. 3.5b two parallel rays enter the PCE symmetrically about the optical axis. The returning rays converge to a virtual focus, $1/\delta$, behind the sweet plane, caused by the mismatch between input and output ray angles.

3.3.3 Visibility of the Interference Pattern

Using the PCE for tilt-immune interferometry requires further investigation into how δ affects the output displacement and angle. Consider a ray reflecting off the target mirror with angle, θ_m, at a distance, r_m from the optical axis. The ray enters the PCE system at angle, $2\theta_m$ and, using Eq. (3.5), the output angle (before being reflected out of the system by the target mirror) is

$$\theta_{out} = r_m\delta + 2\theta_m(z\delta - 1) \tag{3.16}$$

The ray deviation, having reflected off the target mirror on returning from the PCE, is

$$\Delta\theta = r_m\delta + 2\theta_m z\delta \tag{3.17}$$

Using the same method, but for the output ray displacement, the transverse displacement

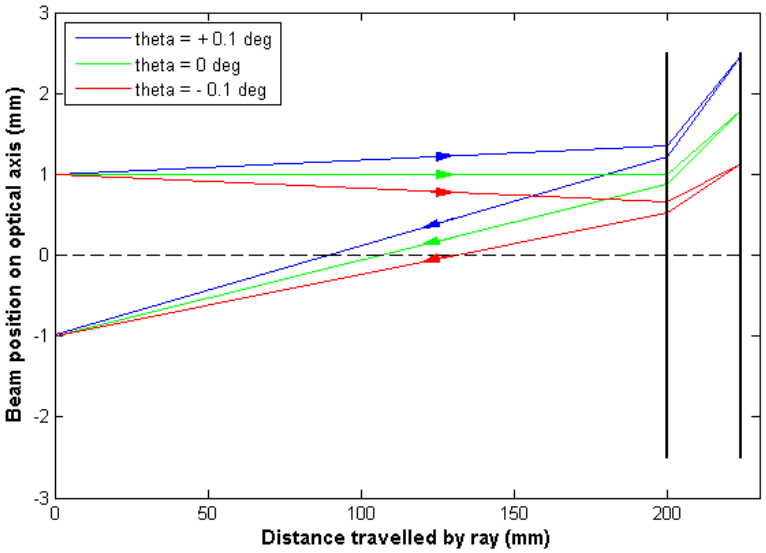

(a) Diagram showing passage of rays through the PCE to and from the sweet plane [33].

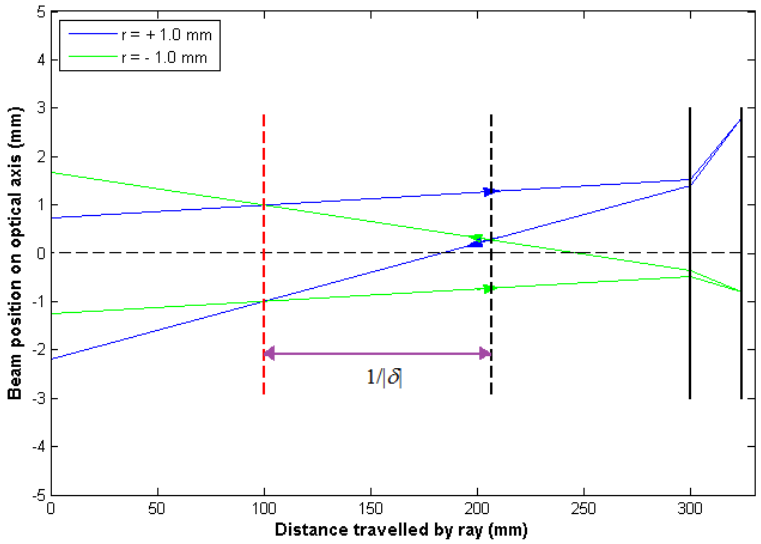

(b) Diagram showing passage of parallel rays through the PCE. The red dashed line represents the sweet plane; the black dashed line is the focus of the rays, at $z = 1/\delta$ [33].

Figure 3.5: For both ray diagrams the PCE parameters are $f_1 = -30\,\text{mm}$, $f_2 = 50\,\text{mm}$, $s = 200\,\text{mm}$, $d = 23.9\,\text{mm}$, and $1/\delta = -107\,\text{mm}$ [33].

of the returning ray is

$$\Delta d_t = r_m(z\delta - 1) - 4\theta_m z(1 - \frac{z\delta}{2}) \tag{3.18}$$

In the PCE, from Eq. (3.17), as the target mirror moves away from the sweet plane, the output beam becomes misaligned with the incoming beam. Eq. (3.18) shows that the displacement also changes, due to the terms being proportional to δ. The tilt and displacement of the returning target beam reduce the visibility of the interference pattern (as it no longer aligns perfectly with the reference beam), and this decreases further as z and θ_m increase.

The drop in visibility with z is also observed in the CCE, having set δ in Eq. (3.17) and Eq. (3.18) to zero. As a working example, compare nEUCLID with EUCLID. For both, $r_m = 0$, $\theta_m = 0.1°$, and $z = 10\,\text{mm}$, with nEUCLID having $\delta = -0.004\,\text{mm}^{-1}$. Using Eq. (3.17) and Eq. (3.18), it is shown that $\Delta\theta = 0°$ and $\Delta d_t = 0.070\,\text{mm}$ for EUCLID, and $\Delta\theta = 0.0080°$ and $\Delta d_t = 0.071\,\text{mm}$ for nEUCLID.

Thus, the tilt immunity of both the CCE and the PCE has a finite range of z values. This is explored for the PCE in Section 5.1.2; see [9] for further details of the visibility of EUCLID.

3.3.4 Optical Path Length

Using Eq. (3.5), the optical path length of rays passing through the PCE system can be calculated. Using the standard ABCD matrices for a space of distance, z, on either side of the PCE to mimic the target arm, the optical path length OPL through each system component from point x_1 to point x_2 was calculated using the Eikonal equation ([34, pp. 781]):

$$OPL(x_1, x_2) = L_0 + \frac{1}{2B}(Ax_1^2 - 2x_1x_2 + Dx_2^2) \tag{3.19}$$

where L_0 is the on-axis distance, and A, B, C, and D refer to the specific matrix term for each component.

The optical path for the PCE is calculated both with and without the z mirror displacement either side, to give the optical path difference measured by the interferometer when the target mirror is displaced by a distance, z. Using the same method as before, where a beam of angle $2\theta_m$ enters the system at a distance r_m from the optical axis, the optical path difference is

$$\begin{aligned} OPD_1(z, \theta_m, r_m) =& 2z\left(1 - 2\theta_m^2\right) - \frac{r_m^2}{\delta}2 + 2z\left(\frac{r_m^2\delta^2}{4} - 2r_m\theta_m\delta\right) \\ &+ 4z^2\left(\frac{\theta_m r_m\delta^2}{2} - \frac{3}{2}\theta_m^2\delta\right) + O(z^3) \end{aligned} \tag{3.20}$$

The first term in Eq. (3.20) is the optical path difference expected from a CCE (all other terms for a CCE are zero, as δ is zero).

Further optical path difference is introduced as the beam travels back to the point of interference with the reference beam. The beam travels a distance, D, giving an extra

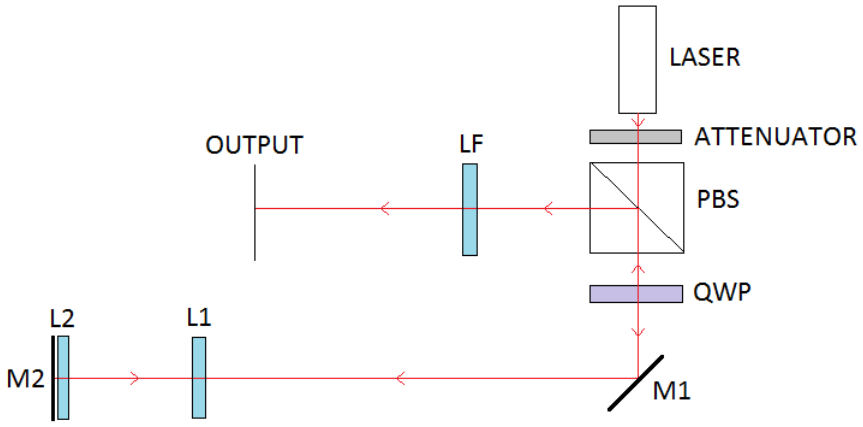

Figure 3.6: Initial design to confirm PCE properties using a HeNe laser source.

path difference of

$$OPD_2 = \frac{D}{2}(\Delta\theta)^2 \tag{3.21}$$

where $\Delta\theta$ is given by Eq. (3.17). With correct alignment r_m can be zero and remain so as the target mirror moves away from the sweet plane. Thus we can reduce Eq. (3.21) to consider only the terms relating to θ_m:

$$OPD_2 \approx \frac{D}{2}(\theta_m^2 z^2 \delta^2) \tag{3.22}$$

As discussed in [33], D is of the order of $1/\delta$, and only becomes significant when z is of the order of $1/\delta$. Due to fringe visibility limits restricting z, OPD_2 is mostly insignificant. To give a working example, nEUCLID has a δ value of $-0.004\,\mathrm{mm}^{-1}$. For D to become significant, z would have to be approximately 250 mm. However, for z greater than 120 mm (the working range of nEUCLID) the visibility becomes too low for a good Lissajous pattern, thus OPD_2 is not important.

3.3.5 Initial Design Testing

Before beginning to build the new interferometer with the PCE, the cat's eye design was tested to confirm it had the properties described in Eq. (3.3), and a working distance of more than 60 mm.

The testing began using a 633 nm HeNe laser and two standard plano-concave and plano-convex lenses (L1 and L2) from the optical laboratory, as shown in Fig. 3.6. Two plane aluminium mirrors were used, one behind the lenses to reflect light out of the PCE (M2), and one to reflect the laser beam into the PCE (M1). A small, tight fringe pattern approximately 2 mm in diameter was observed at the output, which did not move when the target mirror was tilted by approximately $\pm 0.5°$.

The next step was to test the PCE over a distance of several hundred millimetres. This was achieved by bouncing the HeNe beam off several mirrors laid out across the optical bench as shown in Fig. 3.7 before entering the PCE (L1 and L2), to mimic a long target

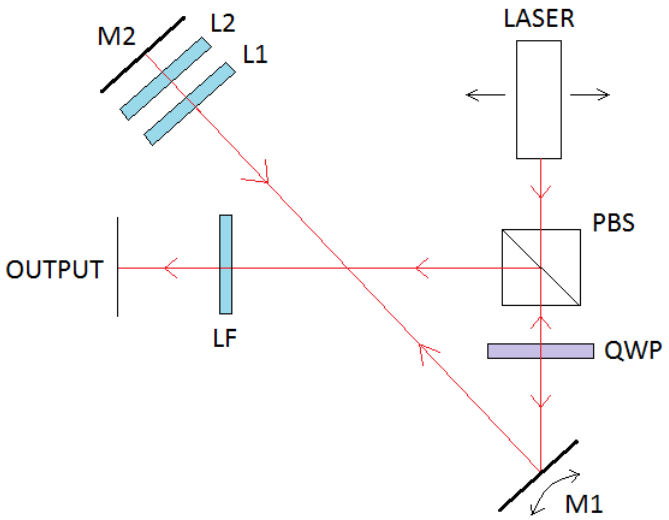

Figure 3.7: Initial interferometer design to confirm PCE properties using a HeNe laser source. Total working distance is 930 mm.

arm. Once again, tilting the target mirror (M1) by approximately $\pm 0.5°$ did not cause the fringe pattern to move, confirming tilt immunity of the PCE. The laser was mounted on a micrometer drive and translated across the optics, with a focusing lens (LF) in front of the detector to ensure the PCE was also immune to translational beam displacement. The final working distance tested using this method was 930 mm.

The design was also confirmed using a VCSEL, the same source used in EUCLID, with the same methods described above but laid out as shown in Fig. 3.8. The HeNe laser was replaced with the VCSEL and an aspheric lens, to collimate the VCSEL output. The working distance of this design was 1.40 m.

Whilst the VCSEL was able to produce a tilt immune fringe pattern in the PCE, it was decided that a different source should be used for the new interferometer design, as the target arm length would be limited by the coherence length of the VCSEL (see Section 4.4 for more detail). The position of the PCE was moved from the target arm into the shorter arm, to allow a long clear path for the position of future targets.

3.4 The Meniscus Lens

As discussed in Section 3.3.1 the PCE has a focus, after which the target beam diverges. This divergence causes the output target beam width and the radii of curvature to differ from that of the reference beam. When the beams recombine and interfere the best visibility is no longer achievable. To ensure a closer match of beam width and radii of curvature, the beam passage inside nEUCLID was modelled to produce the maximum and minimum visibility of interference pattern ($\phi = 0$ or π). A lens was placed in the reference arm to match the radius of curvature of the two beams (see Appendix E for details). A meniscus lens was chosen because it was readily available for the required focal length.

The radius of curvature at the photodiodes should be $1/\delta$ (-238 mm) plus the additional

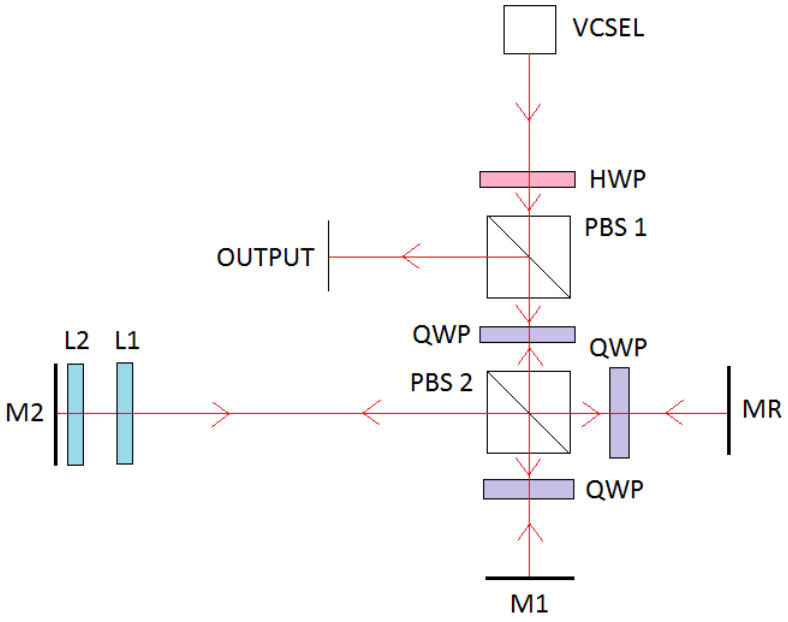

Figure 3.8: Secondary interferometer design to confirm PCE properties using a VCSEL laser source. Total working distance is 1.40 m.

distance the beam travels to the PDs, to good approximation. The radius of curvature of the modelled target beam, R_{cT}, is 1118.9 mm. Adding on the approximate distance from the the target beam focal point to the PDs gives a value of 1014 mm. The similarity of these results shows that the meniscus lens method is in line with the geometrical optics method, and that the model used to predict the interference patterns gives sensible results, i.e. the beam is diverging after the focal point in the PCE.

The predicted output interference pattern with and without the meniscus lens, produced using the code in Appendix E, can be seen in Fig. 3.9a and Fig. 3.9b. A focusing lens was used on the output of nEUCLID to produce these patterns as the pattern was too large for the imaging area of the charge-coupled device (CCD) camera without it; 16.0 mm beam diameter compared to an active area of the CCD of 4.9 mm^2.

These fringe patterns are compared with those taken with nEUCLID in the laboratory in Section 5.1.1, and match the data well.

3.5 Comparison of Cat's Eyes

To optimise the PCE, the cat's eye system was modelled in sequential Zemax, an optical design program. Figure 3.10 shows the PCE in Zemax, whilst Fig. 3.11 shows the CCE for comparison. Two configurations were used: afocal, where the rays enter the system from infinity, and focal, where the rays enter at the sweet plane. The PCE was created from standard lenses from the in-built lens catalogue, and was modelled as an unfolded system. A "perfect" lens was added to the system to eliminate the curvature of the beam. Initial approximate values for the four PCE parameters (s, d, f_1, and f_2) were calculated, using the results described in Section 3.3.2.

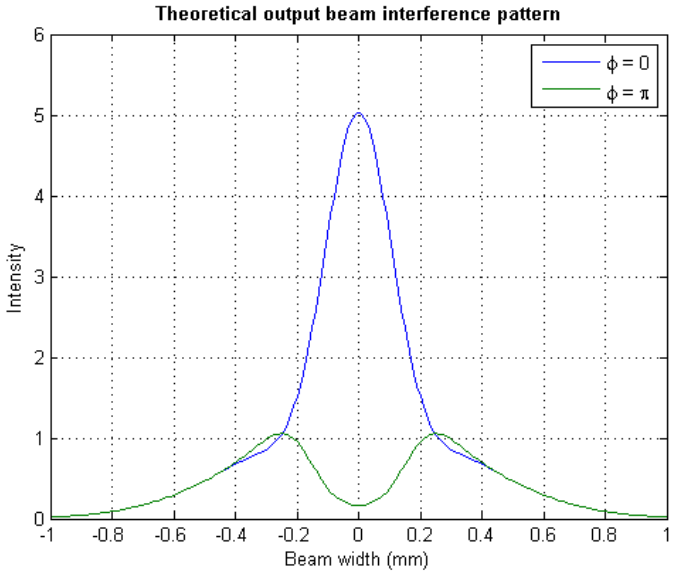

(a) Predicted interference pattern from nEUCLID with the meniscus lens.

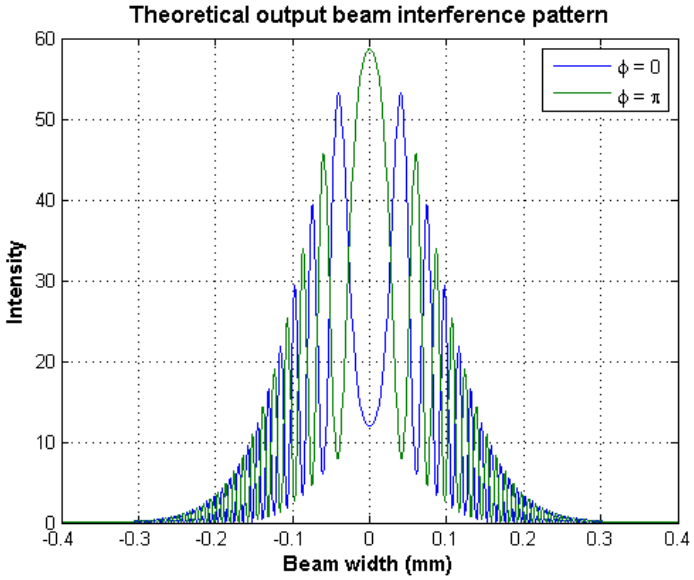

(b) Predicted interference pattern from nEUCLID *without* the meniscus lens. Note the smaller x axis, to allow closer inspection of beam width values due to a tight pattern.

Figure 3.9: The predicted output interference pattern of nEUCLID, with (*a*) and without (*b*) the meniscus lens. ϕ indicates the maximum and minimum value for the visibility in each case [33].

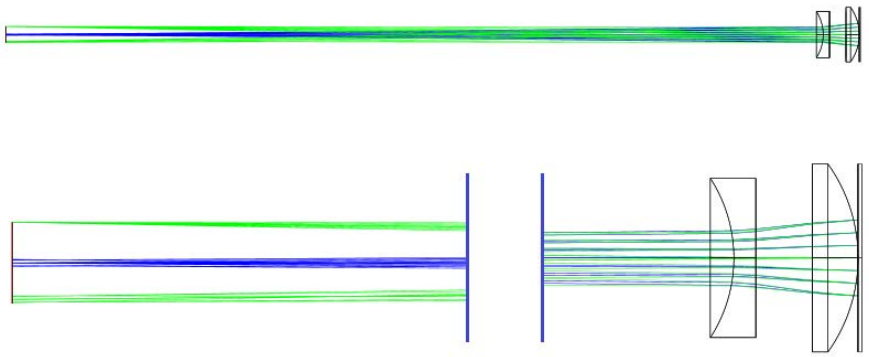

Figure 3.10: The PCE as modelled in the focal mode in sequential Zemax, with the lower image showing a zoomed-in version of the lens configuration ($r_{in} = 4.5\,\text{mm}$, $s = 450\,\text{mm}$, $d = 9.0\,\text{mm}$). The blue rays represent an on-axis beam; the green rays represent a beam off-axis by 1 mm, showing the system working as a cat's eye.

The optimisation routine begins with the afocal mode: rays enter the PCE at $\pm 0.5°$, to mimic the range of tilt of a target. The rays reflect off a plane mirror and out of the PCE to an image plane; the nominal sweet plane. The distances f_1 and d were adjusted around the nominal values to minimise the outgoing spherical wavefront aberrations at the sweet plane.

Once this was achieved, the PCE was optimised in the focal configuration. Rays enter the PCE at $\pm 8\,\text{mm}$, to mimic the diameter of the target beam. They reflect off a plane mirror and out of the PCE, this time focusing at the sweet plane. The position of the sweet plane was found by adjusting s to optimise the optical path difference between the extreme rays.

Whilst the CCE contains no δ term and thus is a "perfect" cat's eye, the PCE has substantially lower wavefront distortion at large s distances. Three different CCE and PCE set-ups were modelled in Zemax using simple lenses, to monitor the wavefront error of the output beam as the target mirror was tilted. The working distance, s, for each pair of systems was 200 mm, 1000 mm and 10 000 mm, and the resulting R for each system was calculated, displayed in Fig. 3.12.

As is clear in Fig. 3.12, the CCE wavefront error increases sharply at larger s values (i.e. larger R systems; $R = s/d$) with increased input angle. In contrast to this, the wavefront error for the PCE systems decreases at larger s values/for large R systems.

This analysis using simple lenses shows the advantage of the PCE because large focal ratios can be used for both lenses. Such lenses cannot be used to realise a CCE with a large value of R. A simple example given in [33] demonstrates this point: if the convex lens in a CCE is assumed to have a unit focal ratio, in order to achieve $R = 11$ the focal ratio of the negative lens has to be 0.1. Suitable optical elements with this property do not exist to the knowledge of this author.

The PCE in nEUCLID has an s value of 660 mm and a d value of 73.95 mm, with a wavefront distortion on axis at the sweet plane of 0.0031 waves. For further details of the lens systems please see appendix F.

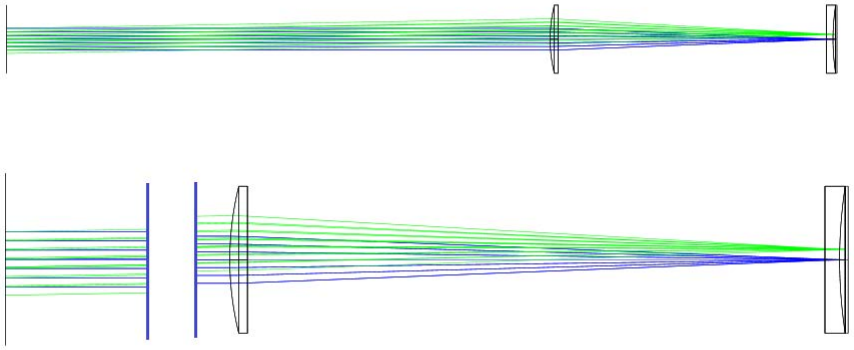

Figure 3.11: The CCE as modelled in the focal mode in sequential Zemax, with the lower image showing a zoomed-in version of the lens configuration ($r_{in} = 1.0\,\text{mm}$, $s = 200\,\text{mm}$, $d = 98.5\,\text{mm}$). The blue rays represent an on-axis beam; the green rays represent a beam off-axis by 1 mm, showing the system working as a cat's eye.

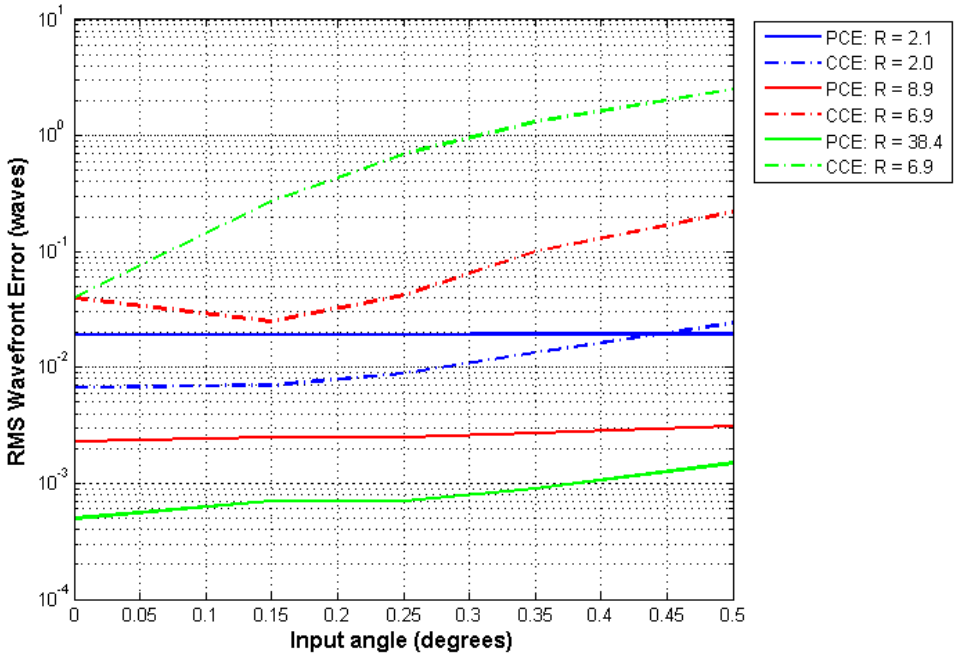

Figure 3.12: Plot of the increasing wavefront error for the PCE and CCE over a range of input angles. Blue, $s = 200\,\text{mm}$; red, $s = 1000\,\text{mm}$; green, $s = 10\,000\,\text{mm}$ [33].

3.6 Summary

A new cat's eye has been developed – the PCE – which allows the interferometer to have highly unequal arm lengths. A cat's eye is a retroreflector – a device that reflects rays of light back to their source with minimum scattering. The basic function of a cat's eye is to reflect an incoming beam such that it is returned parallel to its incoming path, irrespective of the angle between the incoming beam and the optic axis of the cat's eye. Whilst not being a "perfect" cat's eye, the PCE is highly effective. The PCE contains a δ parameter in its matrix, which acts as a negative focusing element. If treated accordingly this does not hinder the usage of the PCE; it is either too small a value to cause an impact on measurements, or it can be negated by adding a meniscus lens to the reference arm of the interferometer. The interference pattern produced when using a reference arm meniscus lens are modelled using MATLAB and shown in Fig. 3.9.

Initial designs undertaken to prove the properties of the PCE are described, as is the mathematical structure of the PCE and the δ parameter. Choosing the working distance, s, of the PCE defines the working distance of the interferometer, and the separation of the cat's eye lenses, d. An additional optical path length occurs the further from the sweet plane of the PCE the target is moved, as shown in Eq. (3.20). The PCE has another interesting property: the larger the working distance, the lower the wavefront error of the system, compared to a CCE. This is extremely advantageous for use in long-distance applications.

Chapter 4

nEUCLID

Figure 4.1 shows the complete nEUCLID in the laboratory showing the full target arm, the optics (covered by a black perspex case), the electronics unit, and a laptop to run the data acquisition software.

4.1 Optical Configuration

Figure 4.2 shows a sketch of the nEUCLID optical set-up. The beam passage through the set-up will now be described.

(Note: In the following explanation ρ polarisation and ς polarisation are the electric field components of the beam that are parallel (ρ) and perpendicular (ς) to the plane of incidence of the incoming and outgoing beams. The polarisation state is defined by the surface the polarisation encounters; the states do not remain constant through the optical system.)

A 1550 nm DFB pig-tailed laser is taken from the electronics box to a polarisation-maintaining fibre via a wide-key FC/APC to FC/APC connector. The beam passes through the fibre and into a collimator through the FC/APC connector. The beam passes out of the collimator and through a sheet polariser (P1) and PBS 0. The beam passes through PBS 1 and a NPBS. A HWP, orientated at 22.5° to ensure neither polarisation is aligned with either waveplate axis, rotates the plane of polarisation by 45°, causing the beam to separate into each polarisation upon passing through PBS 2. The ς polarisation travels down the target arm, and ρ polarisation down the reference arm.

Within the target arm, the ς beam passes through QWP 1, travels to the target mirror (MT), and back again, back through QWP 1. The double pass through the quarter wave plate causes the target beam to pass through PBS 2, and into the cat's eye arm. This consists of the two cat's eye lenses – a plano-concave lens (L2) and a plano-convex lens (L3) – and a mirror. The beam passes through the two lenses, reflects off the cat's eye mirror (MC), and passes back through the lenses, and back down the target arm. Reflecting off the target mirror a second time, the beam travels through QWP 1 again (the fourth time), causing the beam to now reflect through PBS 2.

Meanwhile, in the 21 mm reference arm, the ρ beam has passed through a second sheet

Figure 4.1: Photograph of nEUCLID showing the full target arm and covered optics (the black box), and the electronics box, with a laptop to run the software and for scale.

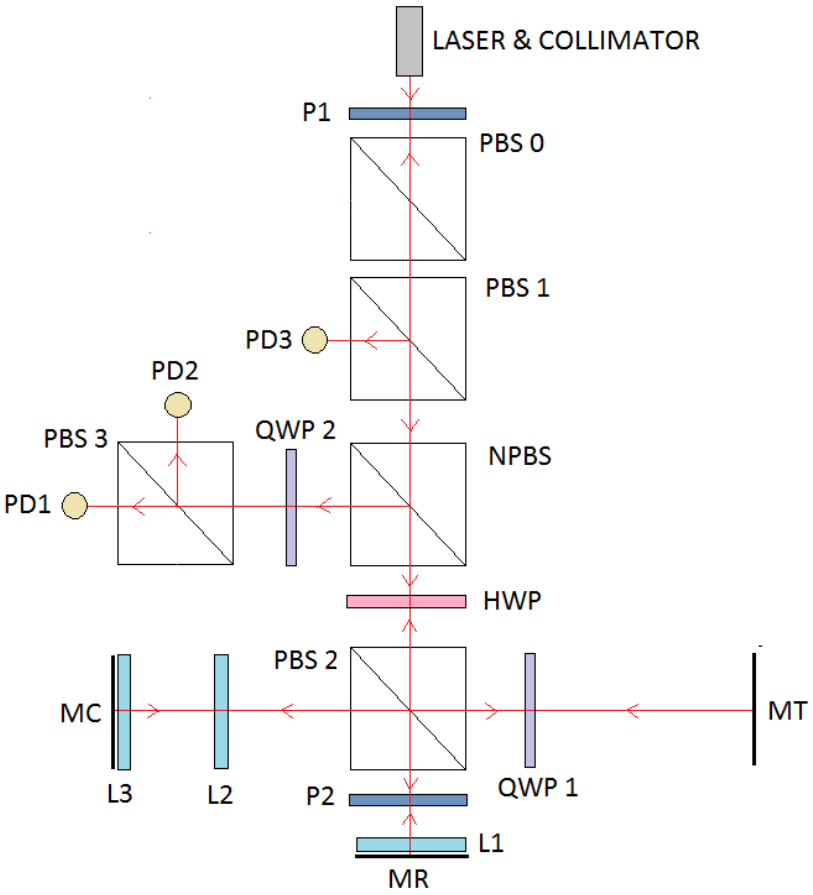

Figure 4.2: Schematic diagram of nEUCLID (target arm not to scale).

polariser (P2). After this the reference beam passes through the meniscus lens (L1) and reflects off the reference arm mirror (MR). It passes back through the meniscus lens, back through the polariser, and travels back through PBS 2, recombining with the target beam.

Both beams, now recombined, pass back through the HWP and NPBS. This splits the beam into two beams of equal intensity. One half of the beam travels through QWP 2 to PBS 3. Here the beam is separated again into the two polarisation components – PD1 (cosine) and PD2 (minus cosine). The other half of the NPBS-split beam travels onwards, to be separated into polarisation components by PBS 1. The ς polarisation beam travels to PD3 (sine), whilst the ρ polarisation continues on towards the laser. All the optics are coated with a 1550 nm anti-reflection (AR) coating, and are mounted on a 1 m-long aluminium rail.

4.2 Additions to the Design

During implementation small problems developed during the design process that needed solving. This section explains the need for certain components in the nEUCLID design described in Section 4.1, and how they improve the performance of nEUCLID.

The plane of polarisation of the laser is accurately aligned with the laser fibre in the electronics box as it is set by the manufacturer. The bulkhead connector (the FC/APC) connects the laser fibre with the patchcord fibre that connects the optics to the electronics. However, the phase of the polarisation is not stable unless the two fibres are aligned by $<1°$. Ambient heating/cooling of the fibre changes the refractive index of the fibre, allowing the different polarisation states through the fibre. This causes phase fluctuations which add to the overall noise of the interferometer. PBS 0 aids PBS 1 in excluding any polarisation deviation because of the low optical quality of PBS 1. This effect was tested by holding the laser fibre in my hand, to heat a section of the fibre by a few degrees. This was done away from the collimator, to ensure no stress was placed on the fibre connection, which would also induce apparent phase change in the system.

Before the beam travels through the polariser, it travels directly into a collimator. This is to collimate the beam upon entry to the interferometer optics, to limit the divergence of the beam as it travels through the system and down the long target arm. However, the target beam does still diverge over this distance due to the PCE, thus a second sheet polariser (P2) is placed in the reference arm to match the reference beam intensity to that of the target beam for a better visibility of interference pattern.

A circulator inside the fibre prevents the beam from re-entering the laser. A circulator is a device that guides the passage of a beam using "ports" that allow light to pass in/out [35]. A beam passes from one port (say Port 1) and out of a second port (Port 2), out of the fibre. However, on return from the optical system, the beam passes in through Port 2 and now out of Port 3, as shown in Fig. 4.3. Port 3 is directed away from the laser, restricting potential optical feedback by 30 dB [36, p.703].

A sheet polariser (P1) was placed at the input of the laser to the optics to further reduce the optical feedback into the laser. This extra reduction was also found to be necessary with EUCLID [9, p.99].

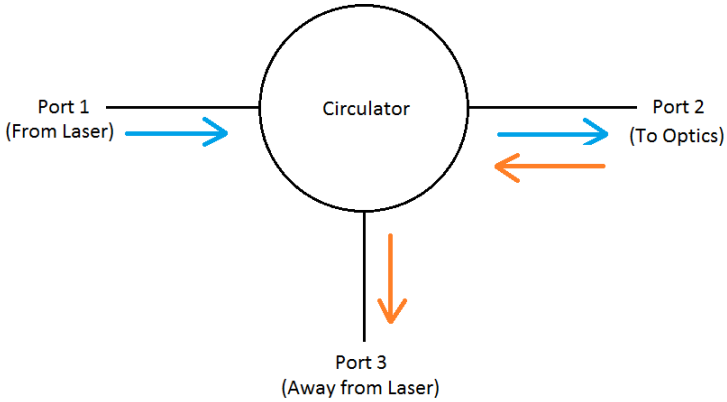

Figure 4.3: Diagram showing how a circulator affects the beam passage in an optical system; the blue arrow is entering the optical system, the orange arrow is leaving the optical system [35].

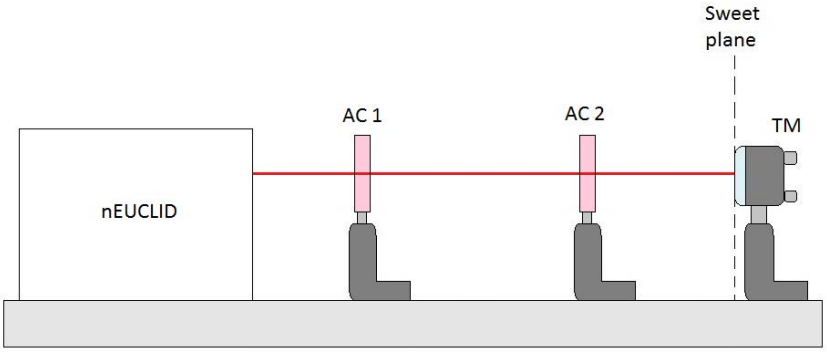

Figure 4.4: Diagram showing the two fluorescent alignment pinhole cards (AC) in position along the target arm during the alignment process.

4.3 Aligning nEUCLID

The DFB laser in nEUCLID is invisible to the naked eye. This makes it less convenient to align when setting up the interferometer. The following method describes the alignment process of nEUCLID.

A HeNe laser was passed through the fibre, into the collimator, to align the major optics (beam splitters, lenses, etc), as this beam is visible. Once the optical components have been aligned so that the HeNe beam passes through the centre of each, two fluorescent alignment cards with pinholes are positioned along the target arm, as shown in Fig. 4.4. This ensures the beam is parallel with the aluminium rail, and thus the set-up. Once the beam passes through these pinholes and back the HeNe laser is swapped to the DFB. The alignment cards will show any misalignment of the DFB beam.

Once the optics and beam are correctly aligned, an infra-red (IR) CCD camera is positioned at one of the outputs where PD1 would be placed. A plano-convex lens of focal length 80 mm is used to focus the output beam onto the CCD. The camera observes the interference

pattern to confirm the target and reference mirrors are aligned for best visibility (a circular interference pattern similar to Fig. 2.6a).

The CCD camera is removed and the three photodiodes are replaced. An oscilloscope is used to check the signals on each photodiode, to ensure each is positioned in the centre of the interference pattern and thus see the maximum visibility. The oscilloscope is also used to check the size and shape of the Lissajous pattern once the photodiodes are positioned. Any final minor adjustments to the interference pattern can be made with the reference mirror mount. The Lissajous pattern is fairly stable; the air current in the lab caused it to slowly trace out a circle as the air crossed the target arm beam path unless the arm was covered.

4.4 Laser Selection

The initial prototypes of nEUCLID, designed to test the basic theory of operation, used a stabilised HeNe as the source. Having determined the PCE was viable in such an interferometer, small-package laser sources were investigated as the HeNe laser is large ($\approx$ 30 cm) and not easily space-qualified. EUCLID contains a VCSEL which, whilst relatively inexpensive, has a coherence length of 2 m. Because of the desired working distance of 1 m for nEUCLID a coherence length of at least 5 m was necessary. For this reason a DFB laser was chosen; it is a commercially well-used source, due to its very low failure rate (0.1 nm wavelength shift in 20 years [37]) and options for long coherence lengths. The laser we used is not space-qualified, but could easily be replaced with a laser that is for future versions of nEUCLID.

The DFB laser used in nEUCLID has a spectral bandwidth of 1 MHz [38], thus a coherence length, L_c, of 200 m is given using

$$L_c = c\tau_\nu, \tag{4.1}$$

where τ_ν is the coherence time, defined in Eq. (4.2) [13, p.61],

$$\tau_\nu = \sqrt{\frac{2\ln 2}{\pi}}\frac{1}{\Delta\nu}, \tag{4.2}$$

where $\Delta\nu$ is the spectral bandwidth, determined by the wavelength of the laser, λ: $\Delta\nu = \nu\Delta\lambda/\lambda$.

Using an IR laser made it difficult to align nEUCLID, and thus more complicated to build than if a visible laser had been used. However, IR optical components are readily available and, as previously mentioned, certain IR lasers have coherence lengths of up to tens of kilometres.

4.5 Description of Apparatus

Besides the main optical set-up, nEUCLID has several other design components. The collimator is mounted on a micrometer drive, to allow it to be moved transversely to the optical set-up to align the laser beam through the optics. The entire interferometer,

Figure 4.5: Photograph of the nEUCLID target mirror on a DC motor stage, mounted on a micrometer drive and the aluminium rail.

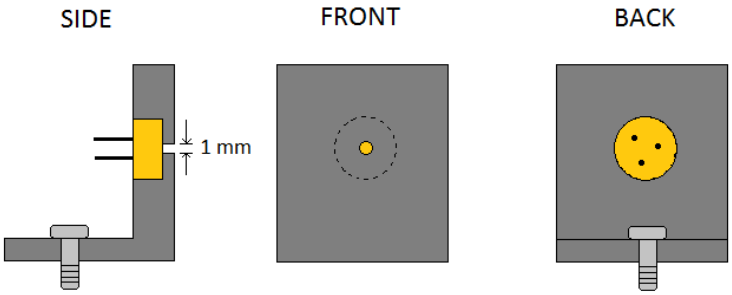

Figure 4.6: Diagram of the photodiode mounts used in nEUCLID.

including the target mirror, is mounted on aluminium rail sliders on the 1 m aluminium rail. This is to allow accurate alignment of the target mirror and easy transportation of the device.

As shown in Fig. 4.5, the target mirror is mounted on a micrometer drive (on an aluminium slider), which allows the target mirror to be moved transversely across the beam path, again to aid in aligning the beam. The mirror is mounted on a direct current (DC) motorised stage, which controls the tilt angle of the mirror using one motor per axis. The minimum slew rate of the target mirror is $50\,\mu\mathrm{m\,s^{-1}}$ [39]; the angular speed used to take data from nEUCLID is $0.1\,^{\circ}\,\mathrm{s^{-1}}$. The full angular range of the motor is $\pm 4°$, however, this was limited to $\pm 0.6°$ due to the size of the optics and target arm length.

An optical lever was used to confirm the angle the target mirror moved by; a HeNe laser beam was reflected off the target mirror and onto the laboratory wall, where a calibrated scale was placed. Each movement of the target mirror was confirmed using this scale, to ensure to correct tilt angle.

The photodiodes were fitted into mounts of my own design, shown in Fig. 4.6. They were changed from aluminium to black acetal to stop reflections into the sensor area, and to insulate the photodiodes from the aluminium mounting post and breadboard. A pinhole of diameter 1 mm in the front of the mount ensured the interference pattern was centred

on the active area of the PD.

Figure 4.7 is a photograph of the nEUCLID optics in the lab. (Note: the target arm is too long to fit into this photo).

The optics of nEUCLID, shown in Fig. 4.7, are enclosed in a black perspex box which screws into perspex posts mounted on the breadboard. This protects the interferometer from dust and air currents, and ensures secure travel of the equipment. The current dimensions of the interferometer (not including the target arm) are 280 mm × 160 mm × 110 mm.

The mass of the optics (including the aluminium breadboard) is approximately 2.0 kg. This would be reduced if nEUCLID was commercialised; the mass is large as all the components are standard, off-the-shelf components.

The electronics box containing the laser and the software controlling the data acquisition are extremely similar to that used for EUCLID, described in Section D.2 and Section D.3. However, instead of a laser diode (with associated electronics) there is a DFB laser butterfly package, with a thermoelectric cooler to regulate the laser temperature. The software package is the same, except it is calibrated for a 1550 nm signal. The data acquisition for this project was 400 Hz (a sampling rate of 1 MHz and a decimation rate of 2500).

The power of the laser is 7 mW [40]. The electronics box power is 2 W, from a 9 V source, and has dimensions of 190 mm × 60 mm × 170 mm [18].

See Appendix C for details on the materials and components used in nEUCLID.

4.6 Nomenclature

The working distance, s, is the distance from the sweet plane (the optimum working distance, defined in Section 3.2) to the interferometer body. The working range, w_r, is the distance the target mirror can move away from the sweet plane to reduce the observed fringe visibility by 50%. These distances are shown in Fig. 4.8.

4.7 Summary

This chapter described the optical configuration of nEUCLID, with a schematic diagram and a photograph to aid in the understanding of the beam passage. Several design additions were made once the interferometer was built, such as a polariser in the reference arm to match the target beam intensity, and an extra polarising beam splitter to cut out polarisation deviations from the fibre. The alignment method for nEUCLID was explained; the complexity is due to aligning an (invisible) IR beam. An optical lever was used to confirm the tilt of the target mirror, due to the low repeatability of the mirror motors. A DFBlaser was selected due to its long coherence length, and because its compatibility with the space industry. A description of the apparatus was included, explaining the method of mounting the photodiodes, why the system is mounted on an aluminium rail nEUCLID, and the electronics box used to process the data from nEUCLID. Further details of the materials and components used can be found in Appendix C.

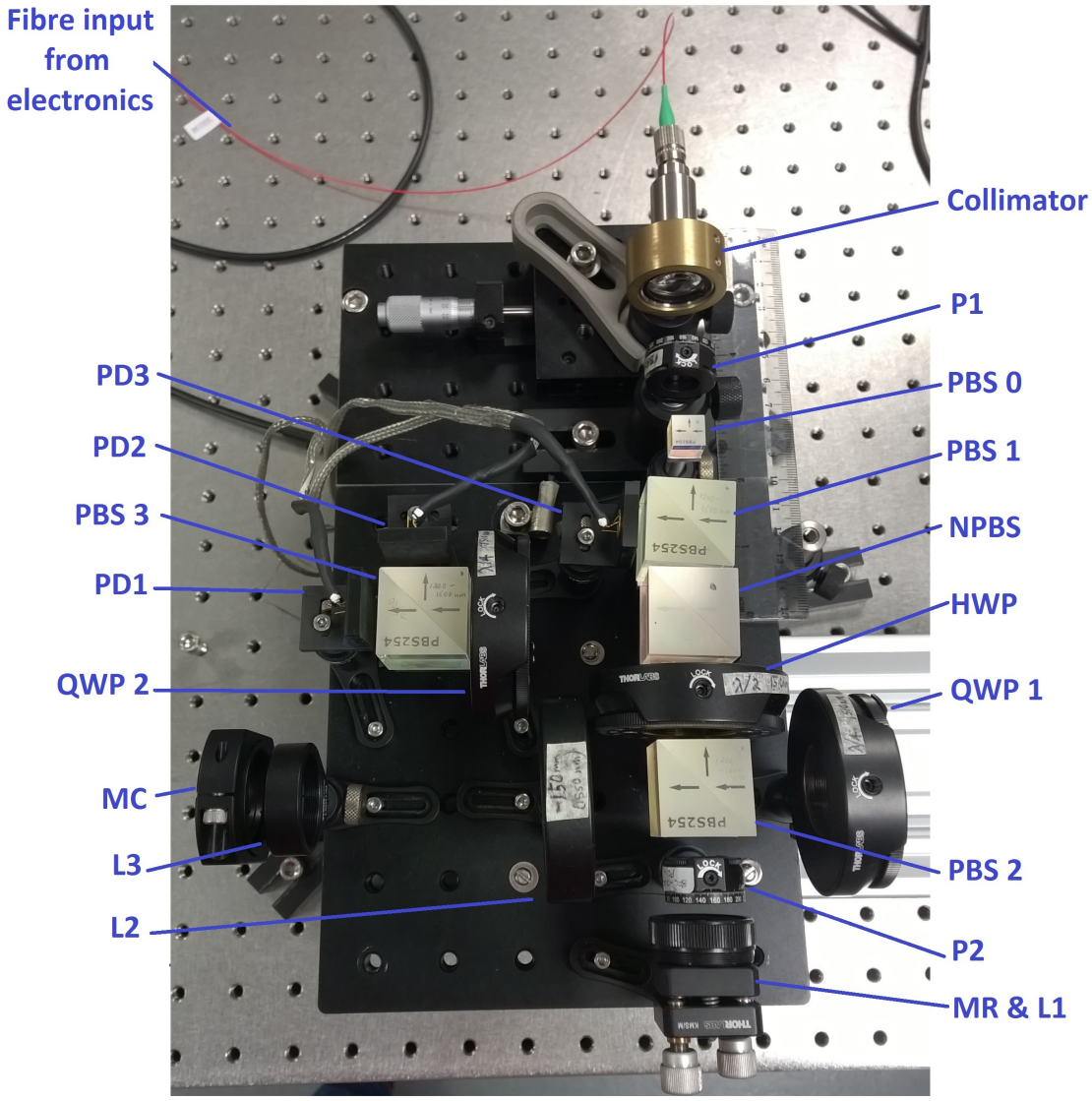

Figure 4.7: Photograph of nEUCLID optics in the laboratory; target arm not shown. Labels match those in Fig. 4.2.

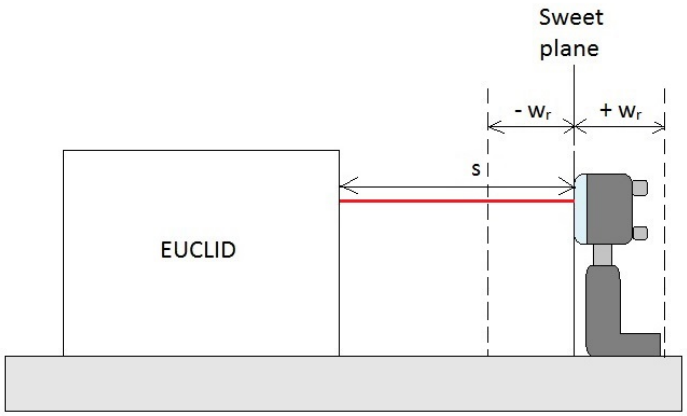

Figure 4.8: Schematic diagram of the working distance and working range of EUCLID. The working distance, s, is the distance from the interferometer body to the sweet plane; the working range, w_r, is the maximum distance away from the sweet plane where 50% fringe visibility is possible.

Chapter 5

RESULTS

This chapter discusses the data taken with nEUCLID. The fringe patterns observed with the meniscus lens are shown, as is an example of the tilt immunity of nEUCLID at the sweet plane. This result is compared with the expected displacement for tilting the target mirror were the PCE not there. The visibility of the pattern at and beyond the sweet plane is given, showing how the visibility and amount of tilt immunity drops when the target mirror is moved away from the sweet plane.

Whilst taking data with the CCD camera a single-pass interference pattern was observed (i.e., a beam from the target mirror that did not pass through the cat's eye). It is presumed this is due to low-quality polarising optics, and its origin is investigated in this chapter.

The focusing effect of the PCE means there is an extra phase difference across the photodiodes as the target mirror is tilted, and the target beam moves. Matching the Lissajous patterns with a computational model investigated the displacement of the target beam across the photodiodes, and calculations are given to remove the focusing effect of the PCE, thus the extra phase difference.

Finally, the sensitivity of nEUCLID is shown in an amplitude spectral density (ASD) for 10^{-2} Hz to 10^{2} Hz. The full time series plot of the noise over a 15 h period is also given. The values for the major noise sources in the system are calculated.

5.1 Fringe Pattern Predictions

The predicted fringe patterns discussed in Section 3.4 and shown in Fig. 3.9, created by adding a meniscus lens to the reference arm, are shown here with the laboratory data overlaid. The data were taken using a lens at one of the photodiode positions, which focused the output beam onto an IR CCD camera.

5.1.1 Fringe Patterns with the Meniscus Lens

Using the output interference pattern as a guide, a commercially-available concave meniscus lens was chosen. It has a focal length of -2013 mm, and is made of B270 glass. The

meniscus lens was placed in the reference arm, against the reference mirror, and the interference pattern observed. Figure 5.1a and Fig. 5.1b show the laboratory results with and without the meniscus lens in the reference arm. The photodiodes are masked and thus only see 1 mm diameter of the interference pattern.

Fig. 5.1 shows the observed data overlain on the model described in Section 3.4. The centre of the observed interference pattern and its vertical scale were fitted to the modelled pattern. A DC offset corresponding to background intensity was also removed from the observed data. The right-hand side of the pattern fits the model well, whilst the left-hand side is subject to optical distortions.

This proves the meniscus lens matches the target beam to the reference beam well enough that the interference patterns of nEUCLID are capable of being used to take displacement measurements.

5.1.2 Tilt Immunity in a Fringe Pattern

Once the interference patterns had been confirmed to match the model (Section 5.1.1), the tilt immunity of nEUCLID at the sweet plane was proven. The CCD camera remained at the interferometer output, and the reference arm was blocked; only the target beam was necessary for this test. The target mirror was tilted at the sweet plane from 0° to 0.1°. As can be seen in Fig. 5.2 the two target beam profiles remain in the same position, indicating that the system is tilt-immune. The modelled target beam for the set-up is also displayed, to ensure the system is still understood.

For contrast, if the PCE was removed from the interferometer (so the system was no longer tilt immune) and the target mirror was tilted at the sweet plane by 0.1° as in Fig. 5.2, the beam on the photodiodes would move by 3.46 mm.

5.2 Visibility of nEUCLID

Figure 5.3 shows the amount of target mirror tilt possible at each z distance from the sweet plane. Following the convention defined by EUCLID, the working range is the maximum distance the measurement target can move away from the sweet plane and still achieve a Lissajous pattern of 50% of the visibility at the sweet plane. The visibility, as discussed in Section 2.2.4, is defined by Eq. (2.30). The value of 50% ensures that the Lissajous pattern is still large enough to be able to be used to calculate a correct phase value. However, it is an arbitrary definition; in practice both EUCLID and nEUCLID can work at larger tilt ranges, as shown in Fig. 5.3 for nEUCLID and [9] for EUCLID. The minimum visibility is defined by whether the Lissajous pattern is distinct enough for the phase angle to be resolved. Fig. 5.3, therefore, demonstrates that nEUCLID could in principle work up to tilt angles of ±0.5°.

As the target mirror moves away from the sweet plane the visibility decreases until 120 mm, where the Lissajous pattern is 50% of its original visibility at 0° tilt. This defines the working range of nEUCLID to be ±120 mm. Between 0 mm to 120 mm the tilt range of the target mirror for 50% visibility is ±0.35°. At 120 mm for 50% visibility the tilt range

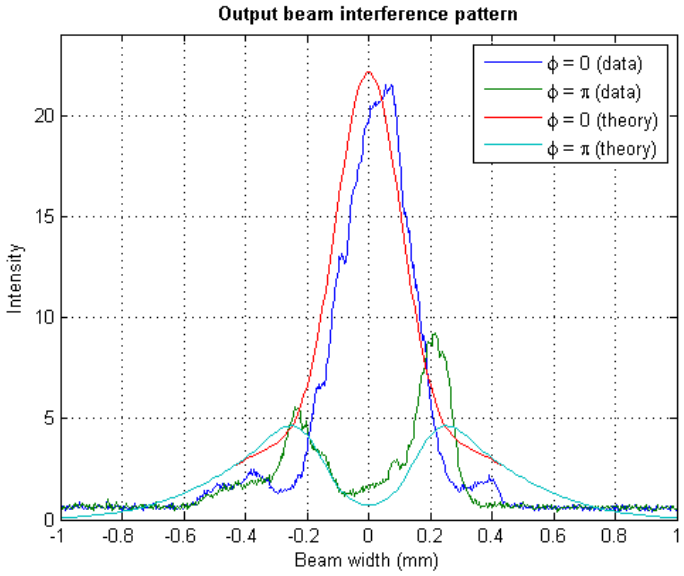

(a) The measured interference pattern from nEUCLID with the meniscus lens.

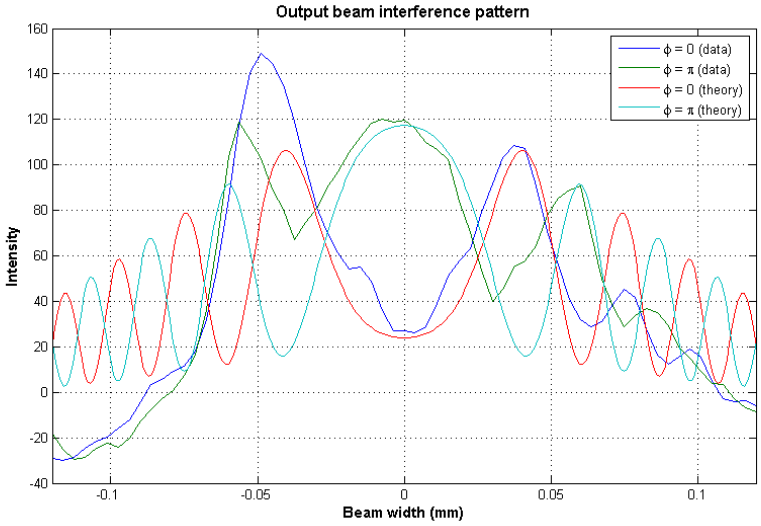

(b) The measured interference pattern data from nEUCLID *without* meniscus lens. The pattern has been magnified slightly to allow closer inspection of how well the model matches the data (i.e., the beam width is now $-0.12\,\text{mm}$ to $0.12\,\text{mm}$, compared with $-1.0\,\text{mm}$ to $1.0\,\text{mm}$ in Fig. 3.9).

Figure 5.1: The measured interference pattern of nEUCLID, with (*a*) and without (*b*) the meniscus lens. In both figures the modelled data has been overlaid for comparison. $\phi = 0$ or π indicates the maximum/minimum visibility.

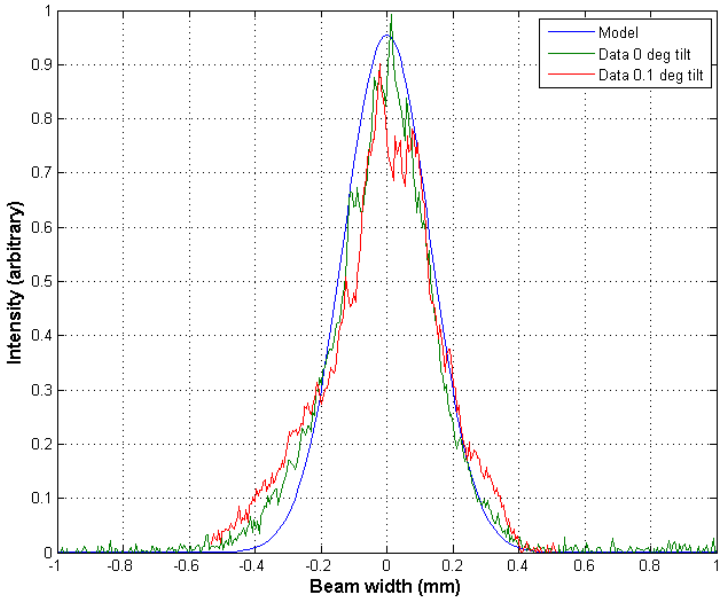

Figure 5.2: The output target beam of nEUCLID for 0° and 0.1° target mirror tilt at the sweet plane, with the modelled target beam overlaid for comparison [33].

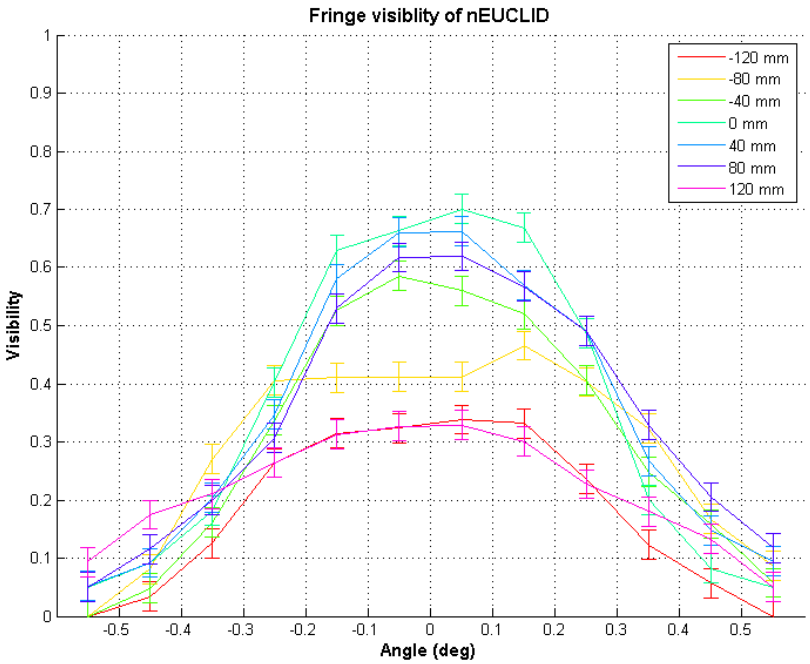

Figure 5.3: Plot of the visibility of nEUCLID for set z distances away from the sweet plane, $z = 0$.

decreases to ±0.15°. However, as Fig. 5.3 demonstrates, nEUCLID continues to work beyond the tilt range of ±0.15°, thus a tilt range of ±0.35° for the full working range is reasonable.

This can be compared with a non-tilt-immune interferometer. For non-negligible tilt angles the visibility is zero as there is no interference pattern. The visibility drops off from its maximum at 0° as the two beams clear each other. For example, using the beam sizes in this system (16 mm for the target beam and 8 mm for the reference beam), at the sweet plane a tilt angle of at most ±0.34° would be achievable, estimating 12 mm of clearance between the two beams.

5.3 Single-Pass Interference Pattern

When taking CCD images with nEUCLID a bright secondary interference pattern is visible in the data, shown in Fig. 5.5. With perfect optics the target arm QWP will ensure the entire target beam travels straight through the PCE, having reflected off the target mirror. However, there is an interference pattern caused by a stray beam from the target mirror that has *not* passed through the PCE. Fig. 5.4 shows the passage of this "single-pass beam" through nEUCLID.

The single-pass beam corrupts some of the data taken of the tilt-immune double-pass interference pattern, as the single-pass pattern is not tilt-immune (not having passed through the PCE). Rotating the QWP in the target arm (QWP 1) reduced the intensity of the single-pass beam, but did not remove it entirely. With precise alignment the single-pass pattern can be made to sit above/below the double-pass pattern (see Fig. 5.5) and thus not disrupt displacement measurements, as was accomplished for Fig. 5.3, but this is not practical for real-world applications.

Using company-supplied data for the extinction ratio and AR coating of each of the components used in nEUCLID, the power of each part of the target beam was calculated. Assuming an input of 3.5 mW the total output power of the single-pass beam is 0.0020 mW, whilst the double-pass beam is 0.448 mW. This means only 0.45% of the target beam is travelling back to the photodiodes without passing through the PCE, which does not explain why the single-pass pattern appears to be so bright.

Integrating each of the two beams in Fig. 5.5 over the PD diameter (1.0 mm) gives an intensity of 44.7 µW for the double-pass beam, and 22.1 µW for the single-pass beam. This does not match the supplier data; approximately 30% of the total beam intensity is in the single-pass beam, not 0.45%.

These results are not consistent with the manufacturer's data, and thus this is an area that needs further investigation. The lenses, and waveplates were tested individually by monitoring the intensity output using just a laser, a photodiode, and the component in question. This experiment did not raise any immediate issues regarding the component quality, other than highlighting the importance of choosing an AR coating appropriate to wavelength. However, when the PBSs were tested the measured transmission value (when reflecting the beam) and reflectance value (when transmitting the beam) were both much higher than that specified by the manufacturer's data – 33% compared to 1%. Removing the single-pass beam is more involved than one may first assume, due to the target beam

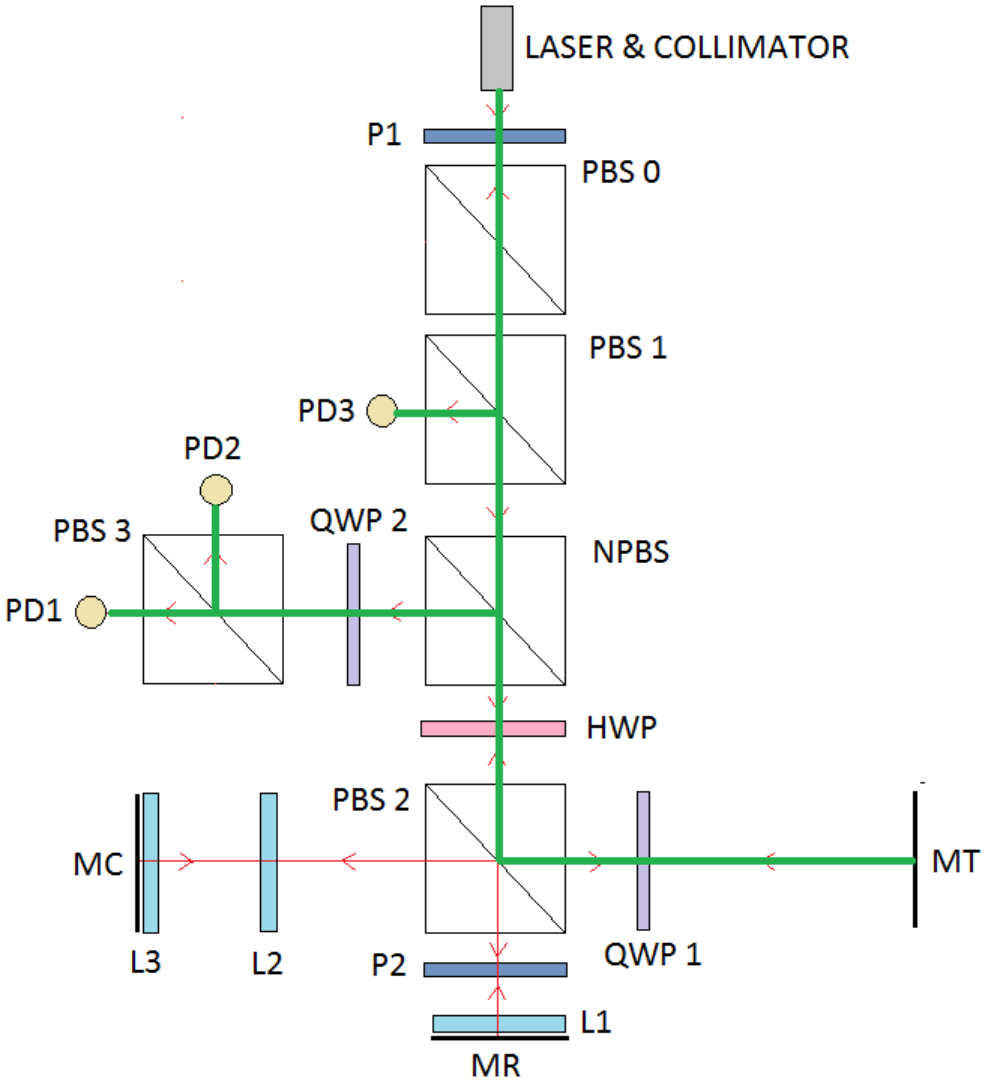

Figure 5.4: The beam passage of the single-pass target beam in nEUCLID, shown in green. The red lines remain to show the double-pass beam passage.

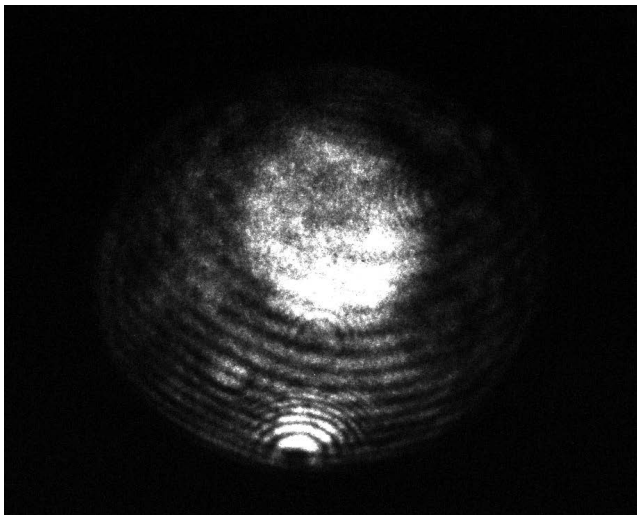

Figure 5.5: CCD photograph of the two interference patterns with the meniscus lens in the reference arm; the larger top pattern is from the double-pass, the smaller bottom pattern is from the single-pass. The faint large rings are caused by reflections from the incorrect AR coating on the PCE lenses - this was later rectified.

displacing when the target mirror is not at the sweet plane. E.g., An iris could not be used to pick out the target beam when away from the sweet plane, as this would partly blocked the target beam as it displaced across the reference beam. Section 7.2.1 discusses the options for removing or at least reducing the single-pass beam effect.

5.4 Matching Lissajous Patterns

As discussed in Section 3.3.3, the target beam will displace transversely across each photodiode if the target mirror is tilted when it is not at the sweet plane. The rays across the target beam have different phases as some have travelled further than others due to the divergence of the target beam (e.g. the centre rays compared to the edge rays). This is also the same for the single-pass beam.

Two changes to the Lissajous pattern are observed due to these effects. The first effect is due to the phase difference across the target beam because the beam divergence. This causes the Lissajous pattern to be traced out on the oscilloscope screen. The second effect is from the change in visibility incurred as the target beam moves across the reference beam, varying the interference pattern. This causes the Lissajous pattern to change shape.

Three photodiodes can see the same visibility if they are all aligned on the same part of the interference pattern to begin with. However, as the single-pass beam cannot be removed, when the target beam is tilted the phase changes, thus the Lissajous pattern traces out the phase and a "displacement" is measured.

The effect due to the phase difference across the target beam can be seen in Fig. 5.6a and Fig. 5.7a. A program was written to investigate this, taking photodiode intensity measurements incrementally across the modelled fringe pattern, and matching the results to those taken in the lab. The results are shown in Fig. 5.6b and Fig. 5.7b.

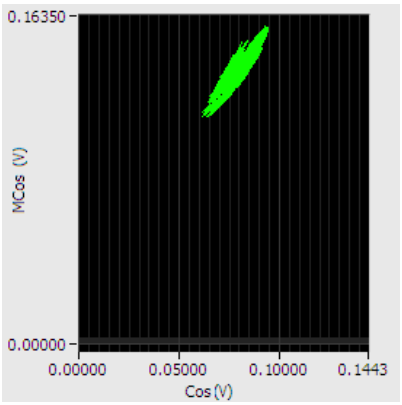

(a) In-phase Lissajous pattern from nEUCLID (green)

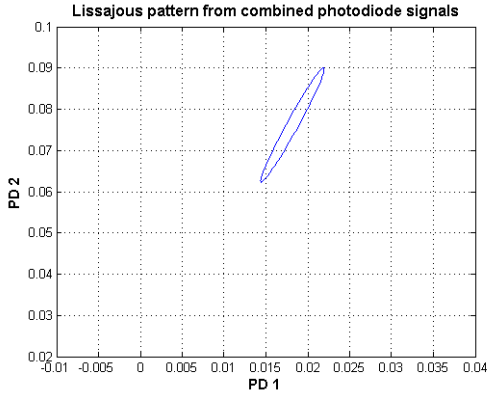

(b) Corresponding modelled in-phase Lissajous pattern

Figure 5.6: In-phase elliptical Lissajous pattern from nEUCLID in the lab (*a*) and via the computational model (*b*)

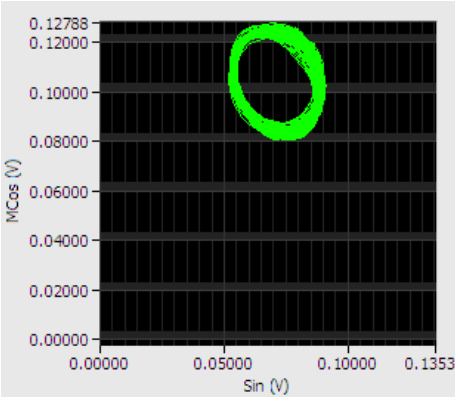

(a) $\pi/2$ out of phase Lissajous pattern from nEUCLID (green)

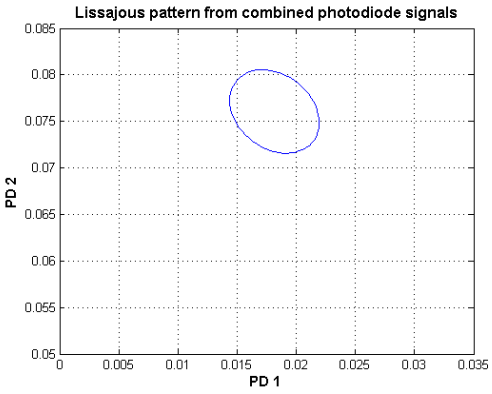

(b) Corresponding modelled $\pi/2$ out of phase Lissajous pattern

Figure 5.7: $\pi/2$ out of phase circular Lissajous pattern from nEUCLID in the lab (*a*) and via the computational model (*b*)

	b/a
In phase: theory	0.4665
In phase: data	0.4689 ± 0.04
Out of phase: theory	0.9947
Out of phase: data	0.9949 ± 0.06

Table 5.1: The ratio of semi-minor to semi-major axes, b/a, of the data and the models; Figure 5.6a to Fig. 5.7b.

The laboratory data were taken at 72 mm from the sweet plane, tilting the target mirror by 0.1° for each data set, but keeping the PDs fixed. The results show the Lissajous pattern in phase (an ellipse) and $\pi/2$ out of phase (a circle). The modelled data was achieved via the same process, albeit computationally. All data values are displayed in Table 5.1.

This method calculates the displacement of the target beam on the PDs. The phase shift depends critically on the overlap of the two beams. This experiment has reinforced the idea that diverging beams should not be used in an interferometer; the phase of the target beam with respect to the reference beam depends on the angle of the target beam. It is possible to suppress this effect by making the two beams overlap at the sweet plane, which has been achieved in the lab.

However, the predicted displacement from the computational model which matches what is observed in lab (i.e., Fig. 5.6 and Fig. 5.7), does not match the theoretical displacement calculated from Eq. (3.18) in Section 3.3.3. Using the z and θ_m used in the lab for the above experiment (i.e., $z = 72\,\text{mm}$ and $\theta_m = \pm 0.1°$) with Eq. (3.18), the displacement of the target beam with respect to the reference beam should be 0.20 mm. However, using the computational model, the amount of displacement required to produce the Lissajous patterns that match those observed in the lab is 0.015 mm. This experiment is difficult to model; it is a complicated system. The fringe visibility, the angle of the photodiodes, and the position of the photodiodes all have to be taken into account, thus it is not possible to accurately determine what is causing the discrepancy in results. This would mostly likely account for the slight angle of the modelled Lissajous patterns that is not seen in the observed data.

This experiment has shown it is possible to predict the shape of the Lissajous pattern for a set distance from the sweet plane, as the target beam is transversely displaced across the photodiodes. This shape can be optimised for better visibility by correct positioning of the photodiodes.

5.5 Removing the Focusing Effect of the PCE

Two unforeseen aspects limit the sensitivity of nEUCLID: the single-pass beam (described in Section 5.3), and the phase effect seen in the Lissajous pattern shape (described in Section 5.4). These two parameters are linked together by the focusing effect of the δ parameter described in Section 3.3.1. A better solution is needed than the one already described in this thesis – the addition of a meniscus lens, discussed in Section 3.4. This new solution is focusing the beam before it enters the interferometer.

The δ in the PCE creates a focusing effect at $1/\delta$ behind the sweet plane, as discussed in Section 3.3.1. The beam diverges past this point, and on to the photodiodes, expanding the fringe pattern. This expansion reduces the visibility of the pattern unless the reference beam radius of curvature and beam width are matched to the target beam.

However, as the following calculations show, simply adding an extra lens to the set-up can remove this focusing effect. A focused beam will also remove the need to reposition the photodiodes described in Section 5.4, as the beam will remain collimated through the interferometer.

The input laser beam in nEUCLID passing through the working distance, s, through the PCE and back towards the photodiodes can be represented by the matrix, M_S,

$$M_S = \begin{pmatrix} \delta s - 1 & \delta s^2 - 2s \\ \delta & \delta s - 1 \end{pmatrix}. \tag{5.1}$$

If a lens, L_n, of focal length, f, is placed in front of this system, for example between the HWP and PBS 2 in Fig. 4.2, the overall result becomes

$$M_{SL} = \begin{pmatrix} 1 & 0 \\ -\frac{1}{f} & 1 \end{pmatrix} \begin{pmatrix} \delta s - 1 & \delta s^2 - 2s \\ \delta & \delta s - 1 \end{pmatrix} \begin{pmatrix} 1 & 0 \\ -\frac{1}{f} & 1 \end{pmatrix}, \tag{5.2}$$

which becomes

$$M_{SL} = \begin{pmatrix} \frac{\delta f s - \delta s^2 - f + 2s}{f} & \delta s^2 - 2s \\ \frac{\delta f^2 - 2\delta f s + \delta s^2 + 2f - 2s}{f^2} & \frac{\delta f s - \delta s^2 - f + 2s}{f} \end{pmatrix}, \tag{5.3}$$

If the focal length of the new lens, f, is equal to the working distance, s, Eq. (5.3) reduces to

$$\begin{pmatrix} 1 & \delta s^2 - 2s \\ 0 & 1 \end{pmatrix}, \tag{5.4}$$

Using Gaussian optics, if the ABCD matrix components of Eq. (5.4) are tested with the PCE values of nEUCLID the change in the divergence of the beam, D, with the new lens is negligible [34, pp. 664 & 783]

$$q_0 = -\frac{i\lambda}{\pi w_0^2}, \qquad \frac{1}{q} \equiv \frac{1}{R_c} - i\frac{\lambda}{\pi w^2}, \tag{5.5}$$

where w_0 is the beam waist, and w is the output beam width.

Re-defining q in terms of ABCD matrix components using [p. 784][34], the radius of curvature, R_c, is

$$R_c = \left[\mathrm{Re}\left(\frac{C + Dq_0}{A + Bq_0} \right) \right]^{-1} = -7.06 \times 10^6 \,\mathrm{mm}. \tag{5.6}$$

The new output beam width, w_{out}, can also be compared,

$$\frac{1}{w_{out}^2} = \frac{\pi}{\lambda} \mathrm{Im}\left(\frac{C + Dq_0}{A + Bq_0} \right), \tag{5.7}$$

$$w_{out} = 8.0014 \,\mathrm{mm}, \tag{5.8}$$

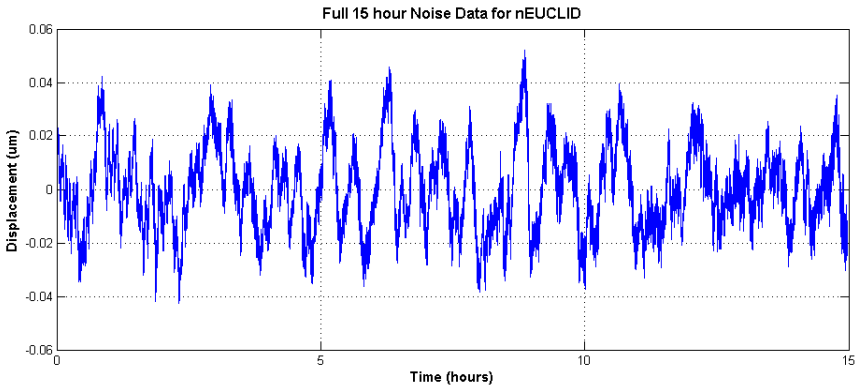

Figure 5.8: The full 15 hours of noise data collected for nEUCLID in air. The data have been de-trended to remove the thermal expansion effect of the aluminium rail nEUCLID is mounted on.

in comparison to the beam width at the input of nEUCLID, $w_{in} = 8.00\,\text{mm}$.

A lens is still required in the reference arm, to negate the focusing effect in the reference arm.

5.6 Sensitivity of nEUCLID

A noise performance plot of nEUCLID in air was taken for 15 hours to measure the sensitivity of the device. The optical bench was suspended to remove vibration effects, all laboratory lights were switched off to remove potential intensity interference on the photodiodes, the air conditioning system was off and the interferometer was covered with a cardboard box to protect it from air currents. The full data set is shown in Fig. 5.8. The data have been de-trended to remove the long-term effect of thermal expansion of the aluminium rail that nEUCLID is mounted on. The 15 hours of data were cut into samples of 100 seconds to produce Fig. 5.9.

From the data presented in Fig. 5.9 nEUCLID has a sensitivity of $4.20 \times 10^{-10}\,\text{m}/\sqrt{\text{Hz}}$ (at 1 Hz, in air). The plotted points representing the ASD of EUCLID are joined by a dashed line to guide the eye only.

From the ASD shown in Fig. 5.9, between 0.1 Hz and 10 Hz the system appears to be dominated by 1/f noise. A likely culprit for this noise is the DFB laser. Lasers can be susceptible to phase noise – random, short-term fluctuations in the phase of the wave (e.g. random fluctuations around a perfect sine wave) [41]. It affects the coherence length of the laser by limiting the linewidth of the beam, thus limiting the frequency stability (monochromaticity) of the laser. EUCLID also experiences this noise between 0.1 Hz and 10 Hz [9]. Issues of frequency noise in the laser are further described by S. Aston in [9], and in Section 2.6.2. Below 0.1 Hz the sensitivity is most likely dominated by air turbulence.

Comparing nEUCLID with EUCLID in Fig. 5.9, it can be seen that there is a factor of approximately 10 between the ASD value for each system. This is most likely due to the armlength difference. Unequal armlengths in interferometers cause extra noise in the

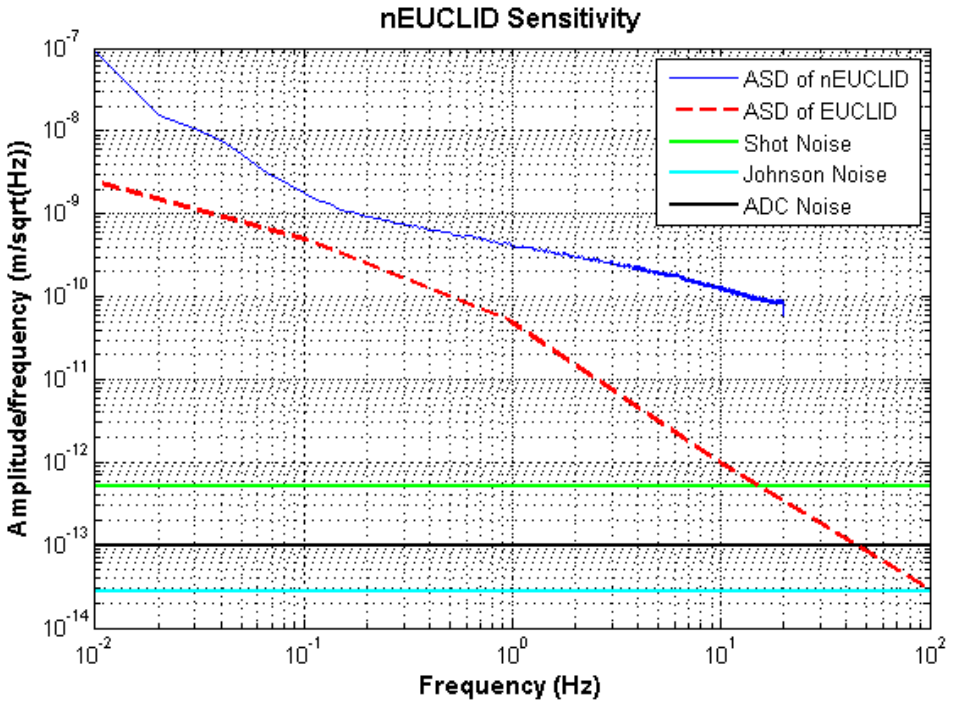

Figure 5.9: The sensitivity plot of nEUCLID in air, with the relevant noise sources included. A comparison of the ASD of EUCLID is also shown on the figure.

system; phase noise scales with armlength difference. Therefore, noise that is insignificant in EUCLID could be significant in nEUCLID. In the ideal case the sensitivity of an equal armlength nEUCLID would have been tested, but unfortunately there has not been time to do this. It is not expected that the sensitivity of nEUCLID would match that of EUCLID due to the unequal armlengths.

The laser linewidth, L, can be estimated as the rms noise variation of the laser frequency. This can be calculated by integrating the PSD – the square of the ASD – as described by Eq. (2.52) in Section 2.6.2. The measured ASD $A_z(f)$ can be converted to a frequency ASD $A_\nu(f)$ using the frequency of the laser f_0 and the armlength difference L of the interferometer:

$$A_\nu(f) = A_z(f)\frac{f_0}{l} \tag{5.9}$$

Using Eq. (2.52), a value of L is calculated as approximately 1 MHz (where $f_1 = 10^{-2}$ Hz, $f_2 = 2 \times 10^1$ Hz, and $l = 2.62$ m). This value is consistent with the laser specifications.

Whilst the ASD for nEUCLID doesn't extend beyond ~ 10 Hz (due to the small amount of noise data taken), at high frequencies the system will likely be dominated by shot noise, as observed in EUCLID [9, pp. 126–128]. The predicted shot noise for nEUCLID is described below in Section 2.6.1. It would be prudent to take longer and more numerous noise data sets for nEUCLID, to confirm this prediction.

5.7 Noise in nEUCLID

The following noise sources were identified and calculated for nEUCLID. For further details on their derivations, please refer to Section 2.6.

5.7.1 Shot noise

Using Eq. (2.50), the shot noise for nEUCLID is $8.47 \times 10^{-7}\,\mathrm{V}/\sqrt{\mathrm{Hz}}$, where the photocurrent of the photodiodes is1 µA, the transimpedance amplifier gain is 187 kΩ, and the voltage gain is 8.

nEUCLID has displacement sensitivity from shot noise of $\approx 5.2 \times 10^{-13}\,\mathrm{m}/\sqrt{\mathrm{Hz}}$, where the approximate radius of the Lissajous pattern produced by the interferometer is 0.1 V.

5.7.2 Johnson noise

Using Eq. (2.53) the Johnson noise for nEUCLID is $2.73 \times 10^{-14}\,\mathrm{m}$ per $\sqrt{\mathrm{Hz}}$.

5.7.3 ADC noise

Using Eq. (2.54), where the ADC utilisation is 0.5, and the ADC voltage input range is 4 [9], the displacement noise is $9.86 \times 10^{-14}\,\mathrm{m}/\sqrt{\mathrm{Hz}}$.

5.8 Summary

The model of the interference pattern with the meniscus lens been proven correct with laboratory data, confirming the understanding of nEUCLID and the PCE within an interferometer. The tilt immunity at the sweet plane has been compared with the tilt of a mirror at the sweet plane without the PCE, proving the PCE is necessary for tilt immunity at ranges over 660 mm. This working distance is very impressive, compared to the maximum working distance of 59 mm of previous University of Birmingham tilt-immune interferometers. This distance also fulfils the brief of Airbus DS as, despite not being a full metre, this working distance still proves the concept.

Fig. 5.3 shows the working range of nEUCLID is ±120 mm. A tilt immunity of ±0.35° is achievable from the sweet plane (0 mm) until ±120 mm. This level of tilt immunity is to be expected for such a large working range, thus is within specification for the brief from Airbus DS.

The sensitivity of the device is $420\,\mathrm{pm}/\sqrt{\mathrm{Hz}}$ (at 1 Hz, in air). The relevant noise sources are shown on Fig. 5.9, and are all at least a factor of 100 below nEUCLID sensitivity range (in air) thus currently do not impact hugely on nEUCLID. The ASD for EUCLID is also shown, but for a vacuum, so the results are not comparable. The sensitivity value shows that vacuum testing is necessary to improve the resolution of nEUCLID, and to be able to compare it accurately with EUCLID.

Chapter 6

POTENTIAL SPACE APPLICATIONS FOR nEUCLID

6.1 Applications

As the space industry continues to grow new technology has become necessary to advance future missions. ESA's Technology Research Programme (TRP) requests calls for new technologies throughout the year across all disciplines, from propulsion systems to laser metrology devices, Earth observation science to human spaceflight.

This is where new technology such as nEUCLID is called for; a small, low mass, adaptable sensor would be key to future successes for composite structures in space, as well as formation flying missions. Whilst on the ground, it has become crucial for next-generation antennas to have surface and pointing accuracy of micrometres, to collect and measure data with extreme precision.

This chapter will discuss in detail the variety of applications for nEUCLID, and how it meets the necessary requirements.

6.1.1 Ground-based Applications

Ground-based applications within the space industry are an area of interest for nEUCLID; the multitude of tests carried out on satellites before they are launched are fundamental to the success of a mission, thus testing on the ground is as important as functioning in space.

Vibration Monitoring

Vibration testing shocks and shakes satellite components to model spaceflight conditions, to ensure the craft can withstand launch and deployment. This includes electrical parts as well as structural and mechanical. Sensors are used to monitor movement during

Figure 6.1: ESA's LPF satellite being vibration tested [43]

launch-simulation testing, thus a small and accurate sensor with the necessary tolerance is highly desirable.

Testing is done at certain resonant frequencies which elements of the craft are known to self-vibrate at once launched. This testing ensures the equipment will not degrade upon launch, and will function successfully. Figure 6.1 shows an example of vibration testing on ESA's LISA Pathfinder (LPF).

There are three main types of vibration testing: sine, random and shock [42]. Sine testing subjects the spacecraft to an increasing range of frequencies and amplitudes; random testing uses a broad band of frequencies, to simulate more realistic real-life scenarios; shock testing uses a rapid high-energy pulse of short duration. Typical sinusoidal testing of LISA Pathfinder is 20 Hz to 100 Hz up to 60 g [43]. nEUCLID can currently measure 6 g at 100 Hz, due to limitations of the sampling speed of the electronics; the phase wrapping of nEUCLID is $\lambda/16$ in 1 µs, giving a maximum tracking speed of $96.8\,\mathrm{mm\,s^{-1}}$, and thus an acceleration of approximately $60\,\mathrm{m\,s^{-2}}$, or 6 g.

Piezoelectric accelerometers are the most commonly used devices for measuring vibration-induced displacement in the space industry [44]. They use the piezoelectric effect of quartz to generate an electrical output proportional to the applied acceleration from the component being tested. Using piezoelectric accelerometers, a displacement of ± 12.7 mm can be expected for a typical spacecraft vibration test [45].

However, accelerometers are heavy; the average mass of an accelerometer is 1.2 g, which seems small but if there are 100 or so over the spacecraft the overall mass can be great. For light structures this is a particular problem, as the extra mass of accelerometers can change the vibration testing results. Remote displacement sensing using devices such as nEUCLID would eliminate this problem. Remote sensing is also very useful from a cleanliness point of view. During testing the spacecraft needs to be kept as clean as possible, to prevent potential damage to electronics and equipment. Removing accelerometers from the test procedures would ensure the spacecraft would remain as clean as it entered the testing facility (barring vibrational damage).

Several nEUCLIDs would be required to monitor different positions on larger crafts; however, this is also how accelerometers are used in testing. Only an accuracy of tens of micrometres is required, for millimetres of displacement. However, with future needs

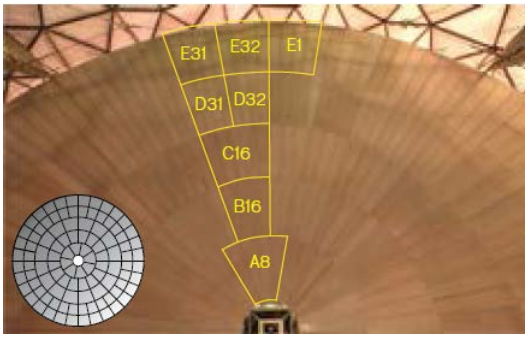

Figure 6.2: An example of the panel sections on a larger antenna dish, with the full design in the bottom left-hand corner. (The HUSIR antenna, taken from [47]).

of more accurate test results, nEUCLID would easily fulfil requirements of nanometres of accuracy over micrometres of displacement, making it an ideal candidate for this application.

Antenna Monitoring

Once an antenna dish has been manufactured the surface needs to be calibrated, to ensure the antenna will produce the correct gain and radiation pattern. If there is an error in either of these values the radiation may be scattered, and the antenna footprint could either be incorrectly positioned or the wrong size [46].

Most large antenna dishes (e.g. for microwave or radio observatories) are made in sections – "panels" – and fitted together at the end of the manufacturing process, as shown in Fig. 6.2. It is crucial to ensure all panels are correctly positioned and aligned with each other, otherwise the accuracy of the antenna is compromised. The current method uses a coherent laser radar (CLR) to measure reflections from the surface – a non-contact method to protect the surface. The device uses heterodyne detection (described in Section 2.3.2) to make several different measurements of the surface, e.g. one at each panel corner. The surface measurement is compared to a theoretical paraboloid of the same size and shape. If necessary, the panels are readjusted and the process repeated until the alignment has an acceptable tolerance (usually tens of micrometres) [47].

Similar to coherent laser radar is the laser absolute interferometer, mass marketed as a "laser tracker". The leading company in designing these is Leica, and they also use heterodyne detection to measure surfaces [48]. An example of the accuracy using such a device for antenna panel surface measurement is $\pm 0.5\,\mu\mathrm{m\,m}^{-1}$ [49]. These devices are able to rotate horizontally by 360° and vertically by ±45° [50], so are more flexible in range than nEUCLID. However, they are extremely large ($2.5\,\mathrm{m} \times 5\,\mathrm{m} \times 10\,\mathrm{m}$ [50]), and thus can only be used in larger laboratories and clean rooms.

Microwave holography is also used to align and measure the surfaces of antennas. Many of the world's large radio astronomy antennas have been aligned using holographic techniques, for example National Aeronautics and Space Administration (NASA)'s Jet Propulsion Laboratory (JPL) deep-space network of antennas [51]. Microwave holography provides a detailed map of the antenna surface, which is compared to the ideal surface and the antenna panels are adjusted to minimize the difference, as with the CLR method. An example of system accuracy is the HUSIR system at the Lincoln Laboratory, which generates a map

of the surface errors in less than half an hour with a spatial resolution of 0.6 m and an accuracy of 20 µm [47].

As discussed above, either several different positions on the antenna would need to be monitored, or a large movement range of the measurement device is required. To use the current nEUCLID would be time-consuming, due to measuring displacement relatively – it would have to be moved to each position or the antenna dish would have to be rotated, requiring extra space in the test room. However, if nEUCLID was made absolute (as discussed in Section 7.2.2) this would alleviate that problem, and nEUCLID could be used in the same way as the CLR. The accuracy of nEUCLID would be very acceptable for this application; the more precise the knowledge of displacement errors, the better the knowledge of the accuracy of the antenna signal. The size of nEUCLID is also very beneficial in this application; many surface-measuring devices are floor-standing, thus require a larger amount of space to perform measurements than nEUCLID needs.

Thermoelastic Testing

Thermoelastic testing is another test required for spacecraft characterisation. The craft is placed in a large thermal vacuum chamber and heated and cooled to see how the materials deform. This test currently uses cameras to take images of the entire antenna, with small discs positioned on the antenna for reference. The accuracy of the camera is only 10 µm [52] [53], thus again nEUCLID is slightly too accurate for this application.

However, future thermoelastic testing may require improved accuracy as a resolution of nanometres is not achievable with current camera technology. If nEUCLID was used it would have to scan the antenna in order to cover the full area, or use many nEUCLIDs, each monitoring a different position.

6.1.2 Space-based Applications

Space-based applications for nEUCLID are wide-ranging, due to the versatility of the design. A sensor for large-scale structures and optics, such as next generation telescopes that will unfold upon launch; continuous monitoring of position, such as in formation flying missions; on-board a spacecraft, monitoring body distortion or antenna positioning, are all possibilities for a sensor such as nEUCLID.

Adaptive Optics

The next generation of space observatories will be substantially larger and use wider mirrors; this has already begun with the design and subsequent building of the JWST. The use of larger mirrors means that to launch these will be folded into separate segments or panels, and will be deployed and aligned once in orbit.

The JWST is the next large space observatory. It will launch folded inside the rocket and will unfold once deployed in space. The 6.5 m diameter mirror has two side segments that will unfold to form the full mirror [3]. These will be controlled and positioned by actuators

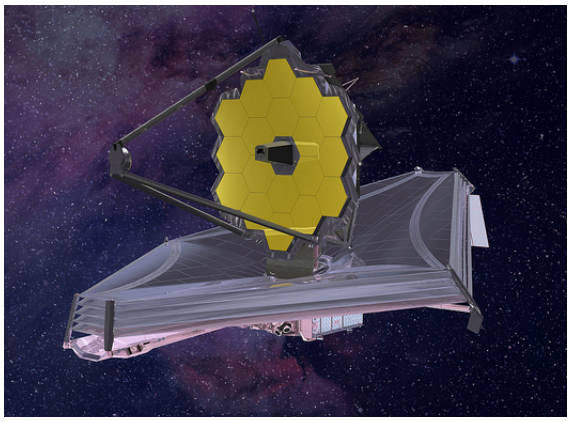

Figure 6.3: Artist's impression of the JWST [54]

[3], and the image quality calibrated using a complex algorithm performed by the on-board computer. This method will be used to monitor the image quality every few days, using the actuators to perform micro-adjustments as necessary.

Capacitive sensors can also be used, either separately to or alongside actuators. Capacitive sensors use the movement of a suspended electrode with respect to a fixed electrode (e.g. on a mirror compared to on the mirror strut) to establish a varying capacitance between the two electrodes. This effect can be measured and the result converted into a displacement of the suspended electrode [55]. However, capacitive sensors can be quite susceptible to environmental noise, e.g. from on-board electronics or temperature gradients (the smaller the sensor, the noisier it is) and thus are limited in their displacement sensitivity. Interferometers are becoming smaller yet more sensitive to displacement, but not necessarily to such noise; this is limited by the electronics [9, pp. 126 - 128]. They are widely available for such applications [56], thus why nEUCLID would be applicable in these situations. Currently, nEUCLID has only been tested with highly reflective surfaces (i.e. mirrors). However, it can make displacement measurements with a low intensity return beam (less than 50% of the original intensity, as discussed in Section 5.2). Further testing of different machined surfaces would be required to ensure how reflective the measurement surface needs to be.

Baseline Metrology

A more specific applications within satellite metrology is monitoring particular parts of the attitude system with respect to a payload. One example is the Wind Velocity Radar Nephoscope (WIVERN), a proposed earth-observation satellite to monitor wind speeds, rainfall and cloud ice water [57] (Fig. 6.4a). It has a spinning payload, separate to the stationary body of the craft, that requires continuous position monitoring of an accuracy of 200 µrad [58]. Three nEUCLIDs would be positioned around the stationary payload and monitor the displacement between the star tracker axis and the spinning payload axis, recording any errors in spin/pointing. For example, if the length of the payload was 0.5 m and it tilted by 200 µrad, nEUCLID would measure a displacement of 100 µm.

Once again there is no current on-board system to monitor this displacement. The most common method is to use a star tracker to ensure the satellite (and payload) is pointing

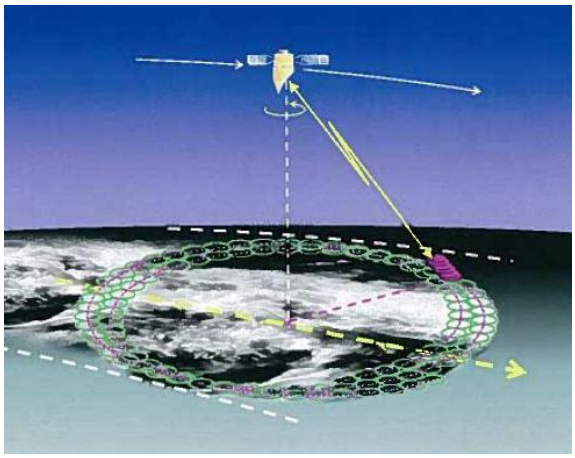

(a) Artist's impression of WIVERN in orbit [57]

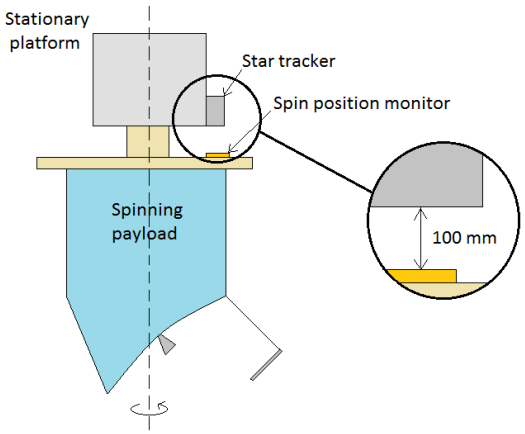

(b) Sketch of WIVERN body, showing distance to be measured by nEUCLID

Figure 6.4: WIVERN: WInd VElocity Radar Nephoscope

in the correct direction. Star trackers measure the position of the visible stars using a camera, and compare the collected image with an on-board catalogue to match the stars in the image to a known position in the sky. They are highly sensitive to light (+ 9 magnitude, with $\pm 1.5''$ [59]), thus can miscalculate in sunlight reflected from the satellite. nEUCLID could be used in tandem with a star sensor, to monitor the displacement between the attitude system and the payload (as shown in Fig. 6.4a).

Another application is the monitoring of antenna phase centres for future missions. Antenna phase centres are the position of the apparent source of radiation, thus must be monitored to ensure the beam is orientated correctly onto the Earth. Future Earth Observation (EO) missions plan to use long antennas (and thus place antenna phase centres further from the craft) to cover a wider area on Earth [60]. This application would require an accuracy of µm over distances of tens of metres. There is currently no technology with a technology readiness level (TRL) higher than 5 that is capable of achieving this [31]. nEUCLID is capable of measuring nanometre displacements at distances of tens of metres, so would be extremely suitable for such an application.

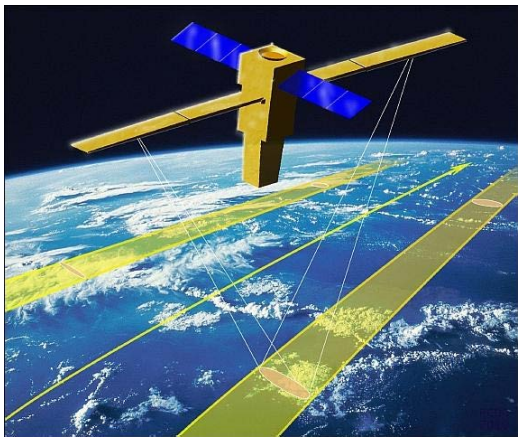

Figure 6.5: Artist's impression of Wavemill showing the antenna beam tracks on Earth [61].

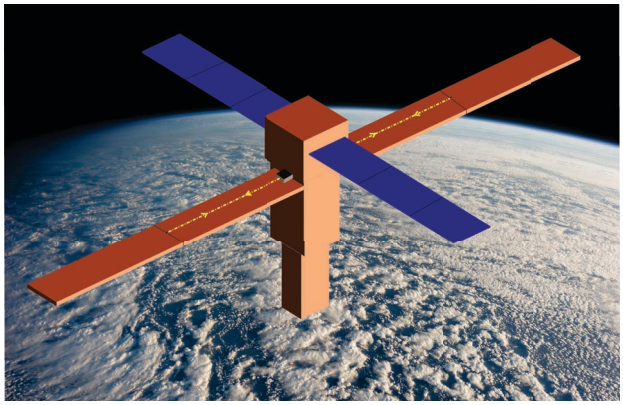

Figure 6.6: Artist's impression of nEUCLID monitoring the phase centres of Wavemill; nEUCLID is shown as a grey box, with yellow lines representing the beam line to/from the antenna centres.

An example of such an application is the ESA mission, Wavemill, to be launched in 2020. Wavemill is a mission to study the spatial and temporal variations in currents in open ocean and coastal waters, with a resolution of less than 5 km. The craft is shaped in a "javelin" configuration with two antenna arms. These arms separate the antenna beams into across-track and along-track directions, creating an elliptical footprint on Earth, as shown in Fig. 6.5. It is vital to know the position of the phase centre of each antenna, to confirm it is pointing in correct direction and hasn't shifted, and thus moved the beam track.

The distance between the two phase centres is 12.4 m; the required accuracy is 10 µm (including errors) [62]. Figure 6.6 shows how nEUCLID would be positioned on the Wavemill satellite. As previously mentioned in Section 2.7, INRiM have created a device with 5 degrees of freedom to enable the phase centres on Wavemill to be monitored. This device is known as COATS, and is capable of measuring ±10 mm at a distance of over 100 m, and ±350″ at 7.5 m for angular measurements. The distance resolution is 1 µm at 1 Hz.

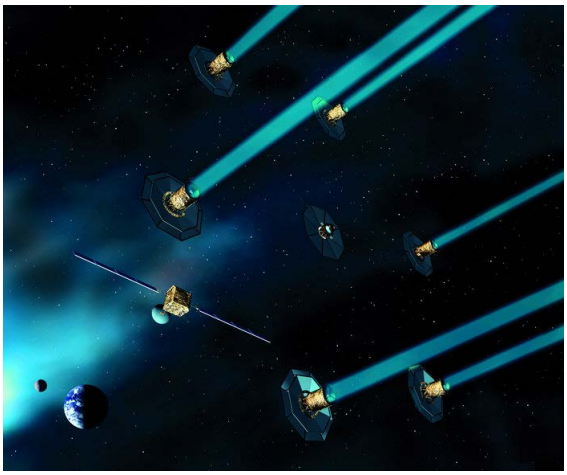

Figure 6.7: Darwin spacecraft formation showing the six collector spacecraft with beams, the central combiner spacecraft, and the communications satellite [64].

Formation Flying

One of the more exciting types of future missions is formation flying. This type of mission consists of two or more satellites flying in formation – a "constellation" – to replace the need for a larger single satellite.

Formation flying has several benefits:

- increased flexibility; can change roles of satellites
- minimum degradation; failure of one satellite does not necessarily cause failure of entire mission
- lower mission cost, due to reduced total mass put into orbit
- reduced redundancy; scientific instruments spread across satellites

Currently there is no position sensor sensitive enough for such a mission, to monitor the position of each individual satellite with a high enough precision of tens of micrometres/hundreds of nanometres. There have been several planned missions in the last decade (e.g. Darwin, Terrestrial Planet Finder (TPF)), but these were abandoned in part due to lack of technology. NASA's Gravity Recovery and Climate Experiment (GRACE) mission is the best current demonstration of precision formation flying; microwave ranging monitors the position of two satellites in constellation. However, laser ranging from ground stations is still performed.

The Darwin mission was proposed by ESA as a constellation of four to five free-flying spacecraft to search for Earth-like planets around nearby stars. Three (or four) of the satellites would have carried small telescopes, to be focused to the central satellite in the constellation. These would have to stay in formation with millimetre precision; a deviation of more than 100 µm would have ruined observations [63]. The mission was retired in 2007 due to lack of sufficient technology to maintain this position accuracy.

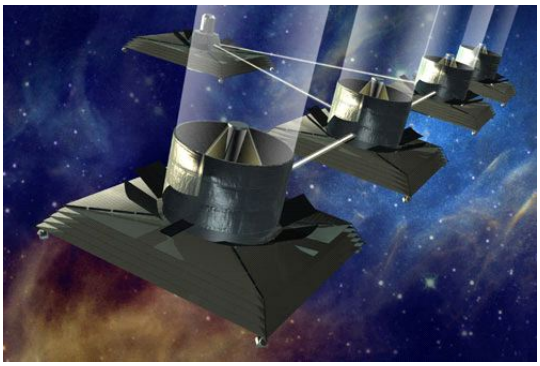

Figure 6.8: NASA's TPF interferometer; a telescope of several satellites flying in formation [65].

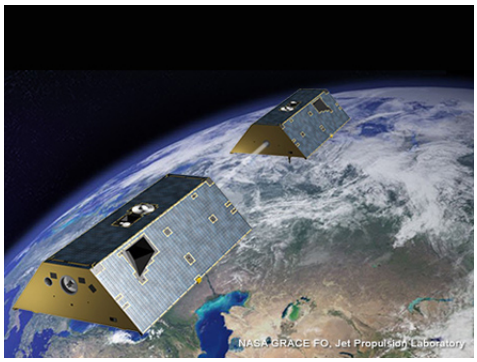

Figure 6.9: NASA's GRACE Follow-On mission; two spacecraft flying in formation to monitor variations in the Earth's gravitational field [70].

The TPF was a formation flying mission proposed by NASA to study planets outside of the Solar System. One design was for a large telescope to be constructed from several small telescopes, each on a separate spacecraft, flying in close formation. The mission was cancelled in 2011.

However, in the last few years investment has been made in formation flying technology (e.g. Proba-3 [66], and GRACE Follow-On [67]), as the importance of these missions has been realised.

The GRACE Follow On is a joint mission between NASA and German Research Centre for Geosciences (GFZ), due to be launched in 2017. It will continue the mission of GRACE, monitoring the variations in the Earth's gravitational field, but will also test a new technology for precise formation flying – a Laser Ranging Interferometer (LRI). As well as the microwave ranging system used in GRACE, the two satellites will use the LRI to monitor the distance between two craft [68], improving the accuracy by two orders of magnitude, down to $80\,\mathrm{nm}/\sqrt{\mathrm{Hz}}$ in the measurement band between 2 mHz and 0.1 Hz [69].

Another formation flying mission in development is Proba-3, an ESA mission due to launch in late 2018. Proba-3 consists of two satellites which will fly with close precision to study the Sun's corona. The craft will fly several kilometres apart for most of the mission, but will be only 150 m away during formation manoeuvres. Neptec UK, with Micos of Switzerland, are developing the metrology system for the mission [66].

Figure 6.10: ESA's Proba-3 mission; one satellite shielding the other from the Sun [71].

Because there is no satisfactory technology simple enough to allow mass formation flying missions to go ahead with the desired precision, current telescope designs are restricted in length to the size of the launch fairing. This limits the size of future large-scale observatories.

nEUCLID would be extremely suitable for formation flying; it is small enough to fit on satellites of this size, yet can theoretically work over ranges of kilometres with micrometre accuracy (with the target mirror scaling accordingly with the beam divergence). With the current nEUCLID PCE system a distance s of 1.0 km is achievable (neglecting tilt immunity, as discussed in Section 2.7). nEUCLID is not yet an absolute interferometer (see Section 7.2.2), but has both the accuracy and low mass required for such missions.

Pointing Knowledge

A satellite antenna should point in the direction of its target on Earth at all times; the antenna boresight (the axis of maximum radiated power) should remain central within the coverage area (e.g. to 100 km for earth observation missions [58]). The attitude and orbital control system, comprising sensors, trackers and gyroscopes, keeps the satellite fixed within its reference frame. However, depointing can occur, causing the boresight to leave its optimum position. Away from the boresight the antenna gain decreases, weakening the signal to the intended position on Earth. The depointed signal can also interfere with other up/downlink signals, creating excess noise.

Whilst more often a product of satellite motion about its centre of mass or orbital motion, depointing can be caused by a mechanical or thermal deformation in part of the attitude system, or in the antenna itself [74]. nEUCLID would be mounted on the main spacecraft body to monitor the deformation and relay data to the central on-board control system, enabling repositioning of the satellite to correct for any incurred depointing.

There are three main systems of antenna pointing mechanism (APM); tracking from a ground station ($\pm 0.015°$ accuracy [75]), re-pointing ($\pm 0.01°$ accuracy [75]) and steady-state pointing ($\pm 0.01°$ accuracy [75]). Tracking is expensive: a radio frequency (RF) sensor signal from the antenna is relayed to a ground system where its position is analysed, then corrections are relayed back to the on-board computer to reposition the antenna. Time taken to relay the signal to ground and back is time the satellite is not in commercial

(a) Artist's impression of the orbit of MetOp Second Generation (MetOp-SG), an ESA earth observation satellite. [72]

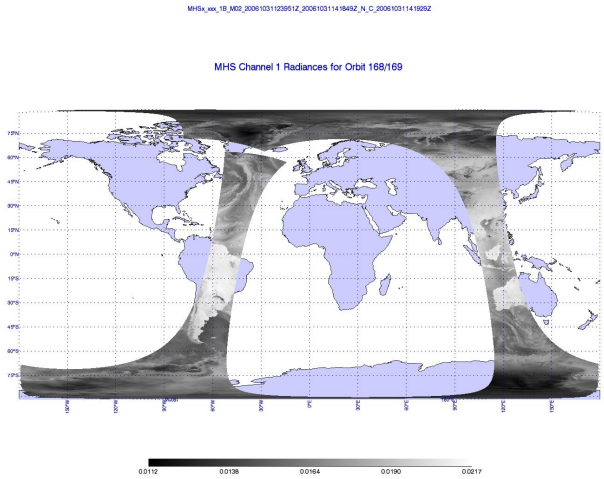

(b) The orbital path of MetOp-A, an earlier ESA earth observation satellite. [73]

Figure 6.11: Two of ESA's earth observation satellites; MetOp-SG (*a*) and MetOp-A (*b*).

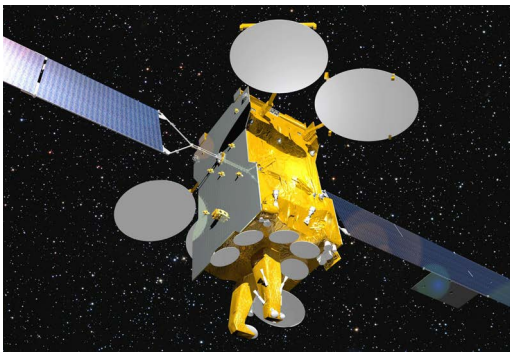

Figure 6.12: Eutelsat 3B, a standard telecommunications satellite built by Airbus DS [78].

operation. This causes the telecommunications company to lose money, especially if the satellite has to make several alignments via ground stations.

Steady-state pointing ensures an antenna remains at a pre-defined angle, whilst re-pointing is applied whenever an antenna has become slightly mispositioned. Re-positioning is generally achieved using a gimbal-drive; a pivoting device that allows rotation about two axes.

An IR sensor is used with the RF sensor to monitor antenna depointing. The sensor is aligned with the mechanical axis of the antenna to record any thermal expansion. The sensor does not measure the displacement directly, but relays the information with the RF sensor to the on-board computer to re-position the antenna as necessary [76]. Errors can occur in the tracking mechanism, caused by RF signal to noise ratio or beam polarisation (circular is used, as linear causes an extra tracking error as the satellite rotates) [77]. The gimbal system used to re-position antennas can also fail, meaning that whilst this system is currently good enough it is not completely reliable.

Currently there is no complete on-board APM; signals are sent from the satellite to the ground station and back to the on-board computer, which can become expensive over time. The use of nEUCLID as the displacement sensor would reduce the cost of monitoring the antenna positioning (removing the use of the IR sensor), as well as reducing the processing time and power required to make such a measurement, as a ground link would no longer be crucial.

In future, telecommunication companies may want to be able to cover smaller, more precise regions, such as cities. This will need an improvement in the current pointing accuracy. Again, due to the nanometre sensitivity of nEUCLID this would be achievable using nEUCLID as a displacement sensor to inform the on-board computer of any depointing of the antenna dish.

Commercial telecommunication satellites use high gain antennas with very narrow beams to produce well-defined coverage on the ground. High antenna gains are achieved using large reflector dishes, of the order of 5 m. Figure 6.12 shows a typical ESA telecommunications satellite. Due to telecommunications satellites regularly going into and coming out of eclipse large temperature changes ($-80°$ to $180°$ [79]) induce thermoelastic distortions of the dishes. These generate periods where the beam alignment, thus the gain on the ground, is not optimal, affecting the signal. Both telecommunications and science mission satellites

require optimal antenna alignment, so this is a problem for all satellite missions. The current nEUCLID is not capable of withstanding such a temperature difference. However, due to the simplicity of the design, it would not be difficult to replace the optics with more robust components, and to shield the electronics inside the spacecraft body as done with the on-board computer.

Concerted effort has been made to control this deformation; strips of lead zirconate titanate (PZT) are applied to the antenna structure, to be used as actuators. An electric field is applied, causing the strips to expand or contract as required, bending the antenna and correcting the beam shape [79]. However, there is no mechanism on-board to monitor the deformation. As with antenna pointing a feedback loop using ground stations checks the antenna gain and adjusts the dish using APMs and the PZT actuators. As mentioned earlier, ground station feedback is time-consuming and expensive.

nEUCLID would monitor several positions on the antenna on-board the satellite, informing the on-board computer of changes in deformation, removing the need for the ground station loop and saving time and processing power. nEUCLID could also be used in a very similar fashion to monitor thermal deformations of the satellite body.

6.2 Summary

nEUCLID can be applied to several ground-based and space-based applications. Whilst some areas, such as ground-based antenna metrology, have technologies with the accuracy required, other areas, such as formation flying and antenna metrology, are sorely lacking. Table 6.1 shows how nEUCLID compares to past/future mission specifications for space applications, and what is already available for certain ground applications. The most promising current applications are a formation flying sensor (comparing an accuracy of 420 pm at 0.66 m with and accuracy of 1 mm at 150 m), a position sensor for adaptive optics (0.42 nm compared to the required 10 nm), and a position sensor for large-scale deployable structures (working at a current distance of 20 m). The other applications defined in the table are not completely beyond the capabilities of nEUCLID; slightly more time would need to be given to the design to achieve the specified goals, e.g. as a sensor for vibration monitoring of satellites the electronics need to be able to sample at higher speeds (Section 6.1.1).

On the ground nEUCLID can be used as a remote sensor for vibration monitoring and thermoelastic testing, ensuring the craft remains clean and the results are not disrupted by extra loads, as is currently the case with accelerometers. It is also capable of antenna metrology, measuring dish distortion during formation and testing of the antenna reflector dishes.

In space, nEUCLID could be used as a position sensor for adaptive optics, to ensure large-scale observatories were deployed properly and the position maintained. nEUCLID would be extremely helpful for pointing knowledge, removing the need for ground stations relays to confirm antenna alignment, and also again for antenna baseline metrology, to monitor any antenna deformation during the mission.

Finally, looking to the future, nEUCLID could be one of the contenders for formation flying - a small, low-mass, low-power device capable of measuring nanometre displacement over

Application	**Mission**	**Requirement**	**Ref.**	**nEUCLID Spec.**
Vibration Monitoring	-	12.7 mm at 100 Hz	[45]	120 pm at 100 Hz
Antenna Metrology	-	20 µm at $s = 0.6$ m	[47]	420 pm at $s = 0.66$ m
Thermoelastic Testing	-	10 µm at $s \approx 1$ m	[53]	420 pm at $s = 0.66$ m
Adaptive Optics	JWST	10 nm	[80]	0.42 nm
Baseline Metrology	Wavemill	10 µm at $s = 12.4$ m	[62]	420 pm at $s = 0.66$ m
Formation Flying	Proba-3	1 mm at $s = 150$ m	[81]	420 pm at $s = 0.66$ m
Pointing Knowledge	NG telecomms.	10s of nm/$\sqrt{\text{Hz}}$	[43]	420 pm/$\sqrt{\text{Hz}}$

Table 6.1: Table of characteristics showing how nEUCLID meets the requirements for one example in each application area. Where no mission is defined the technology is applicable to the whole field. Note: 420 pm is for 1 s of measurement; long-term vacuum testing of nEUCLID would be required to confirm its long-term sensitivity, as discussed in Section 7.2.1.

distances of several metres. This would require proof of the concept over tens of metres, but currently there is no sign of nEUCLID not being able to perform such operations.

Chapter 7

CONCLUSION

7.1 Discussion of nEUCLID Characteristics

The performance values for nEUCLID are compared with EUCLID and COATS in Table 7.1, and will now be discussed in detail.

nEUCLID is slightly larger than both COATS and EUCLID. This is due to nEUCLID being built with standard off-shelf components; EUCLID was built with vacuum-safe components for aLIGO, and COATS was built with space-qualified components. This also increases the mass of nEUCLID compared to EUCLID and COATS. However, using standard components means that nEUCLID is cheaper to build.

nEUCLID has a much lower power than COATS, due to having only one laser. Looking at the longitudinal axis of COATS for a fairer comparison, the laser is 4.0 W which is still much higher than the DFB laser used in nEUCLID. Because nEUCLID and EUCLID contain only one laser the total power of the system is lower, and if the devices were space-qualified fewer redundancy components are necessary.

The tilt immunity of nEUCLID arising from the PCE has been proven, shown in Section 5.1.2, and the work has been published (see Appendix F). The range of tilt of the target mirror, $\pm 0.35°$, is less than that of EUCLID ($\pm 1°$). However, the working distance of nEUCLID (660 mm) is 11 times larger than that of EUCLID. The working distance of COATS is much larger than both of these values (100 m), but there is no reason future versions of nEUCLID could not achieve this distance. A working distance for the current nEUCLID of 1.0 km is achievable (neglecting tilt immunity of the target, as this would cause the optics to scale up in size).

A working range of ± 120 mm allows a wide range of displacement of the target in nEUCLID, which is extremely useful for future applications. This is 40 times larger than the working range of EUCLID (± 3 mm). COATS has a longitudinal working range of 100 m.

The single-pass interference pattern in nEUCLID is a problem, as it gives the impression the device is not tilt-immune; the single-pass beam is not tilt-immune as it does not pass through the PCE. EUCLID copes with the single-pass beam by not being a coaxial

	EUCLID	**nEUCLID**	**COATS**
Dimensions (mm)	$60 \times 22.5 \times 56$	$280 \times 160 \times 110$	$177.6 \times 110 \times 70$
Wavelength (nm)	667	1550	1542 (long.)
			850 (lat.)
			780 (ang.)
Total Laser Power (mW)	0.05	7.0	4.2×10^3
Mass (kg)	0.131	≈ 2.0	< 1.0
Working Distance (mm)	6	660	100×10^3
Working Range ($\pm$ mm)	3	120	100×10^3
Max. Tilt Immunity ($\pm^\circ$)	1.0	0.35	-
Angular Range ($\pm$")	-	-	350 (at 7.5 m)
Sensitivity (at 1 Hz)	50 pm (vac.)	420 pm (air)	1 µm (air)

Table 7.1: Table laying out the characteristics of the three similar devices. All properties are of the optical head only. [18] [31]

system, and by slightly misaligning the optical components. Unfortunately, the brief from Airbus DS meant that nEUCLID had to be coaxial, and despite misaligning the optical components the single-pass beam is still a problem. It is still not clear why the intensity of the single-pass beam is higher than predicted, given the supplier data for the optical components. Further analysis would need to be undertaken to confirm the intensity propagation each optical component in nEUCLID, as well as comparison with higher quality optical components.

Matching the Lissajous patterns seen from nEUCLID due to the position of the photodiode has been successful, confirming that the shape of the Lissajous pattern is dependent on the section of the interference pattern the photodiode is seeing. However, the displacement of the target beam required to produce Lissajous patterns that match the data is approximately an order of magnitude less than that calculated using the theory described in Eq. (3.18). With the removal of the focusing effect of the PCE, and thus the beam divergence, described in Section 5.5, the source of this discrepancy should hopefully be revealed.

The sensitivity of nEUCLID is acceptable, given that the data were taken in air. A result of $420\,\mathrm{pm}/\sqrt{\mathrm{Hz}}$ (at 1 Hz) is comparable to that of EUCLID; EUCLID achieves $50\,\mathrm{pm}/\sqrt{\mathrm{Hz}}$ at 1 Hz in vacuum, but has a target arm length that is 11 times smaller than that of nEUCLID. COATS achieves a much lower sensitivity of $1\,\mu\mathrm{m}/\sqrt{\mathrm{Hz}}$ at 1 Hz in air, most likely due to the increased armlength difference.

The noise of the electronics for nEUCLID, $4.78 \times 10^{-14}\,\mathrm{m}/\sqrt{\mathrm{Hz}}$, does not appear to impinge on the sensitivity of the device in air. The Johnson noise is $2.73 \times 10^{-14}\,\mathrm{m}$ per $\sqrt{\mathrm{Hz}}$, the shot noise is $\approx 5.2 \times 10^{-13}\,\mathrm{m}/\sqrt{\mathrm{Hz}}$, and the effective displacement noise for frequency noise is $2.28 \times 10^{-12}\,\mathrm{m}/\sqrt{\mathrm{Hz}}$. It would worth investigating how these noise values affect the sensitivity of nEUCLID when it is tested in a vacuum.

7.2 Future Work

The nEUCLID developed in this thesis is the first of its kind, thus a few small developments could be made to improve its basic functionality. The most relevant changes for future applications are discussed below.

7.2.1 Improving the Sensitivity

As discussed in Section 5.5, the focusing effect of the PCE limits the sensitivity of nEUCLID by causing the target beam to diverge and creating the phase effect in the Lissajous pattern described in Section 5.4. The sensitivity is also reduced by the single-pass beam, described in Section 5.3. This section discusses removal of the single-pass beam, and how nEUCLID could be tested in a vacuum chamber, to remove air turbulence noise.

Removing the Single-Pass Beam

Removing, or at least reducing the intensity of, the single-pass interference pattern would improve the sensitivity of nEUCLID. This can hopefully be achieved by buying higher-grade polarisation optical components, and by ensuring the target beam is not attenuated through the PCE via higher quality AR coatings on the lenses. Reducing the divergence of the target beam in nEUCLID will also help with this problem, as it will increase the intensity of the target beam on the photodiodes.

As discussed in Section 5.3, the power for each beam was determined using the CCD image of the interference patterns, and compared with the output power of each beam calculated from supplier data for the optical components. The difference between the measured single-pass and double-pass beam values is much higher those predicted by the supplier data: 30% compared to 0.45%. This was confirmed by the power reading taken at different points through the optical system.

The optical properties of the PBSs were also measured and compared with the manufacturer's data. The measured transmission value (when reflecting the beam) and reflectance value (when transmitting the beam) were both much higher than that specified by the manufacturer's data – 33% compared to 1%.

It is not yet understood why the manufacturers' data predicts such a low value in comparison to what is measured in nEUCLID.

Vacuum Testing

The current nEUCLID has not been tested in a vacuum; the sensitivity results were achieved in air in the optical laboratory. To be able to accurately compare the results with those of EUCLID, and also to see how much the unequal armlength affects the sensitivity, vacuum testing is necessary. This would require the optics to be re-mounted with vacuum-safe adhesive, as well as ensuring all the optical posts, mounts and cabling were vacuum-safe. It would also be worth measuring the sensitivity of an equal armlength

nEUCLID, both in air and in vacuum, to see how this changes in response to a much shorter arm.

7.2.2 An Absolute nEUCLID

nEUCLID measures the incremental displacement of the target, D, from an initial position to a final position: $D = l_f - l_i$. If the measurement beam is suddenly blocked, or the target tilted out of range, the displacement reading would be lost and any subsequent measurements would be from zero. To avoid this problem, the wavelength of the interferometer can be modulated using temperature or current, providing an absolute measurement of the distance, L.

The DFB laser in nEUCLID has a temperature-tuning coefficient of $0.1\,\mathrm{nm\,K^{-1}}$ and a current-tuning coefficient of $0.1\,\mathrm{nm\,mA^{-1}}$, with 1.0 nm tunability either side of the peak wavelength [38]. The laser has modulation current of 13 mA to 33 mA, allowing a change in wavelength of $17\,\mathrm{nm\,mA^{-1}}$ (33 mA - 13 mA * $0.1\,\mathrm{nm\,mA^{-1}}$).

The beam on the photodiodes has an optical phase from the difference in the interferometer arm lengths, l, as discussed in Section 2.2.4. When the temperature/current is modulated the wavelength changes from λ_1 to λ_2. This change in wavelength can be defined by one synthetic wavelength, Λ

$$\Lambda = \frac{\lambda_1 \lambda_2}{(\lambda_2 - \lambda_1)}, \tag{7.1}$$

The phase of the modulated system, shifting from the original position, ϕ_1, to the final position, ϕ_2, can be developed from Eq. (2.32) to become Φ

$$\Phi = \frac{8\pi L}{\Lambda}, \tag{7.2}$$

The synthetic wavelength for the maximum modulation range of $17\,\mathrm{nm\,mA^{-1}}$ of nEUCLID is approximately 1.4 mm.

There are problems with this modulation technique. If the wavelength is altered, the current changes, thus the intensity changes. This means the amplitude of the beam varies, causing the Lissajous pattern to vary in size. This would need to be accounted for in the processing (i.e. power stabilisation; see [22, pp. 78-79] for more details).

7.2.3 Equipment Alterations

The photodiode cables need stabilising; they can cause displacement of the mounts during transportation of the device. The optics are only of reasonable quality, thus are susceptible to poor-quality beam reflectance/transmittance, e.g. the PBSs. The AR coatings for each optical component are specific to the manufacturer, thus detailed information regarding their properties is unfortunately not readily available to the customer. However, an average value of reflectance is given for certain components (see Appendix C). From the experiments described in Section 7.2.1, the optical components supplied for nEUCLID were not as good

as those tested for the manufacturers' data. With the help of further investment it is hoped that this quality can be improved upon by using a different supplier.

The element mounting is not stable; the mini-series posts and post holders are liable to bend with large loads or medium force. If vacuum testing was performed the optics should be mounted directly to the breadboard, as in EUCLID, using the appropriate adhesive.

7.3 Summary of Thesis

This thesis has described the design and subsequent building of a new polarisation-based homodyne interferometer that works at large distances and is immune to tilt – the new Easy to Use Compact Laser Interferometric Device (nEUCLID). nEUCLID has evolved from a previous interferometer also produced at the University of Birmingham, EUCLID, and was carried out with funding from Airbus Defence and Space (DS) to look for potential space applications.

During the development of nEUCLID a new cat's eye system – the pseudo cat's eye (PCE) – was designed to enable the interferometer to work at large distances (i.e. at least several hundred mm). The PCE has a lower wavefront error than the conventional cat's eye (CCE) at large distances (beyond 60 mm), as well as being capable of working at these distances. In fact, the larger the working distance, the lower the wavefront error. The size of the PCE (the distance between the constituent lenses) is reduced as the working distance increases, making the system extremely useful for space applications. This work has been published in Applied Optics [33], and is given in Appendix F.

nEUCLID has a working distance of 660 mm, with a working range of ±120 mm. This is a vast improvement on the current working distances and ranges of polarisation-based homodyne interferometers, for example the EUCLID, which has a working distance of only 6 mm and a working range of ±3 mm.

The closest competitor of nEUCLID is the COATS device produced by INRiM. Whilst this has a working distance of 100 m and is capable of measuring lateral, longitudinal and angular displacement, COATS has a much higher power requirement (4.2 W compared with 7 mW). COATS measures angular displacement with one of its three lasers, and it has a lower sensitivity in air than nEUCLID, $1\,\mu m/\sqrt{Hz}$. nEUCLID has a tilt range of ±0.35°, and a sensitivity of $420\,pm/\sqrt{Hz}$ (at 1 Hz, in air). Further details are shown in Table 7.1.

Within this thesis potential space-industry applications for nEUCLID have been explored. Vibration monitoring, thermoelastic testing, and antenna metrology are promising areas where ground-based nEUCLIDs would be useful; remote sensing for light-weight structures is an active area of research in the space industry. Whilst in space, future formation flying missions, adaptive optics, and position sensors for antennas are areas that would benefit from the long working distance and sensitivity of nEUCLID.

Before any further development of nEUCLID for these applications a few enhancements can be made. Firstly, it would be advantageous to remove the focusing effect from the PCE, to improve the interference pattern visibility and remove the need to model the Lissajous patterns and control the photodiode positions. This can be achieved using two standard off-the-shelf lenses (Section 5.5), so would be a natural next step for this project.

Secondly, the single-pass interference pattern needs to be eliminated as this will disrupt the tilt immunity of the device. Finally, the sensitivity of nEUCLID in a vacuum needs to be measured, to confirm the noise of the electronics in a simulated space environment.

Although improvements must be made before nEUCLID can be used in real-world applications, it has successfully demonstrated the ability to remain tilt-immune at large distances whilst being of low mass and low power, fulfilling the brief laid out by Airbus DS.

Appendix A

List of Acronyms

ADC	analogue to digital converter
aLIGO	Advanced Laser Interferometer Gravitational-wave Observatory
APM	antenna pointing mechanism
AR	anti-reflection
ASD	amplitude spectral density
CCD	charge-coupled device
CCE	conventional cat's eye
CCRR	cube-corner retro-reflector
CLR	coherent laser radar
COATS	Compact Optical Attitude Transfer System
CORDIC	Coordinate Rotation Digital Computer
DC	direct current
DFB	distributed feedback
DS	Defence and Space
EO	Earth Observation
ESA	European Space Agency
EUCLID	Easy to Use Compact Laser Interferometric Device
FC/APC	fibre channel/angled physical contact
FPGA	Field Programmable Gate Array
GFZ	German Research Centre for Geosciences
GRACE	Gravity Recovery and Climate Experiment
HWP	half wave plate
ILIAD	Innovative Laser Interferometric Angular Device
INRiM	Istituto Nazionale di Ricerca Metrologica
IR	infra-red
JPL	Jet Propulsion Laboratory

JWST	James Webb Space Telescope
LPF	LISA Pathfinder
LRI	Laser Ranging Interferometer
NASA	National Aeronautics and Space Administration
nEUCLID	new Easy to Use Compact Laser Interferometric Device
NG	next generation
NPBS	non-polarising beamsplitter
PBS	polarising beamsplitter
PC	personal computer
PCE	pseudo cat's eye
PD	photodiode
PSD	power spectral density
PZT	lead zirconate titanate
QWP	quarter wave plate
RF	radio frequency
TPF	Terrestrial Planet Finder
TRL	technology readiness level
USB	Universal Serial Bus
VCSEL	vertical-cavity surface-emitting laser
WIVERN	Wind Velocity Radar Nephoscope

Appendix B

Data Acquisition Software Screenshots

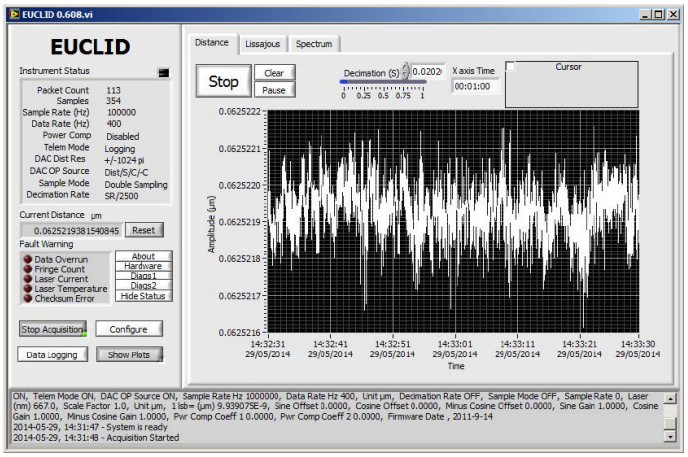

(a) A displacement plot from EUCLID.

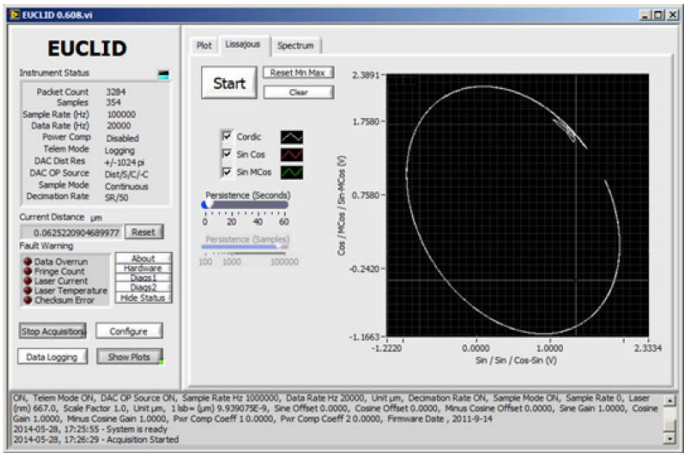

(b) A Lissajous pattern from EUCLID.

Figure B.1: Data output from the EUCLID software program [18]

Appendix C

List of nEUCLID Materials

This table presents the components used in nEUCLID, in the order in which they are used in the interferometer.

Component	**Part Name/ Number**	**Supplier**	**Material**	**Average Reflectance**
DFB Laser (1550 nm)	-	Laser 2000	-	-
Fibre	LAS-13-165	Laser 2000	-	-
Collimator	F810 APC 1550	Thorlabs	-	-
Polariser	06 WL 25	Comar Optics	-	-
Polarising Beamsplitter	PBS254	Thorlabs	N-SF1	<0.5%
Non-polarising Beamsplitter	BS015	Thorlabs	N-BK7	<0.5%
Half-Wave Plate	755 CM 25	Comar Optics	Mica	Unavailable
Quarter-Wave Plate	378 CM 25	Comar Optic	Mica	Unavailable
Mirror	PF10-03-G01	Thorlabs	Aluminium	-
Cat's Eye Concave Lens	LC1611-C	Thorlabs	N-BK7	<0.5%
Cat's Eye Convex Lens	LA1708-C	Thorlabs	N-BK7	<0.5%
Meniscus Lens	2000 JO 25	Comar Optics	B270	<1.3%
Photodiode	FGA21	Thorlabs	InGaAs	-

Table C.1: List of components in nEUCLID, and their part names and materials [82] [83].

Appendix D

EUCLID

This appendix reports on the work described by S. Aston [9].

D.1 Optical Configuration

A 667 nm VCSEL diode is used as the laser source for EUCLID. The horizontally-polarised beam leaves the VCSEL and passes through a collimating aspheric lens, L1. The beam is transmitted through PBS 1 and through a NPBS, where approximately half the beam intensity is lost. The beam travels through a HWP, orientated at 22.5°, which rotates the plane of polarisation by 45°. This allows the beam to be split by PBS 2, transmitting half to the measurement arm and reflecting the other half into the reference arm.

The transmitted beam passes through QWP 1, orientated at 45°, and out of EUCLID towards the measurement target, MT. The beam reflects off the target, passing back through QWP 1 which reorientates the beam polarisation to cause the beam to be reflected at PBS 2. The deflected beam travels into the cat's eye set-up, which consists of a doublet lens, a plano-concave lens and a mirror, MC. Reflecting off the cat's eye mirror, the beam passes back through the lenses, and is again reflected by PBS 2 to the target and back. Upon reaching PBS 2 again, the beam is transmitted, due to rotation of polarisation from QWP 1, recombining with the returning reference beam.

In the reference arm the beam passes through QWP 2, reflects off a mirror (MR), and passes back through the QWP. This orientates the polarisation to cause PBS 2 to transmit the beam through the cat's eye lens system. The beam reflects off MC and returns back through QWP 2, reflecting off MR again. A final pass through QWP 2 rotates the polarisation to reflect at PBS 2, recombining with the measurement beam.

Once recombined, the (now united) beam passes back through the HWP and is split by the NPBS. The transmitted half, which comprises two polarisation components, travels on through QWP 3 which shifts one of the polarisations by $\pi/2$. This beam is separated into the two polarisation components by PBS 3, each to a photodiode (PD1 and PD3). The reflected beam half is reflected again, by PBS1, to PD2.

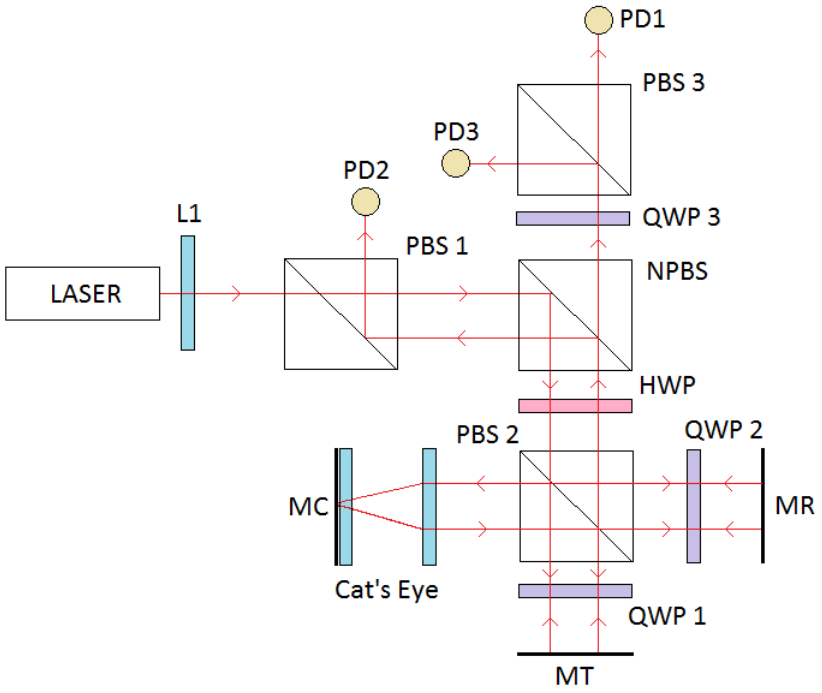

Figure D.1: Schematic of the EUCLID configuration.

D.2 Electronics

The electronics module for EUCLID (Fig. D.2) was built by electronics engineer, David Hoyland. It is a "plug-and-play" device containing a high-speed data acquisition system, the laser diode and accompanying laser diode electronics. The module contains an FPGA; a small chip of an array of logic gates capable of performing complex calculations.

Using a Coordinate Rotation Digital Computer (CORDIC) algorithm, a method that uses simple mathematical operations to find the sine/cosine of an angle, the FPGA calculates the arctangent from the three photodiode signals using Eq. (2.39). The use of an FPGA allows the phase calculation to be completed inside the electronics unit, reducing overall data transmission time. A transimpedence amplifier converts current detected by the photodiodes into voltage the FPGA can use, via an ADC. Each of the three ADC channels are 18-bit and can acquire data at a maximum sample rate of 1 MHz [9]. The maximum target tracking speed is $41.4\,\mathrm{mm\,s^{-1}}$. These three channels can be used for monitoring the signal from the interferometer via an oscilloscope.

D.3 Software

Upon start-up the electronics box sends data to the personal computer (PC) via a Universal Serial Bus (USB) connection. A LabVIEW program was written to control and calibrate EUCLID by software engineer, John Bryant. This program configures the electronics module by sending commands to the FPGA to allow the interferometer to be calibrated before use. Once the displacement measurement has begun, the arctangent calculation

Figure D.2: Photograph of the EUCLID electronics module

results are sent to the PC via USB connection where the measured displacement is plotted as a function of time. The program can also log the displacement data in a data file, and display the resulting Lissajous patterns, as shown in Appendix B.

This program also allows control of the sample rate and decimation rate; the speed at which EUCLID converts the raw PD signals into displacement, and the size the data is cut into to send to the PC. The sample rate for EUCLID can range from 250 kHz to 1 MHz. The decimation rate can be either by 50 or 2500 times [18]. The data acquisition rate is the sample rate divided by the decimation rate.

For more details on the software see the EUCLID User Guide [18].

D.4 Operational Characteristics

As described in the EUCLID User Guide, the working distance s is 6 mm and the working range w_r is ± 3 mm [18]; please refer to this manual for further details.

The sensitivity of EUCLID is $50\,\mathrm{pm}/\sqrt{\mathrm{Hz}}$ at 1 Hz in a vacuum, as shown in Fig. D.3. The sampling rates of both 250 kHz and 1 MHz are shown, as are the relevant noise budgets. At low frequencies 1/f noise from the VCSEL is present, as well as from the operational amplifier; at high frequencies (above 1 kHz) EUCLID becomes limited by shot noise. For further detail on the noise sources in EUCLID please refer to [9].

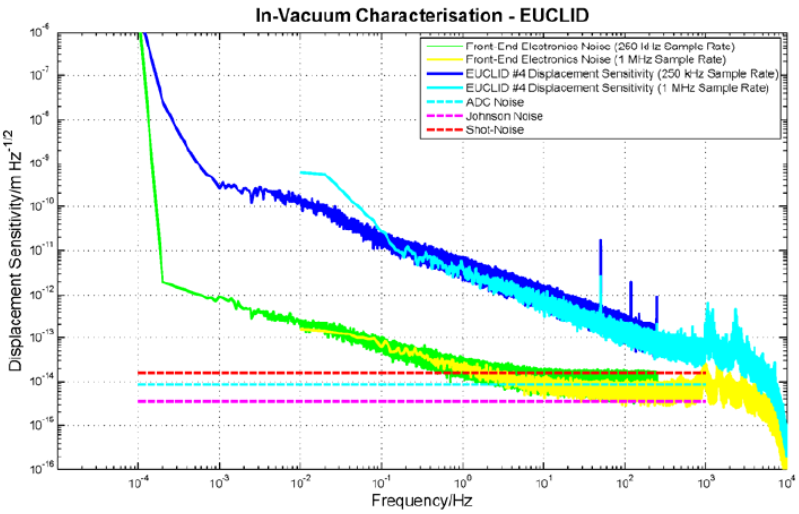

Figure D.3: The sensitivity plot for EUCLID in a vacuum [9] including relevant noise sources.

Appendix E

Code to Correct for Target Beam Divergence

The MatLab code presented here uses Gaussian optics to model the solution to the substantial difference between target and reference beam widths and radii of curvature, as discussed in Section 3.4. To allow the best visibility possible a meniscus lens of focal length -2013 mm was chosen for the reference arm to match the target beam parameters. The data this code produces is shown in Section 3.4 and Section 5.1.1.

```
% Delta correcting code for thesis (updated 10/11/15)

clear

% Define variable values
lambda = 1550e-6;
w0 = 2.487; % Calculated beam waist input from the collimator
R0 = Inf; % Radius of curvature of input collimated beam
del = 0:pi/2:pi; % Vary 'tap' amount to mimic phase change
delta = -0.004187; % Cat's eye delta value
a = 710; % Length of target arm (target mirror to CE lens 1)
efl = -2013; % Focal length of ref. arm correcting lens (Comar)

% Relationships
k = 2*pi/lambda;

% Reference arm distances in lab set-up
r1 = 171; % Coll. to RM
r2 = 152.8; % Distance from RM to focusing lens

% Target arm distances in lab set-up
t1 = 184.9; % Coll. to targ. arm start
t2 = 170.2; % Targ. arm end to focusing lens

%%% FOCUSING OUTPUT LENS %%%
df = 84 + 7; % (Sensor depth + lens depth)
Lf = 79.8;
DF = [1,df;0,1];
LF = [1,0;-1/Lf,1];

%%% TARGET ARM %%%
T1 = [1,t1;0,1];
T2 = [1,t2;0,1];
```

```
arm = [1,a;0,1];
ce = [-1,0;delta,-1];
d1 = T2*arm*ce*arm*T1;
Lt = t2+a+a+t1;

% Define target arm matrix parameters
At = A_ABCD(d1);
Bt = B_ABCD(d1);
Ct = C_ABCD(d1);
Dt = D_ABCD(d1);

%%% REFERENCE ARM %%%
R1 = [1,r1;0,1];
R2 = [1,r2;0,1];

% Lens to match output beam waist and rad. curv. to that of target arm
L = [1,0;-1/efl,1];
d2 = R2*L*L*R1; % Double lens pass
Lr = r2+r1;

% Define ref arm matrix parameters
Ar = A_ABCD(d2);
Br = B_ABCD(d2);
Cr = C_ABCD(d2);
Dr = D_ABCD(d2);


%%% CALC. INTENSITY %%%

% New expressions, one for each arm
% Function: alpha = (2/(k*w0^2)) + (1i/R0);
alpha = alpha(w0,R0,lambda);
% Function: p_amp = A + 1i*alpha*B;
pr = p_amp(alpha,Ar,Br);
pt = p_amp(alpha,At,Bt);
% Function: beta = (alpha*D - 1i*C) / (A + 1i*alpha*B);
beta_r = beta(alpha,Ar,Br,Cr,Dr);
beta_t = beta(alpha,At,Bt,Ct,Dt);

% Check radius of curvature for each beam - should be the same
R_t = 1/imag(beta_t);
R_r = 1/imag(beta_r);
% Check beam width for each beam - should be the same
w_r = sqrt(2/real(k*beta_r));
w_t = sqrt(2/real(k*beta_t));

% Calculate and plot intensity over range of r
r = -1:0.01:1;

% Want fringe pattern for the peak visibility
ref = 0.25; t = 1;
int_del0 = comb_intensity_calib(w0,pr,pt,Lr,Lt,beta_r,beta_t,r,lambda,del(1),ref,t);
int_delpi2 = comb_intensity_calib(w0,pr,pt,Lr,Lt,beta_r,beta_t,r,lambda,del(2),ref,t);
int_delpi = comb_intensity_calib(w0,pr,pt,Lr,Lt,beta_r,beta_t,r,lambda,del(3),ref,t);
% where Function: comb_intensity_calib = abs(ut+ur).^2;
% Target arm amplitude, ut = tc * exp(1i*del).' * (1/sqrt(0.5*pi*(w0^2))) * (1/pt)
% ... * exp(1i*k*Lt) * exp(-0.5*beta_t*k*(r.^2));
% Reference arm amplitude, ur = rc * ones(size(del)).' * (1/sqrt(0.5*pi*(w0^2))) * (1/pr)
% ... * exp(1i*k*Lr) * exp(-0.5*beta_r*k*(r.^2));

% Plot interference pattern
```

```
figure(2)
plot(r,int_del0,r,int_delpi)
legend('k*delta z = 0','k*delta z = pi'); grid on
title('Theoretical output beam interference pattern','FontWeight','bold','FontSize',12)
xlabel('Beam width (mm)','FontWeight','bold','FontSize',11)
ylabel('Intensity','FontWeight','bold','FontSize',11)


% CALCULATE FRINGE VISIBILITY (%)
% Integrate area which PD would see (1 mm diameter, as in lab)
t_max = 2*pi*trapz(int_del0(50:151));
t_min = 2*pi*trapz(int_delpi(50:151));

% Calculate visibility from these values (percent)
vis_new = (t_max - t_min)/(t_max + t_min) * 100;
```

Appendix F

"Pseudo-cat's eye for improved tilt-immune interferometry" - Speake and Bradshaw

applied optics

Pseudo-cat's eye for improved tilt-immune interferometry

CLIVE C. SPEAKE[1,*] AND MIRANDA J. BRADSHAW[1,2]

[1]School of Physics and Astronomy, University of Birmingham, West Midlands B15 2TT, UK
[2]e-mail: mjb@star.sr.bham.ac.uk
*Corresponding author: c.c.speake@bham.ac.uk

Received 25 March 2015; revised 24 July 2015; accepted 28 July 2015; posted 29 July 2015 (Doc. ID 236884); published 18 August 2015

We present a new simple optical design for a cat's eye retroreflector. We describe the design of the new optical configuration and its use in tilt-immune interferometry where it enables the tracking of the displacement of a plane target mirror with minimum sensitivity to its tilt about axes orthogonal to the interferometer's optical axis. In this application the new cat's eye does not behave as a perfect retroreflector and we refer to it as a "pseudo"-cat's eye (PCE). The device allows, for the first time, tilt-immune interferometric displacement measurements in cases where the nominal distance to the target mirror is significantly larger than the length of the cat's eye. We describe the general optical characteristics of the PCE and compare its performance in our application with that of a conventional cat's eye optical configuration using ABCD matrices and Zemax analyses. We further suggest a simple modification to the design that would enable the PCE to behave as a perfect cat's eye, and this design may provide an advantageous solution for other applications.

OCIS codes: (220.3620) Lens system design; (120.4820) Optical systems; (120.3180) Interferometry.

http://dx.doi.org/10.1364/AO.54.007387

1559-128X/15/247387-09$15/0$15.00

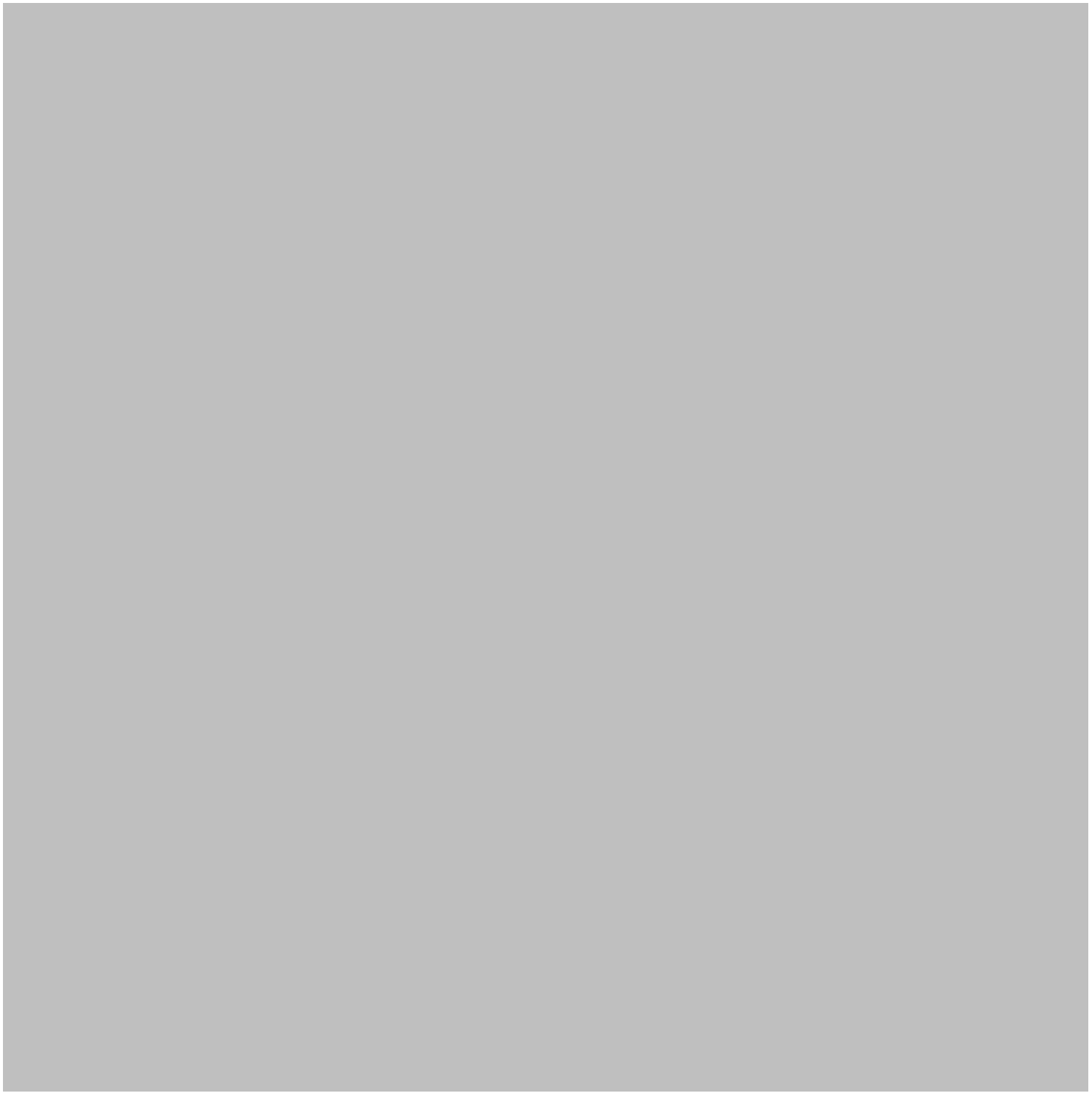

Bibliography

[1] Marshall Space Flight Centre. Advanced Space Transportation Program: Paving the Highway to Space, 2008.

[2] G T. Boothe G Mueller A Preston, B Balaban. Stable materials and bonding techniques for space-based optical systems. *NASA Science Technology Conference*, 2007.

[3] Space Telescope Science Institute. James Webb Space Telescope Wavefront Sensing and Control. `http://www.stsci.edu/jwst/ote/wavefront-sensing-and-control`, . Last accessed: 2015-08-05.

[4] Airbus DS GmbH. Airbus Defence and Space: About Us. `http://airbusdefenceandspace.com/about-us/`, 2015. Last accessed: 2015-08-15.

[5] A. A. Michelson and E. W. Morley. On the relative motion of the earth and the luminiferous ether. *The American Journal of Science - Third Series*, XXXIV(203): 333–345, November 1887.

[6] B P Abbott et al. Ligo: the laser interferometer gravitational-wave observatory. *Reports on Progress in Physics*, 72(7):076901, 2009. URL `http://stacks.iop.org/0034-4885/72/i=7/a=076901`.

[7] A F Fercher. Optical coherence tomography. *Journal of Biomedical Optics*, 1(2):157 – 173, April 1996.

[8] *Measurement of aspheric mirror segments using Fizeau interferometry with CGH correction*, volume 7739, 2010. SPIE Optical Engineering Press.

[9] S. M. Aston. *Optical Read-Out Techniques for the Control of Test Masses in Gravitational Wave Observatories*. PhD thesis, School of Physics and Astronomy, University of Birmingham, UK, January 2011.

[10] Fabián E. Peña-Arellano and Clive C. Speake. Mirror tilt immunity interferometry with a cat's eye retroreflector. *Appl. Opt.*, 50(7):981–991, March 2011. doi: 10.1364/AO.50.000981. URL `http://ao.osa.org/abstract.cfm?URI=ao-50-7-981`.

[11] E. Hecht. *Optics*. Addison Wesley, third edition, 1998.

[12] Hassan Habib. Calibration of Coordinate Measuring Machines (CMM). `http://www.slideshare.net/hassang66/calibration-of-coordinate-measuring-machines-cmm`, April 2015. Last accessed: 2015-09-21.

[13] Kjell J Gåsvik. *Optical Metrology*. John Wiley & Sons Ltd., third edition, 2002.

[14] Michael Bass, editor. *Handbook of Optics: Devices, Measurements and Poroperties*, volume 2. McGraw-Hill Inc., 1995.

[15] M. J. Downs and K. W. Raine. An unmodulated bi-directional fringe-counting interferometer system for measuring displacement. *Precision Engineering*, pages 85–89, November 1978.

[16] Vincenzo Greco, Giuseppe Molesini, and Franco Quercioli. Accurate polarization interferometer. *Review of Scientific Instruments*, 66(7):3729–3734, 1995. doi: http://dx.doi.org/10.1063/1.1145429. URL `http://scitation.aip.org/content/aip/journal/rsi/66/7/10.1063/1.1145429`.

[17] Stuart M. Aston and Clive C. Speake. An interferometric based optical read-out scheme for the lisa proof-mass. *AIP Conference Proceedings*, 873(1):326–333, 2006. doi: http://dx.doi.org/10.1063/1.2405063. URL `http://scitation.aip.org/content/aip/proceeding/aipcp/10.1063/1.2405063`.

[18] C. Speake, D. Hoyland, and J. Bryant. *EUCLID Compact Interferometer User Guide: Version 2.9*. University of Birmingham, Birmingham, UK, May 2014.

[19] S. M. Aston. External and internal photos of EUCLID. Private collection, 2011.

[20] Fabián E. Peña-Arellano. *Characterization of polarization homodyne interferometers*. PhD thesis, School of Physics and Astronomy, University of Birmingham, UK, May 2008.

[21] Terry Quinn, Harold Parks, Clive Speake, and Richard Davis. Improved determination of g using two methods. *Phys. Rev. Lett.*, 111:101102, Sep 2013. doi: 10.1103/PhysRevLett.111.101102. URL `http://link.aps.org/doi/10.1103/PhysRevLett.111.101102`.

[22] Hasnain Panjwani. *Development of a Torsion Balance Facility and a search for Temporal Variations in the Newtonian Gravitational Contstant*. PhD thesis, School of Physics and Astronomy, University of Birmingham, UK, July 2012.

[23] Fabián Erasmo Peña Arellano, Hasnain Panjwani, Ludovico Carbone, and Clive C. Speake. Interferometric measurement of angular motion. *Review of Scientific Instruments*, 84(4):043101, 2013. doi: http://dx.doi.org/10.1063/1.4795549. URL `http://scitation.aip.org/content/aip/journal/rsi/84/4/10.1063/1.4795549`.

[24] David Hoyland. Euclid electronics - front end noise. Technical report, University of Birmingham, 2011.

[25] Garry Berkovic and Ehud Shafir. Optical methods for distance and displacement measurements. *Adv. Opt. Photon.*, 4(4):441–471, Dec 2012. doi: 10.1364/AOP.4.000441. URL `http://aop.osa.org/abstract.cfm?URI=aop-4-4-441`.

[26] M. Lescure R. Myllylä M.C. Amann, T. Bosch and M. Rioux. Laser ranging: a critical review of usual techniques for distance measurement. *Optical Engineering*, 40(1):10 – 19, 2001.

[27] Philip A. Hiskett, Colin S. Parry, Aongus McCarthy, and Gerald S. Buller. A photon-counting time-of-flight rangingtechnique developed for the avoidance of rangeambiguity at gigahertz clock rates. *Opt. Express*, 16(18):13685–13698, Sep 2008. doi: 10.1364/OE.16.013685. URL http://www.opticsexpress.org/abstract.cfm?URI=oe-16-18-13685.

[28] Hai-Jun Yang, Jason Deibel, Sven Nyberg, and Keith Riles. High-precision absolute distance and vibration measurement with frequency scanned interferometry. *Appl. Opt.*, 44(19):3937–3944, Jul 2005. doi: 10.1364/AO.44.003937. URL http://ao.osa.org/abstract.cfm?URI=ao-44-19-3937.

[29] M Kalin A Pogačnik, T Požar and J Možina. A homodyne quadrature laser interferometer for micro-asperity deformation analysis. *Sensors*, 13(1):703, 2013. ISSN 1424-8220. doi: 10.3390/s130100703. URL http://www.mdpi.com/1424-8220/13/1/703.

[30] T. Požar, T.ar, P. Gregorčič, and J. Možina. A precise and wide-dynamic-range displacement-measuring homodyne quadrature laser interferometer. *Applied Physics B*, 105(3):575–582, 2011. ISSN 0946-2171. doi: 10.1007/s00340-011-4512-5. URL http://dx.doi.org/10.1007/s00340-011-4512-5.

[31] M. Pisani. Coats executive summary report. Technical report, Istituto Nazionale di Ricerca Metrologica (INRIM), July 2014.

[32] J. J. Snyder. Paraxial ray analysis of a cat's eye retroreflector. *Applied Optics*, 14(8): 1825 – 1828, 1975.

[33] Clive C. Speake and Miranda J. Bradshaw. Pseudo-cat's eye for improved tilt-immune interferometry. *Appl. Opt.*, 54(24):7387–7395, Aug 2015. doi: 10.1364/AO.54.007387. URL http://ao.osa.org/abstract.cfm?URI=ao-54-24-7387.

[34] A. E. Siegman. *Lasers*. University Science Books, California, 1986.

[35] IBM Redbooks. Understanding Optical Communications: 5.4.6 Circulators. http://imedea.uib-csic.es/~salvador/coms_optiques/addicional/ibm/ch05/05-16.html, November 1998. Last accessed: 2015-09-21.

[36] D.J. Littler, editor. *Electrical Systems and Equipment: Incorporating Modern Power System Practice*, volume D. Pergamon Press, 1992.

[37] Y. Deshayes, L. Bechou, F. Verdier, B. Tregon, D. Laffitte, Jl. Goudard, Y. Hernandez, and Y. Danto. Estimation of lifetime distributions on 1550 nm dfb laser diodes using monte-carlo statistic computations. pages pp. 103–115. SPIE, 2004. URL https://hal.archives-ouvertes.fr/hal-00162359.

[38] Personal communication with Lisa at Laser 2000, June 2013.

[39] *Z8 Series Motorized DC Servo Actuators User Guide*. Thorlabs, revision 13 edition, October 2013.

[40] Personal communication with D. Hoyland, October 2014.

[41] IEEE. Rf, rfic & microwave theory. http://www.ieee.li/pdf/essay/phase_noise_basics.pdf. Last accessed: 2015-09-13.

[42] T. Harrison J. Simpson, K. Boldt and J. Broch. Vibration testing of satellites. *Milsat Magazine*, March 2011. URL http://www.milsatmagazine.com/story.php?number=1453342281. Accessed: 2015-07-14.

[43] Personal communication with Dr C Trenkel at Airbus Defence and Space UK, September 2015.

[44] TJ Patrick AM Cruise, JA Bowles and CV Goodall. *Principles of Space Instrument Design*, volume Cambridge Aerospace Series 9. Cambridge University Press, 1998.

[45] P. R. K. Chetty. *Satellite Technology and Its Applications*. TAB Books, 1988.

[46] J. Ruze. The effect of aperture errors on the antenna radiation pattern. *Il Nuovo Cimento*, 9(3):364–380, 1952. ISSN 0029-6341. doi: 10.1007/BF02903409. URL http://dx.doi.org/10.1007/BF02903409.

[47] C Liu J M. Usoff, M T. Clarke and M J. Silver. Optimizing the husir antenna surface. *Lincoln Laboratory Journal*, 21(1):83 – 105, 2014.

[48] Hexagon Metrology. Leica absolute interferometer: A new approach to laser tracker absolute distance meters. Hexagon Metrology, 2012.

[49] Guofeng Zhou, Xiaoxing Li, Dongsheng Li, Jingdong Luan, and Jinze Zhao. Surface accuracy of a large-scale compact antenna test range considering mechanism, metrology and alignment. *Measurement Science and Technology*, 25(7):075011, 2014. URL http://stacks.iop.org/0957-0233/25/i=7/a=075011.

[50] Hexagon Metrology. Pcmm system specifications: Leica absolute tracker at901 and leica t-products. 2012.

[51] D J. Rochblatt and B L. Seidel. Microwave antenna holography. *IEEE Transactions on Microwave Theory and Techniques*, 40(6):1294 – 1300, June 1992.

[52] H. U. Frey. Thermoelastic measurements on reflectors for telecommunication satellites. *SAE Technical Paper*, 108(1), 1999. URL http://papers.sae.org/1999-01-2132/.

[53] GOM mbH. Aerospace: Development of a dimensionally stable lightweight structure for the lisa pathfinder science module. Technical report, GOM, 2008.

[54] Northrop Grumman. James Webb Space Telescope Artist Conception. https://www.flickr.com/photos/nasawebbtelescope/16658886757, 2015. Last accessed: 2015-08-05.

[55] Robert Puers. Capacitive sensors: When and how to use them. *Sensors and Actuators A: Physical*, 37–38:93 – 105, 1993. ISSN 0924-4247. doi: http://dx.doi.org/10.1016/0924-4247(93)80019-D. URL http://www.sciencedirect.com/science/article/pii/092442479380019D. Proceedings of Eurosensors {VI}.

[56] C C Speake and S M Aston. An interferometric sensor for satellite drag-free control. *Classical and Quantum Gravity*, 22(10):S269, 2005. URL http://stacks.iop.org/0264-9381/22/i=10/a=019.

[57] EADS Astrium, University of Reading, and Starlab. Wivern: Wind velocity radar nephoscope. Private, 2012.

[58] Anthony Illingworth. WIVERN: A WInd VElocity Radar Nephoscope or a figment of the imagination?, June 2014.

[59] James R. Wertz. *Spacecraft Attitude Determination and Control*. D Reidel Publishing Company, 1978.

[60] D. Petrolati C. Buck, C. Donlon and S. D'Addio. A roadmap for wavemill. In *Proceedings of the 3rd Workshop on Advanced RF Sensors and Remote Sensing Instruments (ARSI)*, 2011. URL http://www.congrex.nl/11c11/ARSI%20papers/BUCK_A%20Roadmap%20for%20Wavemill.pdf. Last accessed: 2014-10-04.

[61] Herbert J. Kramer. Wavemill 2d Ocean Current Mapping System. https://directory.eoportal.org/web/eoportal/airborne-sensors/wavemill, 2011. Last accessed: 2015-09-16.

[62] Personal communication with Katherine Bennell, Airbus Defence and Space, January 2013.

[63] ESA. Darwin Overview. http://www.esa.int/Our_Activities/Space_Science/Darwin_overview, October 2009. Last accessed: 2015-08-14.

[64] ESA. Darwin's six telescopes. http://www.esa.int/spaceinimages/Images/2015/06/Darwin_s_six_telescopes, April 2003. Last accessed: 2015-09-10.

[65] NASA. TPF Interferometer. http://science.nasa.gov/missions/tpf/, April 2015. Last accessed: 2015-08-14.

[66] Neptec UK. http://www.neptecuk.com/news/neptec-uk-announces-proba-3-space-contract/, July 2015. Last accessed: 2015-08-14.

[67] Helmholtz Centre Potsdam GFZ German Research Centre for Geosciences. GRACE Follow-On Mission: GFZ signs agreement with NASA. http://www.gfz-potsdam.de/en/media-communication/press-releases/details/article/grace-follow-on-mission-gfz-unterzeichnet-vertrag-mit-nasa-kopie-1/, February 2013. Last accessed: 2015-08-14.

[68] B.S. Sheard, G. Heinzel, K. Danzmann, D.A. Shaddock, W.M. Klipstein, and W.M. Folkner. Intersatellite laser ranging instrument for the grace follow-on mission. *Journal of Geodesy*, 86(12):1083–1095, 2012. ISSN 0949-7714. doi: 10.1007/s00190-012-0566-3. URL http://dx.doi.org/10.1007/s00190-012-0566-3.

[69] A. Baatzsch M. Dehne C. Diekmann K. Voss F. Gilles B. Guenther B. Zender S. Boehme V. Mueller D. Schuetze G.Stede B. Sheard G. Heinzel K. Nicklaus, M. Herding. Optical bench of the laser ranging interferometer on grace follow-on. In *International Conference on Space Optics 2014*, October 2014.

[70] NASA's Jet Propulsion Laboratory. Gravity Recovery and Climate Experiment Follow-On. http://www.jpl.nasa.gov/missions/gravity-recovery-and-climate-experiment-follow-on-grace-fo/. Last accessed: 2015-08-14.

[71] ESA P. Carril. Proba-3's Pair of Satellites. http://www.esa.int/spaceinimages/Images/2010/11/Proba-3_s_pair_of_satellites, 2013. Last accessed: 2015-08-14.

[72] MetOp Second Generation. http://www.esa.int/spaceinimages/Images/2012/11/MetOp_Second_Generation, November 2012. Last accessed: 2015-09-11.

[73] First Level-1b image from MHS, November 2006. Last accessed: 2015-09-11.

[74] Michel Bousquet and Gérard Maral. Satellite antenna depointing originating from attitude control and station keeping specifications. *International Journal of Satellite Communications*, 9(2):85–92, 1991. ISSN 1099-1247. doi: 10.1002/sat.4600090204. URL http://dx.doi.org/10.1002/sat.4600090204.

[75] J Stark P Fortescue and G Swinerd. *Spacecraft Systems Engineering*. John Wiley & Sons Ltd., third edition edition, 2003.

[76] W. Göschel et al. Three-axis stabilization of communication satellites. In C. W. Munday, editor, *Automatic Control in Space : Proceedings of the 8th IFAC Symposium*, page 451. Pergamon Press, 1979.

[77] Bruno Pattan. *Satellite Systems: Principles and Technologies*. Chapman & Hall, 1993. URL https://books.google.co.uk/books?id=0GJWEro9ea4C&pg=PA205&lpg=PA205&dq=spacecraft+antenna+pointing+accuracy&source=bl&ots=ZjeCy6gsey&sig=A5i1A1rZJwBiabTKXfoDHSMAE08&hl=en&sa=X&ved=0CDgQ6AEwAmoVChMIj82U7ZrpxgIVyQfbCh1Pegvr#v=onepage&q=%22IR%20sensor%22&f=false. Last accessed: 25-07-2015.

[78] Airbus Defence and Space. Image of Eutelsat 3B. http://www.space-airbusds.com/en/programme/eutelsat-3b-n8p.html, February 2015. Accessed: 2015-06-03.

[79] Vishal S. Chauhan & Rahul Vaish C.K. Susheel, Rajeev Kumar. Shape control of spacecraft antenna reflector using lead-free piezoelectric actuators. *European Journal of Computational Mechanics*, 23(5-6):199–216, 2014.

[80] Space Telescope Science Institute. The Primary Mirror: An Overview. http://jwst.nasa.gov/mirrors.html, . Last accessed: 2015-09-16.

[81] Herbert J. Kramer. PROBA-3 (Project for On-Board Autonomy-3). https://directory.eoportal.org/web/eoportal/satellite-missions/p/proba-3, 2013. Last accessed: 2015-09-16.

[82] Thorlabs Inc. Optical Coatings. http://www.thorlabs.de/newgrouppage9.cfm?objectgroup_id=5840, 2015. Last accessed: 2015-09-22.

[83] Comar Optics Ltd. Optical Coatings. http://www.comaroptics.com/technical/optical-coatings, 2015. Last accessed: 2015-09-22.